Measurement of the Cross Section for Diphoton Production in 1.8 TeV Proton-Antiproton Collisions

Draft Version 3.5

Takeshi TAKANO

A dissertation submitted to the Doctoral Program
in Physics, the University of Tsukuba
in partial fulfillment of the requirements for the
degree of Doctor of Philosophy (Science)
September 1997

Abstract

We have studied prompt diphoton production in proton-antiproton collisions at a center-of-mass energy of 1.8 TeV by the Collider Detector at Fermilab (CDF) .

Diphoton production in hadron-hadron collisions is one of the clear probe for testing the Next-to-Leading Order (NLO) calculation of the Quantum Chromodynamics (QCD) because of the advantage of the detection of photons with small systematic uncertainty and good energy resolution. The measurement of the diphoton production cross section can be used to check the QCD calculation. By looking at the transverse momentum of the diphoton system, diphoton production is also a good probe for measuring the effects of multiple initial soft gluon radiations and the intrinsic transverse momentum of the initial state partons, which are beyond the NLO prediction.

The data were collected by the CDF detector placed at BØ area of the Fermilab Tevatron collider during 1992 - 1995 collider run. The total integrated luminosity was about $110\,\mathrm{pb}^{-1}$. The trigger system, including both the hardware and the software modules, required the collision events to have two large and isolated electromagnetic energy depositions in the Central Electromagnetic Calorimeter (CEM) .

At offline level, we selected EM clusters which had no tracks associated with them. Using the Central Electromagnetic Strip chamber (CES), which were embedded in the CEM near the shower maximum, we required that the EM shower profile should be consistent with that obtained from testbeam electrons. Candidate photons with large additional CES clusters were rejected. At $p_T \geq 12\,\mathrm{GeV/c}$, we obtained 652 events as the diphoton candidate events. The efficiencies of each selection criterion for the photons were calculated with various CDF physics datasets.

The backgrounds against prompt photons come from neutral mesons (π^0's, η's, and K_s^0's) decaying into multiple photons. We cannot separate them on event-by-event basis, so we subtracted the backgrounds statistically by using the information from the CES

shower profile and the conversion rate in the Central Preradiator detector (CPR) placed in front of the CEM.

The photon fraction in the diphoton candidates was evaluated as a function of the transverse momentum (p_T) of the photons. It showed a large photon purity at high p_T region (0.6 at $p_T = 25\,\mathrm{GeV/c}$).

The differential cross section for diphoton production was measured as a function of the photon p_T, the invariant mass (M) of the diphotons, the azimuthal angle between diphotons ($\Delta\phi$), the ratio of the transverse momenta of the two photons (Z) and the p_T of the diphoton system. The results were compared with the NLO QCD prediction with CTEQ2M parton distribution functions. The results, as a function of the photon p_T, M and $\Delta\phi$, were consistent with the NLO prediction, while the results on the Z and the diphoton system p_T showed slight differences between data and theory.

Contents

The CDF Collaboration

F. Abe,[16] H. Akimoto,[35] A. Akopian,[30] M. G. Albrow,[7] S. R. Amendolia,[26] D. Amidei,[19] J. Antos,[32] S. Aota,[35] G. Apollinari,[30] T. Asakawa,[35] W. Ashmanskas,[17] M. Atac,[7] F. Azfar,[25] P. Azzi-Bacchetta,[24] N. Bacchetta,[24] W. Badgett,[19] S. Bagdasarov,[30] M. W. Bailey,[21] J. Bao,[38] P. de Barbaro,[29] A. Barbaro-Galtieri,[17] V. E. Barnes,[28] B. A. Barnett,[15] M. Barone,[26] E. Barzi,[9] G. Bauer,[18] T. Baumann,[11] F. Bedeschi,[26] S. Behrends,[3] S. Belforte,[26] G. Bellettini,[26] J. Bellinger,[37] D. Benjamin,[34] J. Benlloch,[18] J. Bensinger,[3] D. Benton,[25] A. Beretvas,[7] J. P. Berge,[7] J. Berryhill,[5] S. Bertolucci,[9] B. Bevensee,[25] A. Bhatti,[30] K. Biery,[7] M. Binkley,[7] D. Bisello,[24] R. E. Blair,[1] C. Blocker,[3] A. Bodek,[29] W. Bokhari,[18] V. Bolognesi,[2] G. Bolla,[24] D. Bortoletto,[28] J. Boudreau,[27] L. Breccia,[2] C. Bromberg,[20] N. Bruner,[21] E. Buckley-Geer,[7] H. S. Budd,[29] K. Burkett,[19] G. Busetto,[24] A. Byon-Wagner,[7] K. L. Byrum,[1] J. Cammerata,[15] C. Campagnari,[7] M. Campbell,[19] A. Caner,[26] W. Carithers,[17] D. Carlsmith,[37] A. Castro,[24] D. Cauz,[26] Y. Cen,[29] F. Cervelli,[26] P. S. Chang,[32] P. T. Chang,[32] H. Y. Chao,[32] J. Chapman,[19] M. -T. Cheng,[32] G. Chiarelli,[26] T. Chikamatsu,[35] C. N. Chiou,[32] L. Christofek,[13] S. Cihangir,[7] A. G. Clark,[10] M. Cobal,[26] E. Cocca,[26] M. Contreras,[5] J. Conway,[31] J. Cooper,[7] M. Cordelli,[9] C. Couyoumtzelis,[10] D. Crane,[1] D. Cronin-Hennessy,[6] R. Culbertson,[5] T. Daniels,[18] F. DeJongh,[7] S. Delchamps,[7] S. Dell'Agnello,[26] M. Dell'Orso,[26] R. Demina,[7] L. Demortier,[30] M. Deninno,[2] P. F. Derwent,[7] T. Devlin,[31] J. R. Dittmann,[6] S. Donati,[26] J. Done,[33] T. Dorigo,[24] A. Dunn,[19] N. Eddy,[19] K. Einsweiler,[17] J. E. Elias,[7] R. Ely,[17] E. Engels, Jr.,[27] D. Errede,[13] S. Errede,[13] Q. Fan,[29] G. Feild,[38] C. Ferretti,[26] I. Fiori,[2] B. Flaugher,[7] G. W. Foster,[7] M. Franklin,[11] M. Frautschi,[34] J. Freeman,[7] J. Friedman,[18] H. Frisch,[5] Y. Fukui,[16] S. Funaki,[35] S. Galeotti,[26] M. Gallinaro,[24] O. Ganel,[34] M. Garcia-Sciveres,[17] A. F. Garfinkel,[28] C. Gay,[11] S. Geer,[7] D. W. Gerdes,[15] P. Giannetti,[26] N. Giokaris,[30] P. Giromini,[9] G. Giusti,[26] L. Gladney,[25] D. Glenzinski,[15] M. Gold,[21] J. Gonzalez,[25] A. Gordon,[11] A. T. Goshaw,[6] Y. Gotra,[26] K. Goulianos,[30] H. Grassmann,[26] L. Groer,[31] C. Grosso-Pilcher,[5] G. Guillian,[19] R. S. Guo,[32] C. Haber,[17]

E. Hafen,[18] S. R. Hahn,[7] R. Hamilton,[11] R. Handler,[37] R. M. Hans,[38] F. Happacher,[26] K. Hara,[35] A. D. Hardman,[28] B. Harral,[25] R. M. Harris,[7] S. A. Hauger,[6] J. Hauser,[4] C. Hawk,[31] E. Hayashi,[35] J. Heinrich,[25] K. D. Hoffman,[28] M. Hohlmann,[5] C. Holck,[25] R. Hollebeek,[25] L. Holloway,[13] A. Hölscher,[14] S. Hong,[19] G. Houk,[25] P. Hu,[27] B. T. Huffman,[27] R. Hughes,[22] J. Huston,[20] J. Huth,[11] J. Hylen,[7] H. Ikeda,[35] M. Incagli,[26] J. Incandela,[7] G. Introzzi,[26] J. Iwai,[35] Y. Iwata,[12] H. Jensen,[7] U. Joshi,[7] R. W. Kadel,[17] E. Kajfasz,[24] H. Kambara,[10] T. Kamon,[33] T. Kaneko,[35] K. Karr,[36] H. Kasha,[38] Y. Kato,[23] T. A. Keaffaber,[28] L. Keeble,[9] K. Kelley,[18] R. D. Kennedy,[7] R. Kephart,[7] P. Kesten,[17] D. Kestenbaum,[11] R. M. Keup,[13] H. Keutelian,[7] F. Keyvan,[4] B. Kharadia,[13] B. J. Kim,[29] D. H. Kim,[7a] H. S. Kim,[14] S. B. Kim,[19] S. H. Kim,[35] Y. K. Kim,[17] L. Kirsch,[3] P. Koehn,[29] K. Kondo,[35] J. Konigsberg,[8] S. Kopp,[5] K. Kordas,[14] A. Korytov,[8] W. Koska,[7] E. Kovacs,[7a] W. Kowald,[6] M. Krasberg,[19] J. Kroll,[7] M. Kruse,[29] T. Kuwabara,[35] S. E. Kuhlmann,[1] E. Kuns,[31] A. T. Laasanen,[28] S. Lammel,[7] J. I. Lamoureux,[3] T. LeCompte,[1] S. Leone,[26] J. D. Lewis,[7] P. Limon,[7] M. Lindgren,[4] T. M. Liss,[13] N. Lockyer,[25] O. Long,[25] C. Loomis,[31] M. Loreti,[24] J. Lu,[33] D. Lucchesi,[26] P. Lukens,[7] S. Lusin,[37] J. Lys,[17] K. Maeshima,[7] A. Maghakian,[30] P. Maksimovic,[18] M. Mangano,[26] J. Mansour,[20] M. Mariotti,[24] J. P. Marriner,[7] A. Martin,[38] J. A. J. Matthews,[21] R. Mattingly,[18] P. McIntyre,[33] P. Melese,[30] A. Menzione,[26] E. Meschi,[26] S. Metzler,[25] C. Miao,[19] T. Miao,[7] G. Michail,[11] R. Miller,[20] H. Minato,[35] S. Miscetti,[9] M. Mishina,[16] H. Mitsushio,[35] T. Miyamoto,[35] S. Miyashita,[35] N. Moggi,[26] Y. Morita,[16] J. Mueller,[27] A. Mukherjee,[7] T. Muller,[4] P. Murat,[26] H. Nakada,[35] I. Nakano,[35] C. Nelson,[7] D. Neuberger,[4] C. Newman-Holmes,[7] C.-Y. Ngan,[18] M. Ninomiya,[35] L. Nodulman,[1] S. H. Oh,[6] K. E. Ohl,[38] T. Ohmoto,[12] T. Ohsugi,[12] R. Oishi,[35] M. Okabe,[35] T. Okusawa,[23] R. Oliveira,[25] J. Olsen,[37] C. Pagliarone,[2] R. Paoletti,[26] V. Papadimitriou,[34] S. P. Pappas,[38] N. Parashar,[26] S. Park,[7] A. Parri,[9] J. Patrick,[7] G. Pauletta,[26] M. Paulini,[17] A. Perazzo,[26] L. Pescara,[24] M. D. Peters,[17] T. J. Phillips,[6] G. Piacentino,[2] M. Pillai,[29] K. T. Pitts,[7] R. Plunkett,[7] L. Pondrom,[37] J. Proudfoot,[1] F. Ptohos,[11] G. Punzi,[26] K. Ragan,[14] D. Reher,[17]

A. Ribon,[24] F. Rimondi,[2] L. Ristori,[26] W. J. Robertson,[6] T. Rodrigo,[26] S. Rolli,[26] J. Romano,[5] L. Rosenson,[18] R. Roser,[13] W. K. Sakumoto,[29] D. Saltzberg,[5] A. Sansoni,[9] L. Santi,[26] H. Sato,[35] P. Schlabach,[7] E. E. Schmidt,[7] M. P. Schmidt,[38] A. Scribano,[26] S. Segler,[7] S. Seidel,[21] Y. Seiya,[35] G. Sganos,[14] M. D. Shapiro,[17] N. M. Shaw,[28] Q. Shen,[28] P. F. Shepard,[27] M. Shimojima,[35] M. Shochet,[5] J. Siegrist,[17] A. Sill,[34] P. Sinervo,[14] P. Singh,[27] J. Skarha,[15] K. Sliwa,[36] F. D. Snider,[15] T. Song,[19] J. Spalding,[7] T. Speer,[10] P. Sphicas,[18] F. Spinella,[26] M. Spiropulu,[11] L. Spiegel,[7] L. Stanco,[24] J. Steele,[37] A. Stefanini,[26] K. Strahl,[14] J. Strait,[7] R. Ströhmer,[7a] D. Stuart,[7] G. Sullivan,[5] A. Soumarokov,[32] K. Sumorok,[18] J. Suzuki,[35] T. Takada,[35] T. Takahashi,[23] T. Takano,[35] K. Takikawa,[35] N. Tamura,[12] B. Tannenbaum,[21] F. Tartarelli,[26] W. Taylor,[14] P. K. Teng,[32] Y. Teramoto,[23] S. Tether,[18] D. Theriot,[7] T. L. Thomas,[21] R. Thun,[19] M. Timko,[36] P. Tipton,[29] A. Titov,[30] S. Tkaczyk,[7] D. Toback,[5] K. Tollefson,[29] A. Tollestrup,[7] W. Trischuk,[14] J. F. de Troconiz,[11] S. Truitt,[19] J. Tseng,[18] N. Turini,[26] T. Uchida,[35] N. Uemura,[35] F. Ukegawa,[25] G. Unal,[25] J. Valls,[7a] S. C. van den Brink,[27] S. Vejcik, III,[19] G. Velev,[26] R. Vidal,[7] M. Vondracek,[13] D. Vucinic,[18] R. G. Wagner,[1] R. L. Wagner,[7] J. Wahl,[5] N. B. Wallace,[26] A. M. Walsh,[31] C. Wang,[6] C. H. Wang,[32] J. Wang,[5] M. J. Wang,[32] Q. F. Wang,[30] A. Warburton,[14] T. Watts,[31] R. Webb,[33] C. Wei,[6] C. Wendt,[37] H. Wenzel,[17] W. C. Wester, III,[7] A. B. Wicklund,[1] E. Wicklund,[7] R. Wilkinson,[25] H. H. Williams,[25] P. Wilson,[5] B. L. Winer,[22] D. Winn,[19] D. Wolinski,[19] J. Wolinski,[20] S. Worm,[21] X. Wu,[10] J. Wyss,[24] A. Yagil,[7] W. Yao,[17] K. Yasuoka,[35] Y. Ye,[14] G. P. Yeh,[7] P. Yeh,[32] M. Yin,[6] J. Yoh,[7] C. Yosef,[20] T. Yoshida,[23] D. Yovanovitch,[7] I. Yu,[7] L. Yu,[21] J. C. Yun,[7] A. Zanetti,[26] F. Zetti,[26] L. Zhang,[37] W. Zhang,[25] and S. Zucchelli[2]

[1] *Argonne National Laboratory, Argonne, Illinois 60439*

[2] *Istituto Nazionale di Fisica Nucleare, University of Bologna, I-40127 Bologna, Italy*

[3] *Brandeis University, Waltham, Massachusetts 02264*

[4] *University of California at Los Angeles, Los Angeles, California 90024*

[5] *University of Chicago, Chicago, Illinois 60638*

[6] *Duke University, Durham, North Carolina 28708*

[7] *Fermi National Accelerator Laboratory, Batavia, Illinois 60510*

[8] *University of Florida, Gainesville, FL 33611*

[9] *Laboratori Nazionali di Frascati, Istituto Nazionale di Fisica Nucleare, I-00044 Frascati, Italy*

[10] *University of Geneva, CH-1211 Geneva 4, Switzerland*

[11] *Harvard University, Cambridge, Massachusetts 02138*

[12] *Hiroshima University, Higashi-Hiroshima 724, Japan*

[13] *University of Illinois, Urbana, Illinois 61801*

[14] *Institute of Particle Physics, McGill University, Montreal H3A 2T8, and University of Toronto, Toronto M5S 1A7, Canada*

[15] *The Johns Hopkins University, Baltimore, Maryland 21218*

[16] *National Laboratory for High Energy Physics (KEK), Tsukuba, Ibaraki 315, Japan*

[17] *Ernest Orlando Lawrence Berkeley National Laboratory, Berkeley, California 94720*

[18] *Massachusetts Institute of Technology, Cambridge, Massachusetts 02139*

[19] *University of Michigan, Ann Arbor, Michigan 48109*

[20] *Michigan State University, East Lansing, Michigan 48824*

[21] *University of New Mexico, Albuquerque, New Mexico 87132*

[22] *The Ohio State University, Columbus, OH 43320*

[23] *Osaka City University, Osaka 588, Japan*

[24] *Universita di Padova, Istituto Nazionale di Fisica Nucleare, Sezione di Padova, I-36132 Padova, Italy*

[25] *University of Pennsylvania, Philadelphia, Pennsylvania 19104*

[26] *Istituto Nazionale di Fisica Nucleare, University and Scuola Normale Superiore of Pisa, I-56100 Pisa, Italy*

[27] *University of Pittsburgh, Pittsburgh, Pennsylvania 15270*

[28] *Purdue University, West Lafayette, Indiana 47907*

[29] *University of Rochester, Rochester, New York 14628*

[30] *Rockefeller University, New York, New York 10021*

[31] *Rutgers University, Piscataway, New Jersey 08854*

[32] *Academia Sinica, Taipei, Taiwan 11530, Republic of China*

[33] *Texas A&M University, College Station, Texas 77843*

[34] *Texas Tech University, Lubbock, Texas 79409*

[35] *University of Tsukuba, Tsukuba, Ibaraki 315, Japan*

[36] *Tufts University, Medford, Massachusetts 02155*

[37] *University of Wisconsin, Madison, Wisconsin 53806*

[38] *Yale University, New Haven, Connecticut 06511*

Chapter 1

Introduction

1.1 Large-Momentum-Transfer Production of Prompt Photons

The Quantum Chromodynamics (QCD) [1] has been successfully describing the dynamics of the collisions between hadrons. One of the key features of the theory is the property of asymptotic freedom [2][3], which describes the weakening of the effective quark-gluon coupling at short distances or, equivalently, large momentum transfers. The characteristic of asymptotic freedom allows application of perturbative techniques to the problem of short-distance interactions. The large-momentum-transfer processes in hadron-hadron collisions have played an important role in testing the QCD.

In the Collider Detector at Fermilab (CDF), various physics processes in hadron - hadron collisions were used to test the QCD; for example, lepton pair production [4], Z boson plus jet production [5], and inclusive jet cross section [6]. All of the results showed qualitative agreement with the QCD predictions.

The prompt photon production with large transverse momentum in hadron - hadron collisions is also a good probe for testing the QCD [7]. Although the cross section of the

prompt photon production is small compared with that of jet production, there is less ambiguity of the parton fragmentation processes at the final state. The momentum of the photons in the final state can be also accurately measured with the electromagnetic (EM) calorimeter which has a fine energy resolution, while the momentum of the jets must be measured with both the EM and the hadron calorimeters and the resolution of the hadron calorimeter is worse than the EM calorimeter.

Measurement of the diphoton production in hadron - hadron collisions is thus important for testing the QCD. The number of Feynman diagrams used in the QCD prediction is restricted by requiring the existence of two photons in the final state. The Feynman diagrams for the leading-order diphoton processes are shown in Fig. 1.1.

1.2 Formalism

Figure 1.2 a schematic drawing of such a high p_T process in hadron-hadron collisions, where A and B are the initial hadrons, C and D are the final state objects after the fragmentation processes. The corresponding expression for the invariant cross section of the particle C is

$$E_C \frac{d\sigma}{d^3p_C}(AB \to C + X) = \sum_{abcd} \int dx_a dx_b dz_c G_{a/A}(x_a, Q^2) G_{b/B}(x_b, Q^2) D_{C/c}(z_c, Q^2) \times \frac{\hat{s}}{z_c^2 \pi} \frac{d\sigma}{d\hat{t}}(ab \to cd) \delta(\hat{s} + \hat{t} + \hat{u}) \,, \quad (1.1)$$

where p_C is the momentum of outgoing particle C, x_a and x_b are the momentum fractions of the partons a and b with respect to the initial hadrons A and B, Q^2 is the momentum transfer in the collision, $G_{a/A}(x_a, Q^2)$ and $G_{b/B}(x_b, Q^2)$ are the distribution functions of the partons a and b, respectively, $D_{C/c}(z_c, Q^2)$ is the fragmentation function of the particle C from parton c, $\hat{s}$, $\hat{t}$ and $\hat{u}$ are the Mandelstam variables for the hard collision of the partons $ab \to cd$, $\frac{d\sigma}{d\hat{t}}$ is the differential cross section for the two-body parton scattering subprocess.

Theoretical efforts on the parametrizations of a set of Q^2-dependent parton distribu-

tion functions have been made for the physics processes in high energy hadron-hadron collisions using the data from deep inelastic scattering, J/Ψ and high-mass dilepton production [8], where the Q^2 evolution of these distribution functions are calculated with the Altarelli-Parisi equations [9]. The global fits to the recent results from various experiments (deep inelastic experiments, lepton-pair production experiments and direct photon production experiments), have been also done to determine more sophisticated parton distribution functions [10].

1.3 Leading Order and Next-to-Leading Order QCD Predictions

The invariant cross sections for the leading-order subprocesses shown in Fig. 1.1 are given in [7].

The next-to-leading order (NLO) QCD prediction for the diphoton production was evaluated by Bailey *et al.* [11]. Following diphoton processes were included in this calculation:

1. leading order Born process (Fig. 1.1 (a)),
2. leading order Box process (Fig. 1.1 (b)),
3. contributions of single- and double-photon bremsstrahlung; this item includes both 3-body and 4-body final states and also the collinear pieces that use photon fragmentation functions. The photon fragmentation functions are evolved with Q^2 just as the usual hadronic fragmentation functions are done [7]. (Fig. 1.3),
4. Born processes with one virtual gluon exchange (Fig. 1.4),
5. Born processes with one real gluon emission (Fig. 1.5).

Single-photon bremsstrahlung contribution to the diphoton production was calculated using the $2\rightarrow2$ direct photon subprocess cross sections. Double-photon bremsstrahlung

process was also calculated using the 2→2 QCD subprocess cross sections. In the 2→3 and the 2→4 QCD subprocesses, 3-body and 4-body phase spaces were evaluated with the Monte Carlo techniques [11].

Figure 1.6 shows the theoretical prediction for the NLO QCD calculations as a function of the transverse momentum (p_T) of the photons. Here we put two entries in one event. The momentum transfer Q^2 was chosen to be the p_T^2 of the leading photons. In this calculation we used CTEQ2M parton distribution functions [10]. The energy isolation cut which was used in this analysis of the experimental data was applied to this calculation. The NLO calculation indicates that we will have diphoton events up to around 70 GeV with the integrated luminosity of 110 pb^{-1}, assuming the acceptance of the photon detection to be 1.

1.4 Study of the Background for Higgs Boson Hunting

The QCD diphoton production is considered to be the only dominant physics background for search for the Higgs bosons decaying to two-photons with large transverse momentum [12] at future hadron colliders, such as LHC. The consistency between the experimental result of the diphoton cross section and the theory should be checked for the background study of this decay mode. The CDF and DØ experiments are currently the only experiments capable of doing this study.

1.5 Initial Soft Gluon Radiation and Intrinsic k_T Smearing

The recent result of the inclusive photon cross section measured at CDF [13] shows that the result is in agreement with the NLO QCD prediction but has a steeper slope than the theory at low p_T region. Figure 1.7 shows the result of the inclusive photon cross

section as a function of p_T of the photons, where (data - theory)/theory is shown in linear scale. The CTEQ group reported that such a shape was seen in other inclusive photon measurements at various fixed target experiments, and one of the idea to understand the shape was that the shape could be occurred by the transverse momentum of the initial partons, which is caused by multiple initial soft gluon radiations, as well as the intrinsic transverse momentum of the partons in the hadrons. In the parton model approach it is assumed that the average value of the intrinsic transverse momentum $< k_T >$ reflects the size of the hadron via the uncertainty principle. This leads to the expectation that $< k_T >$ may be in the range of several hundred MeV [7]. Both effects are beyond the NLO calculation. The p_T distribution of the photons is smeared by these effects. Theoretical efforts for explaining the slope of the inclusive photon cross section are in progress with the help of the Monte Carlo techniques which take these effects into account [15].

The diphoton production in hadron - hadron collisions is one of the clear probe for measuring these gluon radiations and intrinsic transverse momentum, by measuring the p_T of the diphoton system, which corresponds to the p_T of the system of the initial partons.

1.6 Previous Results of Diphoton Cross Section

There are many experimental results of measuring the cross section for prompt photon production. The review by Ferbel and Molzon [16] presents a summary of the results of the early experiments with fixed targets and the comparison of the data with the early theoretical works described in [7].

The first measurements of the diphoton cross section in $\bar{\mathrm{p}}\mathrm{p}$ collisions were done at UA2 and UA1 collaboration with CERN Sp$\bar{\mathrm{p}}$S collider at $\sqrt{\mathrm{s}} = 630\,\mathrm{GeV}$ [17][18]. UA2 presented data with large statistics, which were in agreement with the NLO QCD prediction.

p_T bin (GeV/c)	Mean p_T (GeV/c)	$d\sigma_{\gamma\gamma}/dp_T$(pb/GeV/c)	Stat. (%)	Sys. (%)
10-12	11.1	17.5	57	+31 -21
12-15	13.5	11.6	46	+45 -35
15-19	17.4	4.2	65	+41 -29
10-19	13.3	9.6	31	+37 -27

Table 1.1: The diphoton cross section as a function of photon p_T from the total integrated luminosity of $4.3\,\mathrm{pb}^{-1}$. Statistical and systematic errors are also listed.

CDF already published the result of the diphoton cross section with the total accumulated luminosity of $4.3\,\mathrm{pb}^{-1}$ [19]. Figure 1.8 shows the result of the cross section as a function of the transverse momentum of the photons. The numerical values for the cross section are shown in Table 1.1 with statistical and systematic errors. The central values of the measured cross section were about 3 times higher than the NLO QCD prediction, although the errors were large.

1.7 Other Topics on Diphoton Production

In 1996, CDF detected a diphoton candidate event, which also contained one electron and one "electron like" particle, and large missing E_T. CDF has investigated the event in various aspects. The diphoton group looked at a missing E_T distribution of "diphoton plus missing E_T" events [20]. It was reported that the shape of missing E_T distribution for diphoton events was consistent with that of Drell-Yan events.

1.8 Outline of the Thesis

In this thesis we present the result of the measurement of the cross section for diphoton production at a center-of-mass energy $\sqrt{s} = 1.8$ TeV. The data were accumulated using CDF detector. The total integrated luminosity was about $110\,\mathrm{pb}^{-1}$ during 1992-1995 Fermilab Tevatron collider run. The components of the CDF detector relevant to

this analysis are described in Chapter 2, including the trigger system. In Chapter 3 we describe the criteria for selecting diphoton candidates, and evaluation of their efficiencies for real diphoton events. Chapter 4 describes the separation of the prompt diphotons from neutral mesons decaying to multiple photons. Since the backgrounds are not discriminated from real diphoton signals on event-by-event basis, we used a statistical method using the information from the electromagnetic shower profile at the shower maximum region and the conversion rates in front of the calorimeter. In Chapter 5, we evaluate the photon fraction in the final diphoton candidates, and we present the differential diphoton cross section as a function of transverse momentum of the photons, invariant mass of the diphotons, azimuthal angle between two photons, the ratio of p_T for diphotons $(Z = p_T^{(2)}/p_T^{(1)})$, and transverse momentum of the diphoton system. The results are compared with the NLO QCD prediction. Systematic uncertainties in the cross section measurement are also discussed. Finally we conclude in Chapter 6.

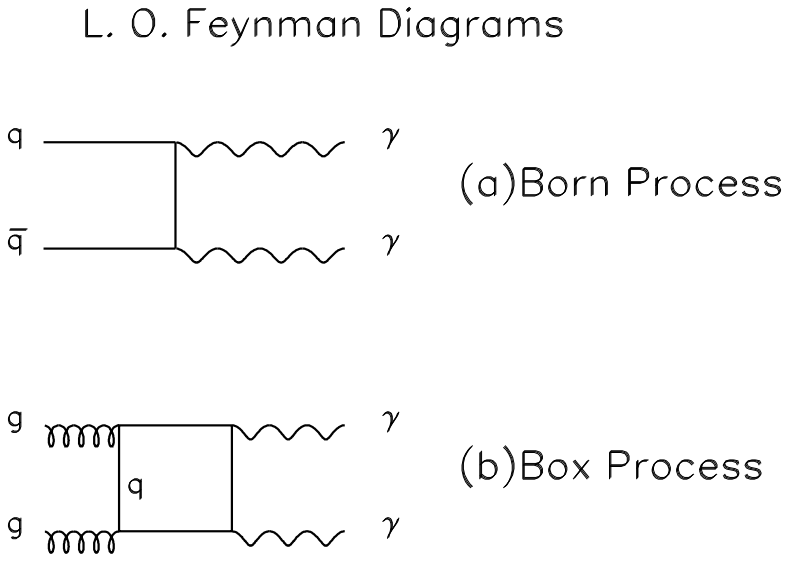

Figure 1.1: Leading-order Feynman diagrams for diphoton production, (a) Born process, (b) Box process.

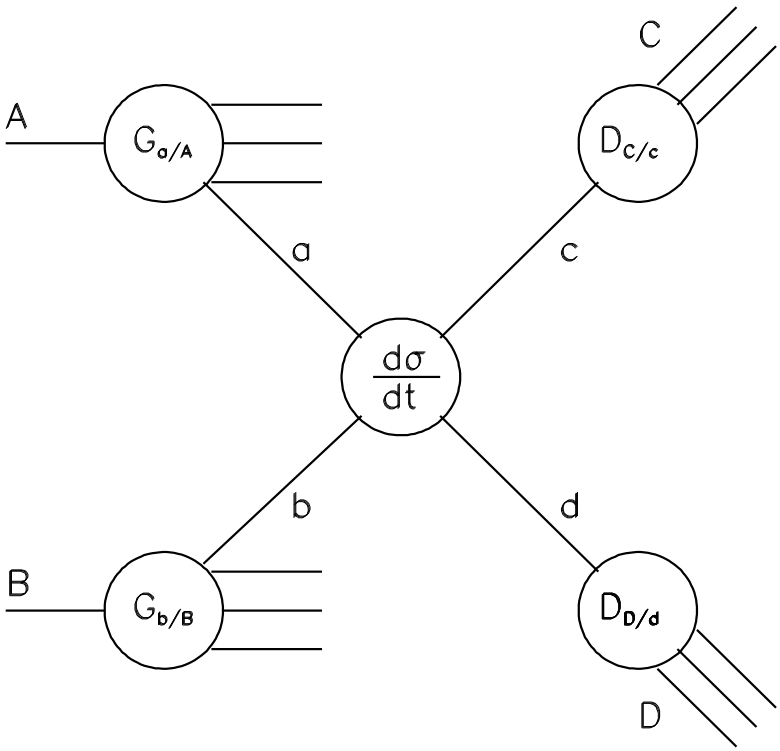

Figure 1.2: Schematic drawing of a high p_T reaction factorized into parton distribution functions (G), parton fragmentation functions (D), and a hard scattering subprocess.

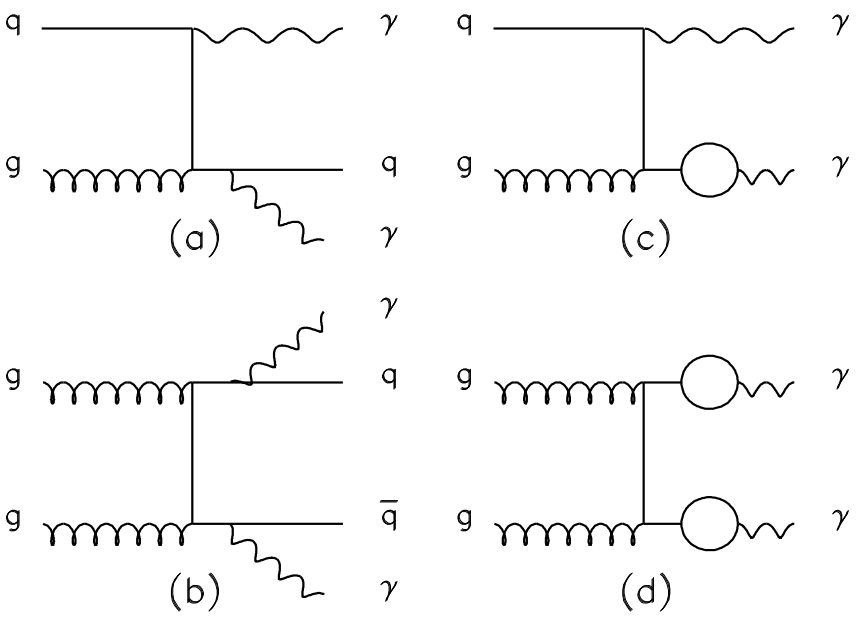

Figure 1.3: Feynman diagrams used in the NLO prediction for diphoton production from the contributions of (a) one photon bremsstrahlung process, (b) diphoton bremsstrahlung process, (c) one photon fragmentation process and (d) diphoton fragmentation process. The circle shows the fragmentation process for the final state quark.

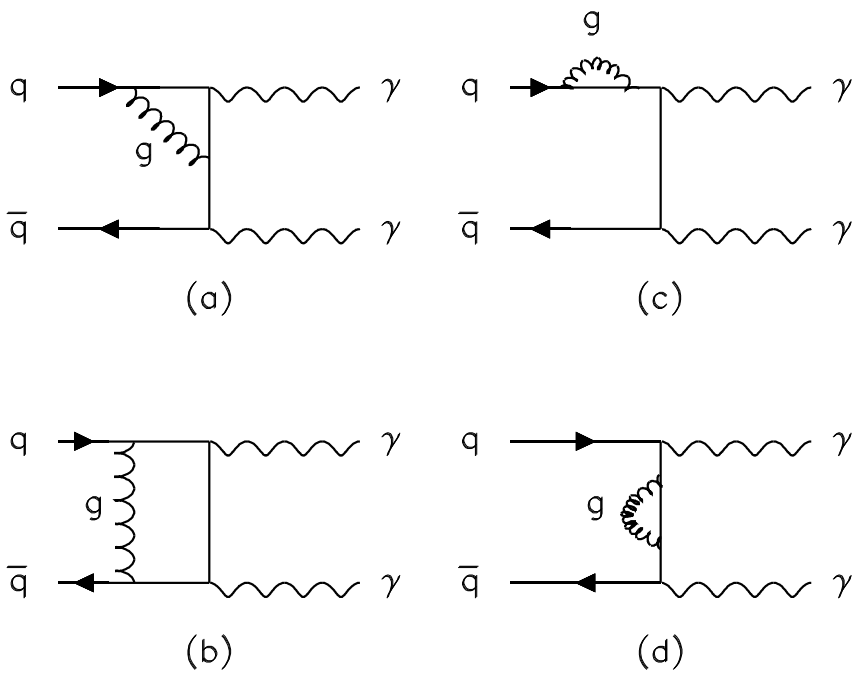

Figure 1.4: Feynman diagrams used in the NLO prediction for diphoton production with one virtual gluon exchange.

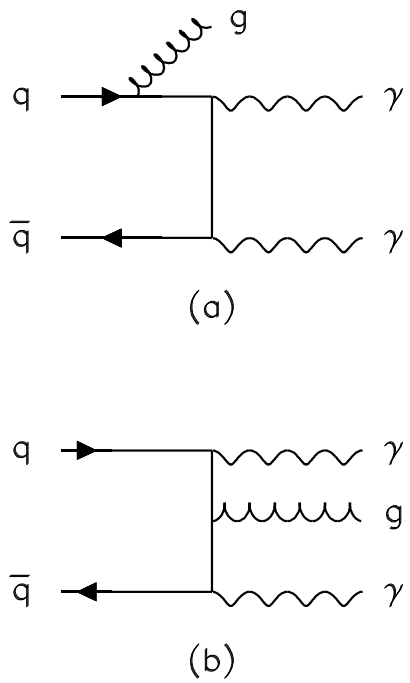

Figure 1.5: Feynman diagrams used in the NLO prediction for diphoton production with one real gluon emission.

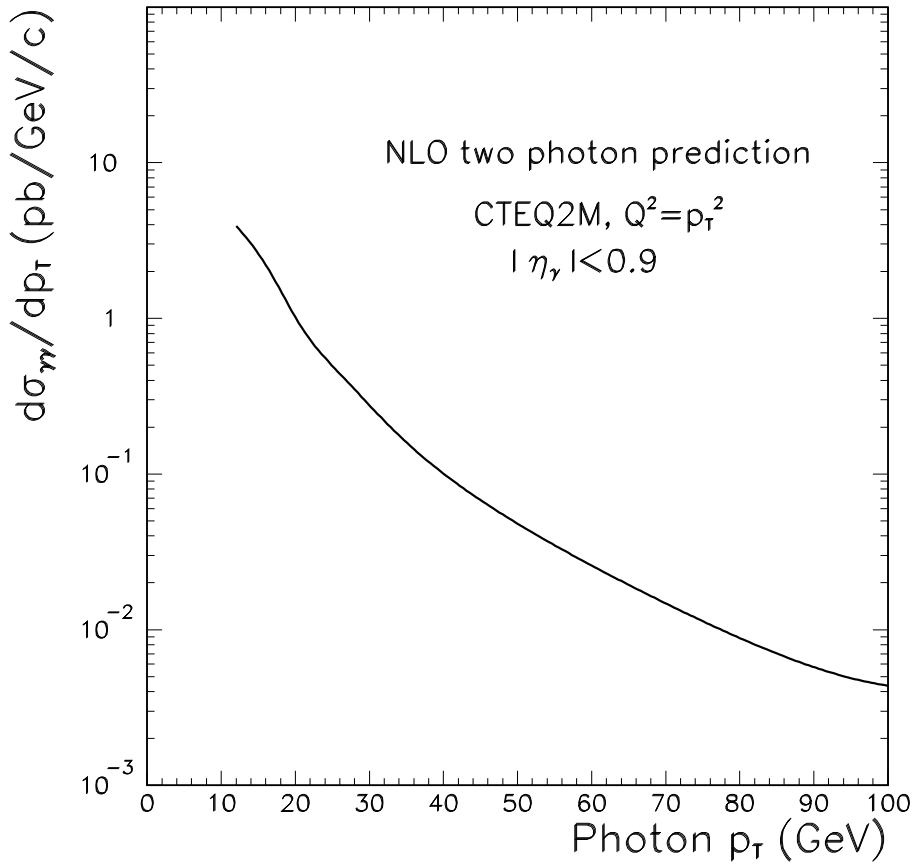

Figure 1.6: The prediction of the diphoton cross section of the NLO calculation, as a function of the transverse momentum of the photons.

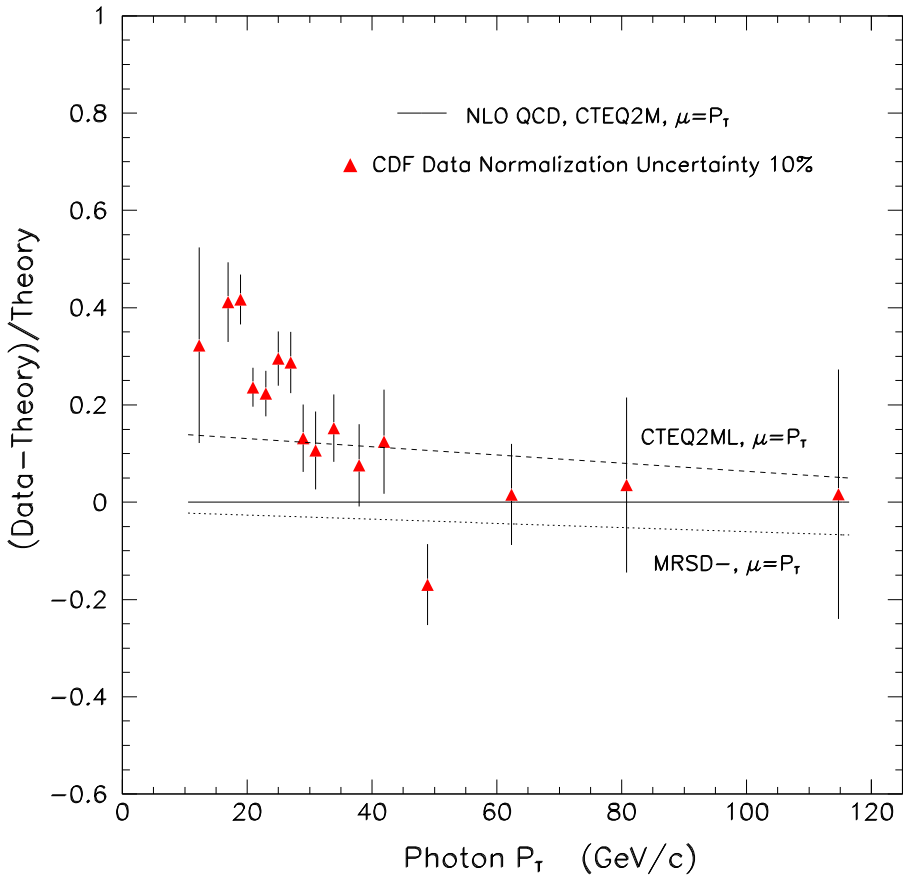

Figure 1.7: The result of the inclusive photon cross section measurement at CDF as a function of p_T of the photons, where (data-theory)/theory is plotted. Variations from different parton distribution functions are also shown. The solid line shows the NLO prediction with CTEQ2M parton distribution functions, the dashed line shows that with CTEQ2ML, the dotted line shows that with MRSD- parton distribution functions.

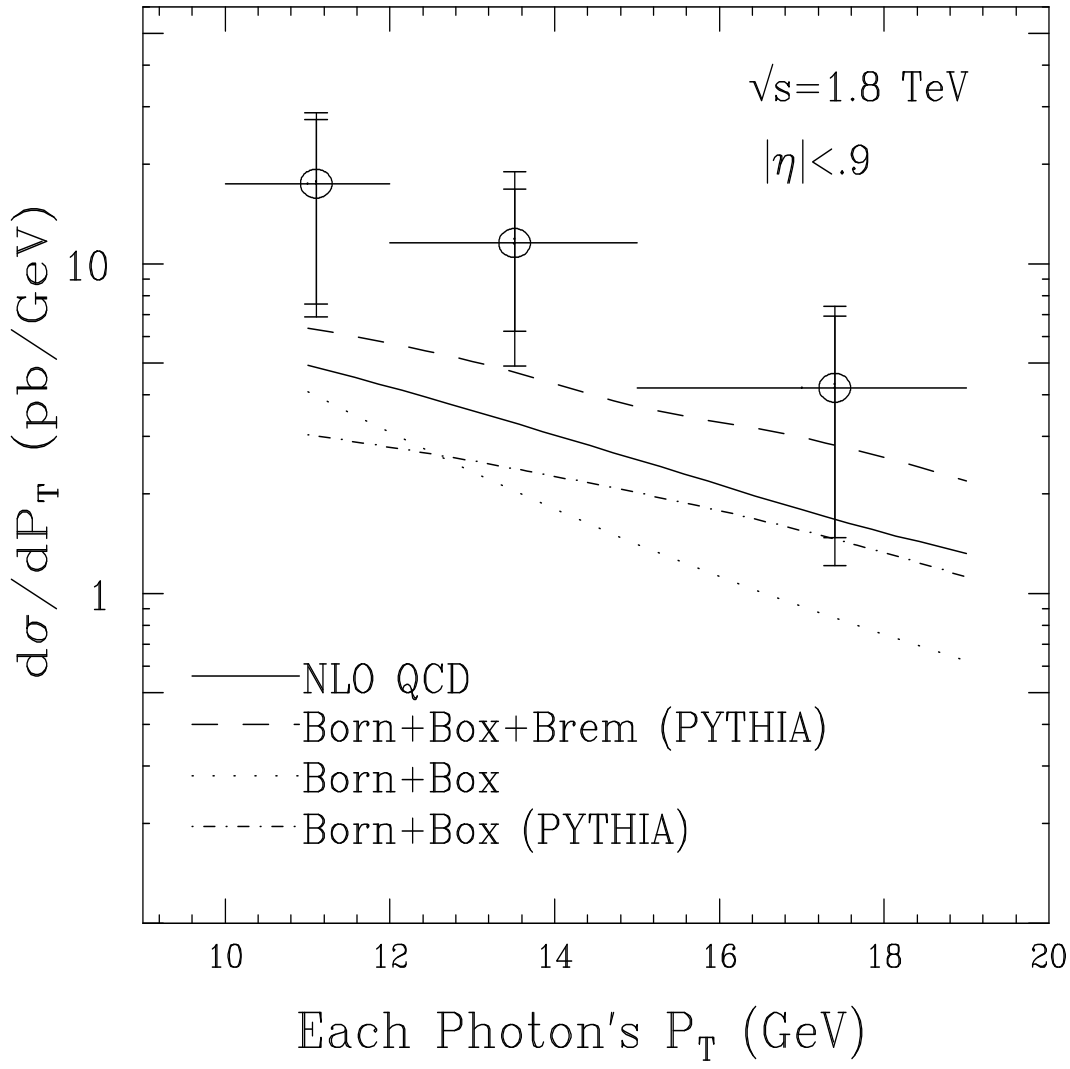

Figure 1.8: The published result of the diphoton cross section as a function of the photon p_T measured at CDF. The total accumulated luminosity was 4.3pb^{-1}. The data were compared with the NLO(solid), LO(dotted) QCD predictions, PYTHIA LO with (dashed) and without (dot-dashed) bremsstrahlung contributions.

Chapter 2

The CDF Detector

In this chapter we describe the experimental apparatus, the Collider Detector at Fermilab (CDF) , with emphasis on the central part of the CDF detector, especially for the central electromagnetic calorimeter, where our sample of the diphoton candidates is selected and used for the study of the diphoton cross section.

The CDF detector [21] is a general purpose solenoidal detector which was designed for studying the proton-antiproton collisions at the center of mass energy of 1.8 TeV. The detector covers almost of the 4π solid angle, down to 2° with respect to the beam direction and 2π in azimuth. It consists of three parts, central, forward and backward, as shown in Figure 2.1.

The apparatus is divided in roughly three categories; tracking device, calorimeters and the muon detection system. The tracking systems measure the tracks of individual charged particles. The calorimeters are used to measure the energy deposition of particles from the collision. The muon system is designed to detect the charged particles penetrating the calorimeters.

2.1 Tracking chambers

In the central region of the detector (Figure 2.2), tracking chambers reside within a 1.4 T solenoid coil [22]. They allow precise momentum analysis of charged particles. We describe the three tracking chamber systems below.

2.1.1 Silicon Vertex Detector: SVX

The silicon vertex detector (SVX) was installed at the beginning of the 1992 collider run, which was designed to detect the secondary vertices which were caused by the Lorentz boost of heavy mesons with long lifetimes, especially mesons from b quark fragmentations.

The SVX is 51 cm long and consists of two barrel modules contacting at $z = 0$ cm. Each barrel consists of four concentric cylindrical layers of DC-coupled silicon microstrips. The layers are located surrounding the beam pipe: 3.005 cm from the beam line for the innermost layer, 4.256 and 5.687 cm for the middle two layers, and 7.866 cm for the outermost layer. The silicon microstrips are 8.5 cm long and 300 μm thick with a strip pitch of 60 μm for the inner three layers and 55 μm for the fourth layer. The tracks of the charged particles in $R - \phi$ plane are reconstructed with the charge distribution of each layer. The position resolution of the SVX in the $R - \phi$ plane is about 13 μm at a track transverse momentum of 3.5 GeV/c.

The informations from the SVX are used to determine the track parameters of the charged particles with the CTC as follows: first all tracks are reconstructed only with CTC, then the tracks are extrapolated to each SVX layer. At least 2 hits in the four layers are required to reconstruct the track parameters with both CTC and SVX informations. The stand-alone reconstruction of the track parameters with SVX is not done.

2.1.2 Vertex time projection chamber: VTX

The vertex time projection chamber (VTX) is located just outside the SVX. After 1988-1989 CDF collider run, the VTX was installed by replacing the similar chamber called VTPC [23].

The VTX consists of 28 time projection chamber modules along the beam direction z, and has a good track reconstruction capability in R-z plane. The main role of the VTX is to determine the primary event vertex along the beam axis. The VTX determines the event z vertex with an accuracy of about 3 mm.

2.1.3 Central tracking chamber: CTC

The central tracking chamber (CTC) [24] is a large cylindrical drift chamber, 1.3 m in diameter and 3.2 m long (figure 2.3). It is located outside the VTX and covers the angular region $40° < \theta < 140°$ ($-1 < \eta < 1$, where the pseudorapidity η is defined in the next section). The chamber consists of 84 layers of sense wires grouped into 9 "superlayers". Five of them consist of 12 axial wires, and four of them consist of 6 stereo wires which have angles of $\pm 3°$ relative to the beam direction. The resolution of a single hit point is about 200 μm, and the CTC provides a momentum resolution of

$$\Delta p_T / p_T \simeq 0.002\, p_T, \tag{2.1}$$

where p_T is the transverse momentum of a charged particle in GeV/c.

2.2 Calorimetry

A calorimetric device plays an important role in high energy experiments, especially in hadron collider experiments. This is because it can measure the energy of neutral particles as well as charged particles. Identification of a particular class of particles, an electron or photon for example, is also possible. Especially for the electromagnetic

calorimeters, the resolution of the particle energy becomes more precise at high energy, which enables us to make the resolution of the various physics variables (momentum of the electrons, the invariant mass of the two electron pair, etc.) more precise than that from CTC.

The CDF calorimeters are segmented into towers with projective geometry; each tower points back to the nominal interaction point. The size of the tower is typically 15 degrees in azimuth and 0.1 in pseudorapidity η. The pseudorapidity η is defined by $\eta = -\ln\tan\theta/2$, where θ is the polar angle with respect to the proton beam direction (z). The pseudorapidity η rather than θ is used as the tower segmentation variable because the distributions of any particles or hadronic jets in hadron colliders are roughly flat in this variable.

The CDF calorimeters consist of three parts (central, plug and forward) depending on the angular region. Each calorimeter has two longitudinal components, the electromagnetic in front and the hadronic behind. In this way an electromagnetic shower can be separated from a hadronic shower, because an electromagnetic (hadronic) shower has a faster (slower) development as a function of the amount of materials a particle passes through. All CDF calorimeters are of the sampling type, which consists of a passive absorber to create particle showers and an active medium to detect secondary particles in the showers.

2.2.1 Central electromagnetic calorimeter: CEM

The CDF central electromagnetic calorimeter (CEM) [25] consists of alternative layers of a plastic scintillator as a sampling medium and a lead sheet as a showering material. It is segmented into 24 modules in azimuth, and two along the beam direction, comprising a total of 48 wedge shaped modules (Figure 2.4). A "wedge" module has 10 towers, each of which covers 15 degrees in azimuth and 0.1 in η.

The CEM has 31 scintillator layers and 30 lead layers, corresponding to a total amount of materials of 16 radiation lengths (X_0). The layers are placed parallel to the

beam line.

A typical size of a tower cell is 46 cm in the ϕ direction (denoted by X in Fig. 2.4) and 24 cm along the beam direction z. This is larger than the size of the electromagnetic showers, which is only a few cm's wide laterally.

Each of the CEM towers is calibrated using an electron beam of 50 GeV momentum. The calibration is maintained using ^{137}Cs radioactive sources for the overall calorimeter response and the LED and Xenon flasher system for the phototubes and lightguides.

The energy resolution of the CEM is measured using the test beam electrons to be

$$\frac{\sigma(E)}{E} = \frac{0.135}{\sqrt{E \sin\theta}}, \tag{2.2}$$

where E is the energy measured in GeV and θ is the polar angle. The dependence on the polar angle is due to the increase in the absorber thickness in lower angle towers.

2.2.2 Central strip chambers: CES

A layer of wire proportional chamber (CES) is placed at approximate shower maximum of the CEM (nominal depth at 5.9 X_0 including the coil). A chamber has two orthogonal views, anode wires measuring the R-ϕ view of the showers and cathode strips measuring the z view. A channel has a typical width of 1.5 cm. The fine segmentation enables us to measure more precise profiles of showers than with CEM towers. We use 11 channels to make a cluster in both wire and strip view. The shower position is determined by the position of the cluster. The position resolution of a few mm's is achieved for electromagnetic showers.

In the physics analysis, we use the local coordinates in the CES module to define the fiducial volume of each CES module. Figure 2.5 shows a schematic drawing of the CES local coordinates.

2.2.3 Central Preradiator Detector: CPR

The central preradiator detector (CPR) [26] was installed at the beginning of the 1992 collider run to detect the particle showers started by the preshower materials (coil and cryostat) placed in front of the CEM. The output charge from the CPR enables us to get information for estimating conversion probability of the electrons, photons and pions, which become the information for extracting electrons/photons from background hadrons. Thus the CPR plays an important role in this analysis.

The CPR consists of multi-wire proportional chambers as a detection device. There are two MWPC modules located in front of each CEM wedge. In each CPR module there are 32 sense wires and 31 field wires which are along the z axis. The total amount of the material of the CPR is about 3% of a radiation length and 1% of an interaction length.

Following is the procedure of the CPR clustering. The signal of the CPR from a particle depends on the conversion probability of the particle. If the particle starts a shower in front of the CPR, we have the CPR signal, if not, we do not have the signal. We use the shower position which is determined from the CES, and the Z vertex position from the VTX, to interpolate the corresponding position at the CPR module. Then we find a CPR channel with the highest charge output within five channels from the interpolated position, which we regard as the seed channel. The clustering includes 5 channels centered on the seed.

2.2.4 Central and Wall Hadron Calorimeter: CHA/WHA

Behind the CEM there exist the central (CHA) and the wall (WHA) hadron calorimeters [29]. They both consist of layers of plastic scintillator and iron absorber. Towers have the same segmentation as the CEM.

2.2.5 Plug and Forward Calorimeters

Calorimeters covering the plug ($1.1 < |\eta| < 2.4$) and forward ($2.2 < |\eta| < 4.2$) regions of the detector employ gas proportional chambers with cathode pad readout as a detection device, and lead and iron plates as showering materials for electromagnetic and hadron components, respectively. A tower size of $\Delta\eta \times \Delta\phi = 0.1 \times 5^\circ$ is used.

2.3 Trigger and Data Acquisition System

2.3.1 Trigger System

The CDF trigger is divided in four levels, level 0, 1, 2 and 3. The level 0 trigger requires a signature of an inelastic collision, which is defined by the coincidence of the beam-beam counter (BBC) systems. The BBC consists of scintillator hodoscopes located in front of the forward and the backward detectors.

The level 1 and 2 triggers use signals from the calorimeters and the tracking chambers to make decisions on the events. Calorimeter signals are summed into trigger towers with a size of $\Delta\eta \times \Delta\phi = 0.2 \times 15^\circ$. In this way the whole CDF calorimeter is represented by a 42×24 array for both electromagnetic and hadronic energies.

The level 1 trigger makes a decision based on calorimeter signals in excess of a programmable threshold, a stiff CTC track from a fast hardware track processor [30], and the muon triggers [31]. The level 2 trigger can form clusters of energies using the 42×24 array. The extra module for isolation cut is used in the triggers for electrons and photons, which is described in the next section.

The level 3 trigger system performs a more sophisticated event selection by executing FORTRAN-77 programs in the UNIX-based data acquisition machines.

The trigger system for diphotons used in this analysis will be described in detail in Chapter 3.

2.3.2 Neural Network Hardware Trigger for Isolation Cut at Level 2

In 1992-1995 collider run, a hardware trigger module for isolation cut was installed for electron and photon selection [32], which consists of special IC chips used for the Neural Network (NN) system.

The trigger system was used as follows: first the IC chips study the isolation pattern around the trigger tower using the simulations, then the simple pattern recognition was used to discriminate the non-isolated events at the hardware trigger level. More details can be seen in [32].

2.4 Luminosity Measurement

The luminosity is obtained by counting the event rate using the BBC:

$$L = \frac{R_{BBC}}{\sigma_{BBC}}, \tag{2.3}$$

where L is the luminosity, R_{BBC} is the BBC event rate, and σ_{BBC} is the effective cross section of visible to the BBC's.

The effective cross section is obtained by using the $\bar{p}p$ total cross section measured by using the luminosity-independent method [33]. The value of σ_{BBC} can be expressed as

$$\sigma_{BBC} = \sigma_{TOT} \times \frac{R_{BBC}}{R_{TOT}} \tag{2.4}$$

where σ_{TOT} is the $\bar{p}p$ total cross section, R_{TOT} is the sum of the elastic and inelastic event rates measured in the CDF. Using recent direct measurements of the elastic and total cross sections by CDF [34], the BBC cross section was obtained as

$$\sigma_{BBC} = 51.2 \pm 1.7\,\text{mb}. \tag{2.5}$$

After accounting for possible backgrounds in the BBC's, we obtain [35]

$$\int L dt = 110 \pm 9 \mathrm{pb}^{-1}. \tag{2.6}$$

The systematic uncertainty in the luminosity measurement is 8%.

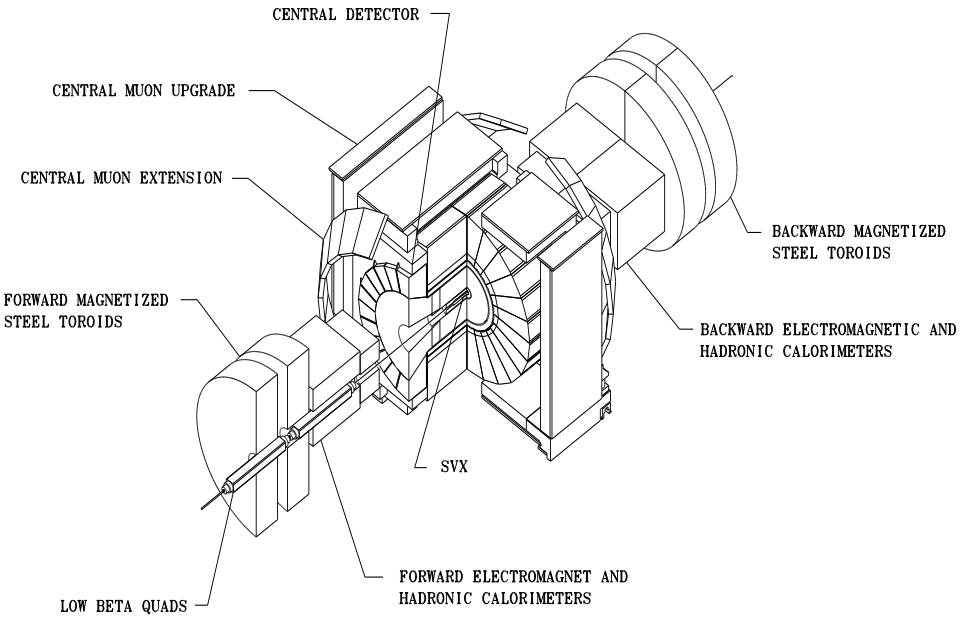

Figure 2.1: Schematic perspective view of the CDF detector.

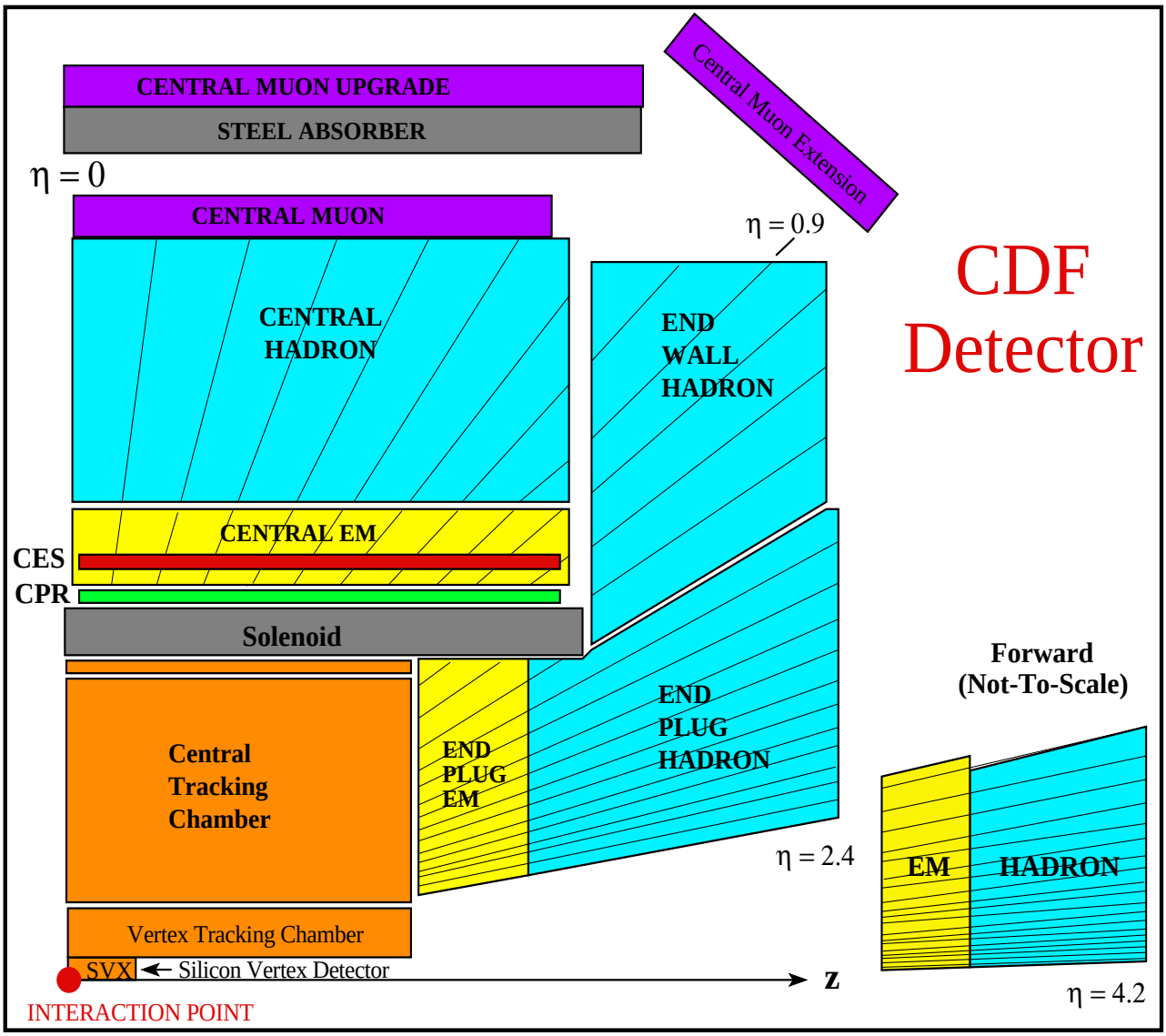

Figure 2.2: Schematic quarter section of the CDF detector.

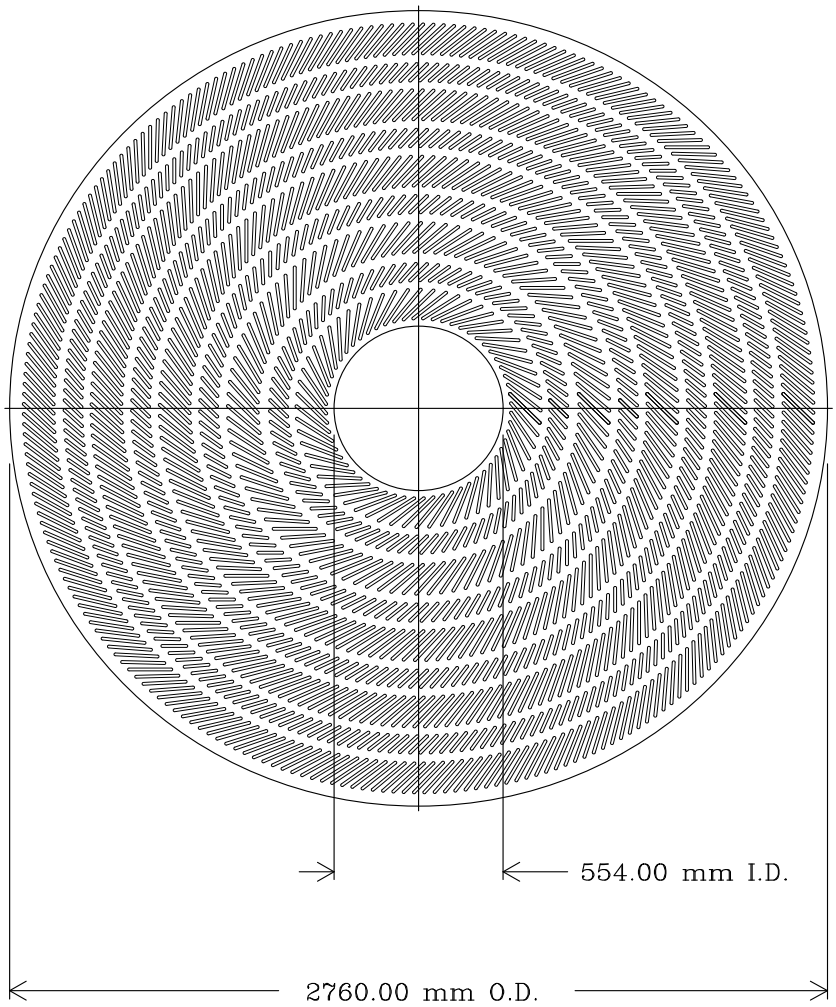

Figure 2.3: Schematic view of an endplate of the CTC showing the arrangement of the blocks which hold the 84 layers of sense wires.

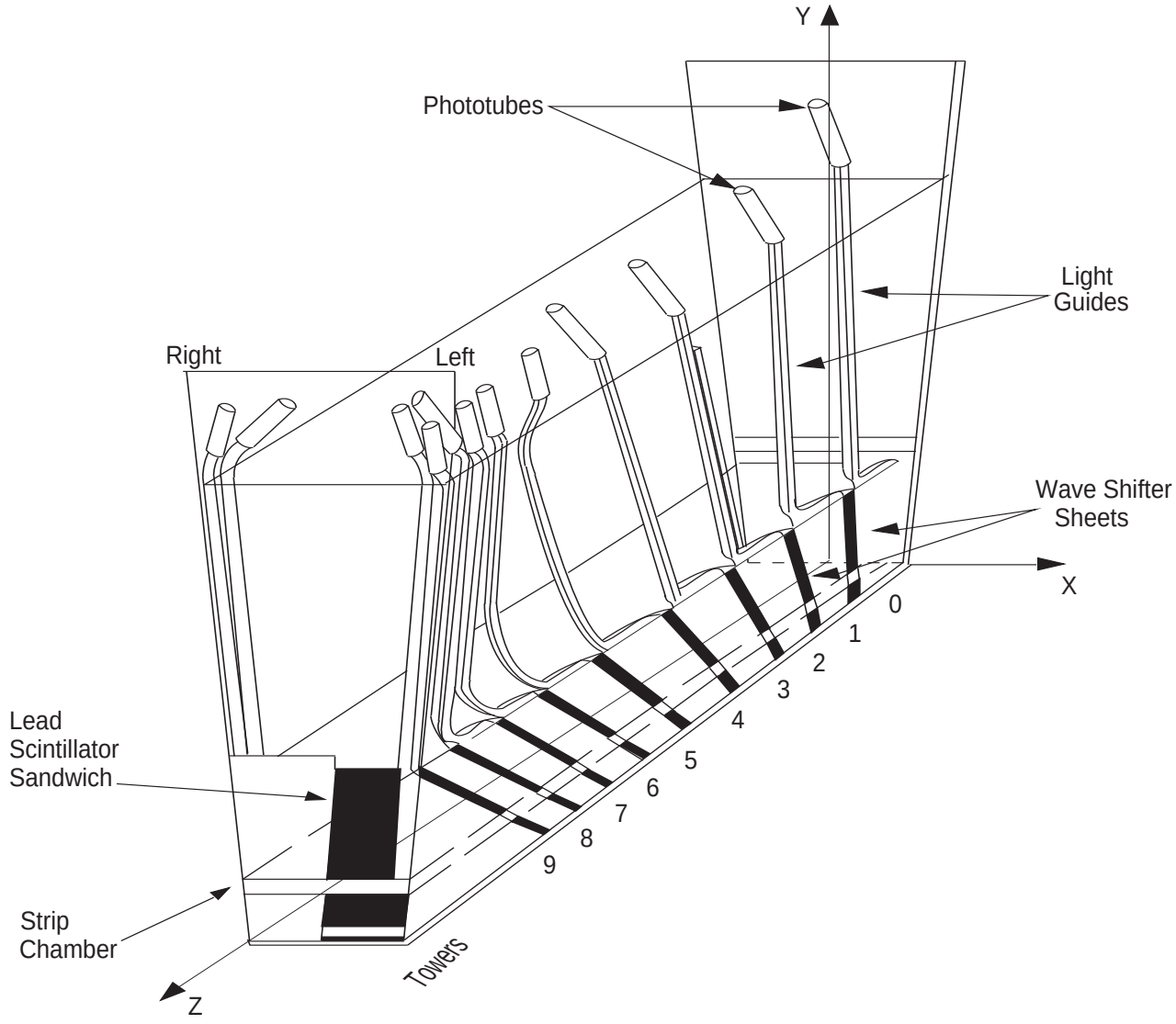

Figure 2.4: A module of the central electromagnetic calorimeter (CEM).

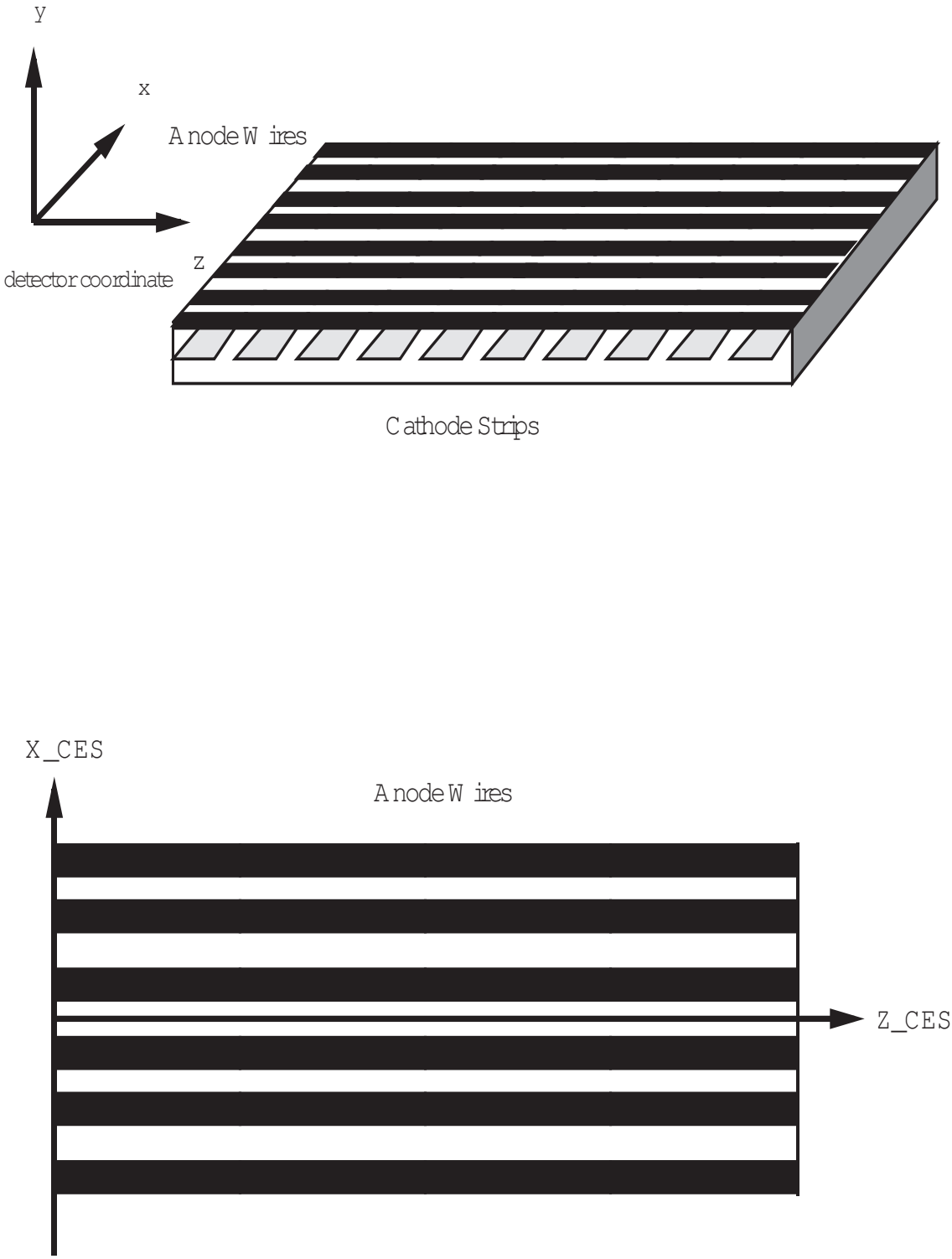

Figure 2.5: Schematic drawings of the CES and its local coordinates.

Chapter 3

Event Selection

In this chapter we present the criteria for selecting diphoton candidates from the CDF data, and their efficiencies for real diphoton events.

We select the events with two EM clusters, both of which do not have 3D tracks pointing at them. The CTC covers the region of $|\eta| \leq 1.0$. So we use only the central volume of the CDF detector.

3.1 Cluster Finding Algorithm

The signature of the prompt diphoton production is two large and isolated electromagnetic energy depositions in the calorimeters. The CDF diphoton trigger finds this signature to acquire the data.

In order to reconstruct the correct energy for electrons and photons from energy depositions in each CEM tower, clustering of the energy depositions is needed. The clustering algorithm is as follows; first we look for the EM towers above the threshold energy (typically 3 GeV in the transverse energy), which will be the seed towers of the EM clusters. Then we add the energy depositions of the two adjacent towers along the z axis (energy threshold is typically 0.1 GeV in the transverse view). The cluster width is, therefore, $\Delta\phi = 15^\circ$ and $\Delta\eta = 0.3$. Thus the clustered energy $E^{cluster}$ is denoted

by

$$E^{cluster} = E^{seed}_{\eta=\eta_s} + E_{\eta=\eta_s-0.1} + E_{\eta=\eta_s+0.1}, \tag{3.1}$$

where η_s is the pseudorapidity of the seed tower. This calculation is done for each EM seed tower.

At the level 2, the transverse energy is calculated using detector pseudorapidity of the seed tower, assuming that the corresponding particle comes from $z = 0$, that is, the collision occurs at the center of the detector,

$$E_T = 2E \arctan(e^{-\eta}) \tag{3.2}$$

where E is the total deposited energy in a cluster, η is the pseudorapidity of the seed tower.

At the level 3 and offline level, we have information of the event vertices along the z-axis from the VTX and of the position of the EM showers from the CES. The polar angle of an EM cluster is calculated from the event vertex position measured in the VTX and the EM shower position measured in the CES. The transverse energy is calculated by

$$\begin{aligned} E_T &= E \times \sin\theta \\ &= E \times \frac{\sqrt{R^2_{CES} + X^2_{CES}}}{\sqrt{R^2_{CES} + X^2_{CES} + Z^2_{vetex}}}, \end{aligned} \tag{3.3}$$

where E is the total deposited energy of the cluster, R_{CES} is the radius of the CES cylinder, X_{CES} is the x position in the CES coordinate measured by the CES wire chamber (see Chapter 2), and Z_{vertex} is the z position of the event vertex reconstructed by the VTX.

3.2 Trigger Requirement

The CDF trigger system consists of various physics triggers. The lowest physics trigger is called "minimum bias trigger", which is used to check the detector system or to evaluate the efficiency for the event selection used in the physics analysis. The physics trigger has a rank from level 1 to level 3.

We used the diphoton trigger system to select the diphoton dataset.

3.2.1 Level 1 Trigger Requirement

The level 1 trigger consists of the hardware modules. At this trigger the events were required to have at least one tower with transverse energy E_T more than 8 GeV.

3.2.2 Level 2 Trigger Requirement

The level 2 trigger consists of the hardware modules, and the trigger for diphotons consists of two criteria; one is E_T and the other is isolation. This trigger first requires that events have two central EM clusters both of which have E_T above 10 GeV.

At the level 2, the hardware trigger requires the event;

1. to have the 2 clusters in the detector region $|\eta| \leq 1.19$,
2. to have the transverse energy $E_T \geq 10\,\mathrm{GeV}$,
3. to have the ratio of the total transverse energy and the electromagnetic energy to be near 1;
   $E_{T,TOT} \,/\, E_{T,EM} \leq 1.125$,
4. that the two clusters are isolated in the calorimeter; at this level we require a loose isolation using the neural network trigger; the requirement is roughly equivalent to the isolation energy of 3×3 towers surrounding the trigger tower less than about 5 GeV.

item
level 3 diphoton trigger
3D tracks pointing at the EM cluster to be 0 or 1

Table 3.1: Criteria for the diphoton dataset.

3.2.3 Level 3 Trigger Requirement

The level 3 trigger consists of the online software systems. The data are processed by the online software and various sophisticated variables (3D tracks, z vertices, shower position at the CES, *etc.*) are calculated. We require that

1. the CEM clusters lie within the fiducial area in CES coordinate; $|x| \leq 17.5\,\mathrm{cm}$ and $14.5\,\mathrm{cm} \leq |z| \leq 217.0\,\mathrm{cm}$,

2. there are at least two CEM clusters with $E_{\mathrm{T}} \geq 10\,\mathrm{GeV}$.

3.2.4 Diphoton Dataset

We made the diphoton dataset with the events which passed the level 3 trigger. Table 3.1 shows the criteria applied to the events which passed the level 3 trigger.

We took all combinations of the EM clusters if there are more than two EM clusters in an event. We had 71206 EM-pair entries in the dataset.

Figure 3.1 shows the E_T distributions of the leading and next leading EM clusters in the EM pairs. Since all combinations of the EM clusters in one event are booked, there are some entries below the trigger threshold. For example, if there are four EM clusters in an event, we have six EM-pairs in an event (i.e., we have six entries in the diphoton dataset from this event) , and at least the two highest EM clusters are above the trigger threshold, therefore the EM-pairs including the third or fourth EM cluster may have the entries below the trigger threshold. Since the diphoton triggers do not require the 3D tracks to the events, and we require the 3D tracks to be 0 or 1 to the events, the dataset includes the electrons as well as photons. In Fig. 3.1 there is a bump at

$40 \leq E_T \leq 50$ GeV, which comes from the electrons from Drell-Yan process. Figure 3.2 shows the mass distribution of the EM pairs in the diphoton dataset, which clearly shows the peak from the contamination of the Drell-Yan process. Figure 3.3 shows the mass distribution of the EM pairs in the diphoton dataset, after the requirement of no 3D tracks pointing at the EM clusters is made. The peak from the contamination of the Drell-Yan process disappears in this plot.

3.3 Offline Event Selection

In the offline event selection, basically we use the same variables given from the algorithm used in the level 3 trigger. In the offline analysis we apply to the events some correction routines for the detectors which have been estimated from the data accumulated during the whole run.

3.3.1 Energy Correction and Transverse Energy Requirement

The transverse energy for electrons/photons in the CEM was corrected in three ways:

1. correction for response variations in the individual CEM tower,
2. correction for tower-to-tower gain variation,
3. correction for time dependent gain variation.

The correction factors for the difference of the response in each individual tower of the calorimeter are given from the CEM test beam results with electrons. Reference [27] describes the results from 50 GeV electron data.

The tower-to-tower gain correction is done with the CEM testbeam result. It is also corrected with the inclusive electron dataset [36][37].

The CEM uses the photomultiplier tubes as a readout device, which detect the photons from scintillating tiles via a wave-shifting bar and the light guide. The gain

for each phototube sometimes should be monitored as a function of the time during the collider run because of the fluctuations of their long-term stability. The long-term stability of the scintillating tiles, wave-shifting bars and the light guides is also taken into account for degradation of the energy resolution and the energy scale. It is monitored during the runs and then used in the correction routines at the off-line level if needed.

At the offline event selection, the events are required to have at least two EM clusters with the corrected E_T of

$$E_T^{corrected} \geq 12\,\mathrm{GeV}\,, \tag{3.4}$$

to reject the trigger bias for the E_T cut at the level 2 (where E_T is required to be larger than 10 GeV) .

3.3.2 Calorimeter Isolation Cut

A calorimeter isolation cut is one of the most effective criterion in the photon selection cuts. The dominant source of the backgrounds for this analysis is the neutral mesons decaying into multi photons with large transverse momentum which come from the quark/gluon fragmentation. Usually high p_T neutral mesons are the constituents of "jets", thus a larger amount of the underlying particles are associated with them, compared with the prompt photon case. The calorimeter isolation cut therefore effectively rejects the background neutral hadrons from prompt photons.

The calorimeter isolation is calculated as follows; first we make the cone around an EM cluster with a radius ΔR defined by

$$\Delta R = \sqrt{\Delta\eta^2 + \Delta\phi^2}. \tag{3.5}$$

The cone radius of 0.4 or 0.7 is typically used in CDF physics analyses. Then the energy depositions in all towers within the radius are added, and finally the energy of the EM

cluster itself is subtracted,

$$\text{Isolation} = \left(\sum_{i \leq \text{cone size}} E_i \right) - E_{cluster} \,. \tag{3.6}$$

where E_i is the tower energy and $E_{cluster}$ is the energy of an EM cluster.

Figure 3.4 shows the isolation distributions in the cone of 0.4 , where the diphoton events are selected with all the selection cuts described in this chapter except for the isolation cut, and are applied the background subtraction method which is described in the next chapter, to extract the real diphoton events and background events. In this figure the R shows the fraction of events within the isolation $\leq$ 1 GeV. Most of the diphoton events are within the isolation $\leq$ 1 GeV ($R \sim 0.90$), while the backgrounds are much broader than the signals ($R \sim 0.36$ for the total backgrounds). Thus we chose the isolation cut

$$\text{isolation in cone } 0.4 \leq 1\,\text{GeV} \tag{3.7}$$

to select the diphoton candidates.

3.3.3 Lateral Shower Profile: χ^2 and Extra Cluster Cut in the CES

The lateral shower profile in the CES is useful to discriminate background particles decaying into multi photons. For example, photons from $\pi^0 \to \gamma\gamma$ deposit their energy into CEM, with a minimum opening distance d (cm) at a radius R (cm) from the beam line. The minimum opening distance is related to the p_T of π^0 by

$$d\,(\text{cm}) \approx \frac{2RM_{\pi^0}}{p_T} \,, \tag{3.8}$$

where $M_{\pi^0} = 0.135\,\text{GeV}/c^2$ is the π^0 mass, P_T is in GeV/c, $R = 184\,\text{cm}$ at the CES radius. It indicates that for the π^0 mesons with high $p_T \geq 5\,\text{GeV}$ we have $d\,leq 10\,\text{cm}$ so that the decaying multiple photons are not separated each other enough to be dis-

tinguished with the CEM tower configuration. In other words they are included in the same CEM tower. The CES shower profile of such an event shows a the different shower shape compared with that from the testbeam electrons. We use this difference to reject the backgrounds effectively.

The CES provides us the information of the lateral profile of the EM shower and its lateral position at shower maximum region in the CEM. The CES clusters are found independently in both the wire and the strip view. First we look for the wire/strip channels which have an output of $\geq$ 0.5 GeV to be regarded as the seed channels. Then we include the 11 channels (with the threshold of 57.2 MeV) centered on the seed channel. We repeat this procedure for all seed channels. The CES cluster should be associated with the corresponding EM cluster.

The configuration of the CES is described in the previous chapter. In the CES coordinate, we regard the x and z position of the EM shower as the weighted mean of the cluster in each wire/strip view, which are labeled as X_{CES} and Z_{CES}, respectively. In order to use the CES clusters in its fiducial area, the CES cluster is required to satisfy the geometrical cuts

$$|X_{CES}| \leq 17.5\,\mathrm{cm}\,, \tag{3.9}$$

$$14\,\mathrm{cm} \leq |Z_{CES}| \leq 217\,\mathrm{cm}, \tag{3.10}$$

in the CES local coordinate.

Before referring to the evaluation of the CES χ^2, we note that the shower shape of the test beam electrons is used as a standard EM shower profile for this analysis instead of that from real photons. Ideally we should have the lateral shower profile for real photons as a standard shower profile. But we don't have the testbeam result for real photons, and using the real photon beam is not realistic at the testbeam. We have to rely on the lateral shower shape of the testbeam electrons. Essentially the difference between the shape for photons and that for electrons is small. Only the shower-starting point for electrons is slightly earlier than that for photons, according to shower simulations. We

include this difference into the systematic uncertainty in evaluating the diphoton cross section, which will be discussed in the next chapter. The CES χ^2 is calculated by:

$$\chi^2 = \frac{1}{4}\sum_{i=1}^{11}\frac{(y_i - \bar{y}_i)^2}{\sigma_i^2}\,, \tag{3.11}$$

where i is the channel index, y_i is the profile of either wire or strip channel from the collision data, and $\bar{y}_i$ is the standard electron profile, and σ_i^2 is the estimated variance of the standard profile $\bar{y}_i$. The $\bar{y}_i$ is from the test beam result. See Appendix B for more detailed description. Using Eq. 3.11, we calculated the CES χ^2 in both wire and strip view. We call them χ^2_{wire} and χ^2_{strip}, respectively.

A variable χ^2_{CES} is defined as the mean value of χ^2_{wire} and χ^2_{strip}:

$$\chi^2_{CES} = \frac{\chi^2_{wire} + \chi^2_{strip}}{2}\,. \tag{3.12}$$

Since the χ^2_{CES} for testbeam electrons is mostly within 20, it is effective to require

$$\chi^2_{CES} \leq 20\,, \tag{3.13}$$

for the background reduction.

The variable χ^2_{CES} is also used in the background subtraction which will be described in the next chapter, where we calculate the efficiencies for the photons/backgrounds to have $\chi^2_{CES} \leq 4$ in the sample $\chi^2_{CES} \leq 20$.

If a CEM cluster has two CES clusters and they are located close to each other, the EM cluster has a possibility of coming from background neutral mesons; one of the decaying multiple photons would make the first CES cluster and the rest of the photons come together to make the second CES cluster. Thus a CES extra cluster cut is effective to reject the background neutral mesons. The events are required that they do not have the extra CES cluster above 1 GeV near the seed tower in both wire and strip views.

3.3.4 No-Track Requirement

As is seen in Figs. 3.2 and 3.3, it is essential to require that there is no 3D tracks associated with the EM clusters.

When the E_T of the CEM cluster is greater than 35 GeV, we use the CPR hit rate to extract real diphoton events, instead of using the CES. The CPR is divided into only four chambers in the z-direction, which means we do not know which particle makes the CPR hit if two or more particles penetrate the same CPR module. We require that the events have no tracks pointing at the CPR cluster (see Chapter 2) if the CEM cluster have $E_T \geq 35$ GeV.

3.3.5 Z vertex and Rapidity Cut

At the event reconstruction level, we have information of the $\bar{\text{p}}$p collision point measured by the VTX along the beam line. Some criteria, such as the number of the VTX octant segments which are used to reconstruct the Z vertex, the number of hits in the VTX, and the ratio of the number of tracks in the forward region and the backward region, are applied to classify the vertices into 6 types. The best rank Z vertex requires that the number of the VTX octant segments are larger than 5, the number of the VTX hits are more than 180, and the ratio of the number of forward/backward reconstructed tracks are less than 0.7 . The second rank Z vertex requires the same criteria except for that the number of the VTX hits be in between 72 and 180 . In this analysis we require that at least one vertex should have the "best 2" rank and it should be within the area of

$$|Z_{vertex}| \leq 60\,\text{cm}\,, \tag{3.14}$$

to confirm the event occurring inside the fiducial region of the CDF detector.

Using Z vertex and the CES cluster position, the physics rapidity of a photon is

calculated by

$$\begin{aligned} \eta_\gamma &= \frac{1}{2}\log\left(\frac{E + p_Z}{E - p_Z}\right) \\ &= \frac{1}{2}\log\left(\frac{\sqrt{R_{CES}^2 + Z_{vertex}^2 + X_{CES}^2} + Z_{vertex}}{\sqrt{R_{CES}^2 + Z_{vertex}^2 + X_{CES}^2} - Z_{vertex}}\right) \end{aligned} \tag{3.15}$$

where R_{CES} is the radius of the CES cylinder, X_{CES} is the X position of the CES cluster in the CES coordinate and Z_{vertex} is the interaction point in the detector $R - Z$ view.

The rapidity η_γ is required to satisfy

$$|\eta_\gamma| \leq 0.9 \tag{3.16}$$

to compare the data with the NLO QCD prediction.

3.3.6 Final Diphoton Candidates

Table 3.2 shows a list of the selection cuts and the number of events in the 1993 - 1995 collider run. The diphoton dataset from 1992 - 1993 collider run is analyzed separately with the same offline selection cuts.

By combining the two collider runs, total of 652 events are obtained as the diphoton candidate events.

3.4 Efficiencies for the Trigger and Selection Cuts

3.4.1 Level 2 Trigger Efficiency

The dielectron sample split from the inclusive electron sample was used to evaluate the level 2 trigger efficiency. The standard electron selection criteria are described in

diphoton trigger dataset	71206
photon selection criteria	events alive
no associated 3D track	22844
$E_T \geq 12\,\mathrm{GeV}$	13228
extra transverse energy in cone $0.4 \leq 1\,\mathrm{GeV}$	1452
$\lvert X_{CES}\rvert$ and $\lvert Z_{CES}\rvert$ fiducial cuts	1299
no extra strip / wire cluster	784
no associated CPR track	779
$\chi^2_{CES} \leq 20$	776
$\lvert Z_{vertex}\rvert \leq 60\,\mathrm{cm}$	713
$\lvert\eta_\gamma\rvert \leq 0.9$	570
result from 1993-1995 collider run	570
result from 1992-1993 collider run	82
total number of diphoton candidate	652

Table 3.2: Event cuts and the number of diphoton candidate events.

detail in Appendix A. The following criteria were applied:

1. Both EM clusters in the central region with $E_T \geq 5\,\mathrm{GeV}$,
2. Extra energy in cone $0.4 \leq 1\,\mathrm{GeV}$,
3. Standard photon fiducial cuts ,
4. $\lvert Z_{vertex}\rvert \leq 60\,\mathrm{cm}$,
5. Number of 3D tracks $= 1$,
6. $\chi^2_{CES} \leq 20$,
7. $E/P \leq 1.5$,
8. $Had/EM \leq 0.05$,
9. $L_{sh} \leq 0.2$,
10. $\lvert\eta_e\rvert \leq 0.9$,

11. Position difference between the CTC track extrapolated to the CES and the CES cluster position; $|\Delta x| \leq 1.5$ cm and $|\Delta z| \leq 2.5$ cm.

The level 2 dielectron trigger was required to the events to ensure that the events passed the dielectron trigger and to avoid the effect of prescale factors from other triggers.

Figure 3.5 shows the efficiency that the dielectron events pass the diphoton level 2 trigger as a function of E_T of the next leading electron, where the next leading electron means the electron with the second-highest E_T. It becomes flat in the region of $E_T \geq 12\,\mathrm{GeV}$.

We calculate the mean value of the data points above 12 GeV, and obtain

$$\epsilon_{L2} = 0.84 \pm 0.02\,. \tag{3.17}$$

This was used to correct the diphoton cross section for the inefficiency of the level 2 trigger.

3.4.2 Calorimeter Isolation Cut Efficiency

The calorimeter isolation cut efficiency is evaluated by the minimum bias (MB) dataset. First of all, we generate two sets of the random numbers for rapidity and azimuthal angle, $(\eta_1\,\phi_1)$, $(\eta_2\,\phi_2)$, in each MB event. We assume as if there are diphotons placed at these points. Then we calculate the calorimeter isolation using Eq. 3.6 around these points. Figure 3.6 shows a comparison of the cone 0.4 isolation distribution of the diphoton events with that from the MB events. Since the two distributions are consistent with each other, we can estimate the isolation cut efficiency with the MB events instead of the diphoton events.

Figure 3.7 shows the efficiency of the isolation cut (extra transverse energy in cone 0.4 $\leq$1 GeV), as a function of the instantaneous luminosity. The efficiencies are fit by a straight line. A typical number of the efficiency is 0.895 ± 0.005 per photon at $9.1 \times 10^{30}\,\mathrm{cm}^{-2}\,\mathrm{sec}^{-1}$.

3.4.3 CES Extra Cluster Cut Efficiency

Most of the CEM clusters for real photons are expected not to have extra CES clusters, but CEM clusters with high E_T would have the possibility to have them because they have large electromagnetic energy depositions at the shower maximum position, which would more often create an extra cluster by shower fluctuation.

The CES extra cluster cut efficiency is estimated using the testbeam electron data. Figure 3.8 shows the efficiency as a function of the electron energy. The efficiency goes lower as the energy of the electron goes higher, as is expected from the above qualitative argument. The efficiency for the electrons from W decay is also shown in the figure. It is slightly lower than the interpolation of the testbeam electron data points due to the radiation of an extra photon.

3.4.4 Track Cut Efficiency

The requirement of no-tracks pointing at the CEM cluster rejects real photon events in two cases; one is the photon conversion in front of the tracking chamber, where a real photon is converted into an electron-positron pair.

This inefficiency of the 3D track cut due to the photon conversion depends on the amount of the materials in front of the CTC. The inefficiency was calculated in the inclusive photon cross section measurement at CDF [13][38]. The inefficiency that we loose real photons due to photon conversion in the 3D track cut was 0.06 per photon with a 0.4% uncertainty.

The track cut also rejects the events in the case where the CEM cluster comes from a real photon but the tracks from underlying events accidentally point at the cluster..

This inefficiency that we loose the real photons due to underlying tracks in the 3D track cut was estimated with the minimum bias events. Virtual CEM clusters are randomly generated in the minimum bias events, and the tracks which point at the virtual clusters are looked for. The inefficiency was calculated to be 0.06 per photon with a 1% uncertainty.

3.4.5 Z Vertex Cut Efficiency

The efficiency for the Z vertex cut was calculated using the Z_{vertex} distribution of the good runs which were taken from the CDF muon triggers [40]. It was 0.96±0.01 .

3.4.6 Fiducial Cut Efficiency

The efficiency for the CES fiducial volume cut (see Eq. 3.9 and 3.10) is 0.663 per photon.

3.4.7 Summary of Efficiencies

Table 3.3 gives a summary of the efficiencies. They are used in Chapter 5 in the calculation of the diphoton cross section.

ITEM	VALUE
CES fiducial cuts $\epsilon_{\rm fid}$ (per photon)	0.663
conversion veto $\epsilon_{\rm conv}$ (per photon)	0.94
underlying track $\epsilon_{\rm trk}$ (per photon)	0.94
isolation cut $\epsilon_{\rm iso}$ (per photon)	0.9 luminosity dependent
Zvertex cut $\epsilon_{\rm zvret}$ (per event)	0.96
extra CES cluster cut $\epsilon_{\rm ext}$ (per photon)	>0.9 E_T dependent
trigger efficiency $\epsilon_{\rm L2}$ (per event)	0.84

Table 3.3: Summary of the efficiencies.

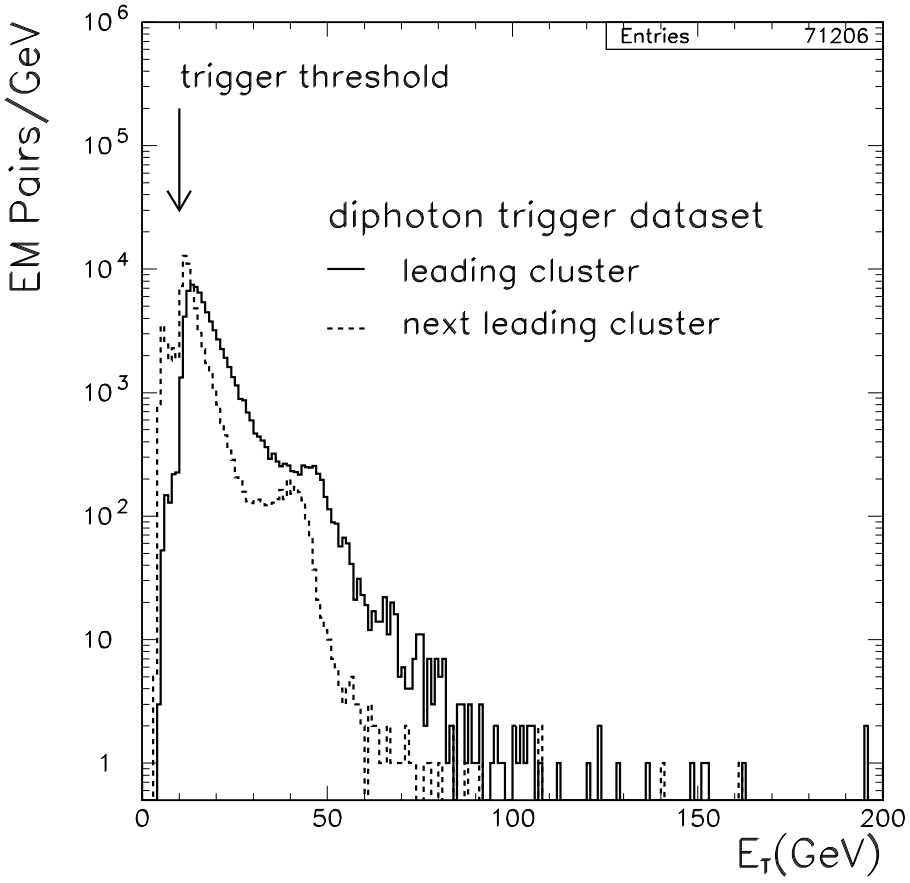

Figure 3.1: E_T distribution of the leading and next leading EM clusters of the EM pairs in the diphoton dataset.

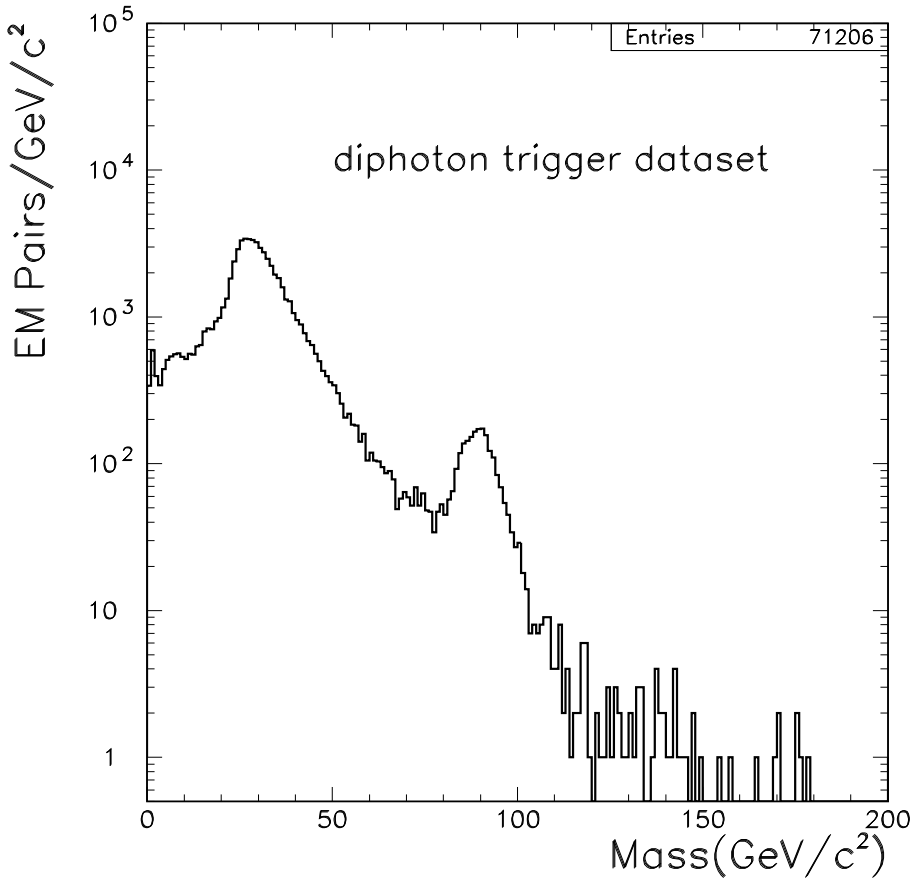

Figure 3.2: Invariant mass distribution of the EM pairs in the diphoton dataset.

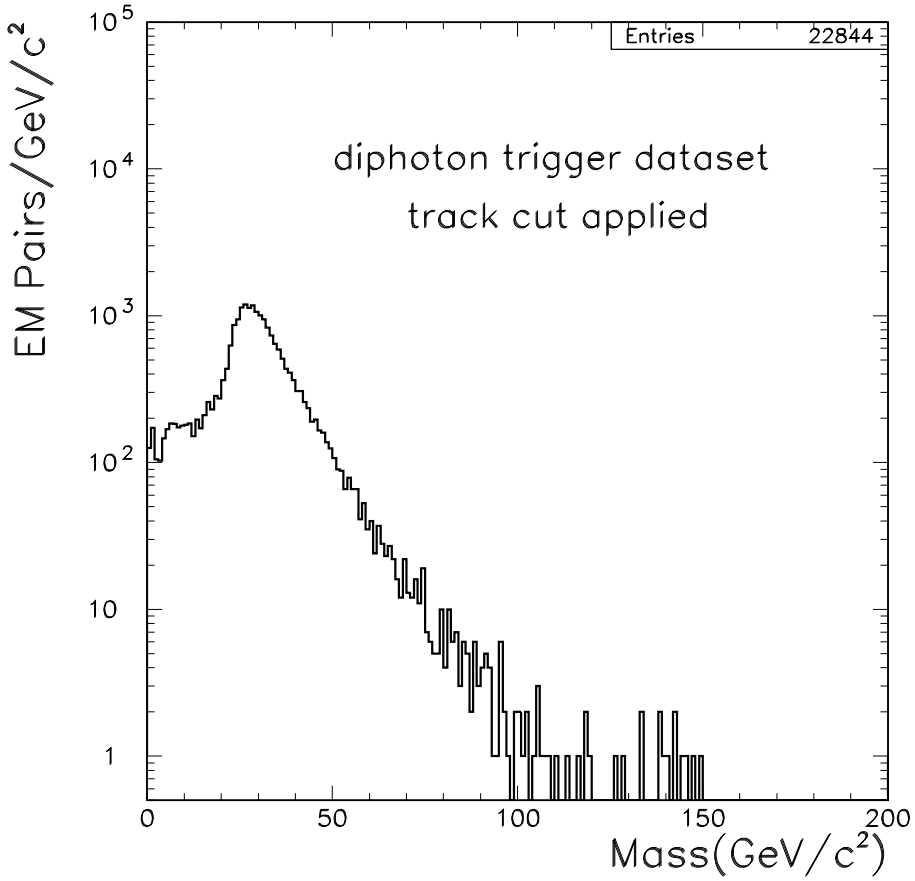

Figure 3.3: Invariant mass distribution of the EM pairs in the diphoton dataset, after the requirement for the number of 3D tracks to be zero is made.

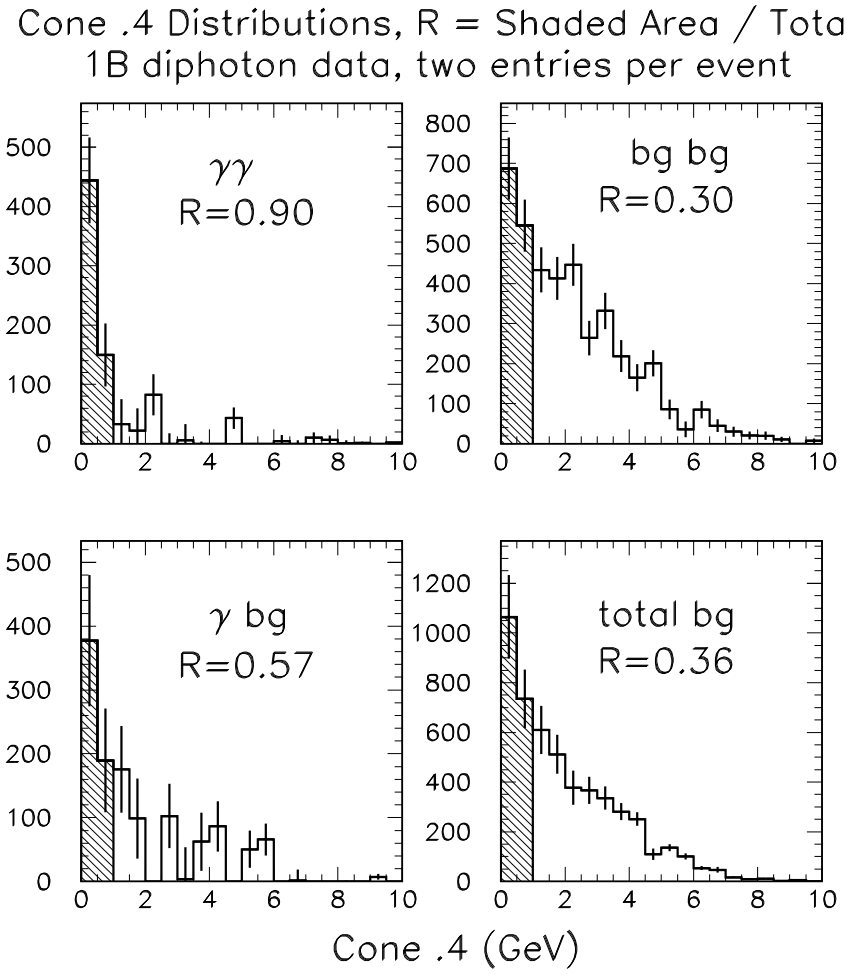

Figure 3.4: Distributions of the transverse energy isolation in the cone of 0.4 for (a) $\gamma\gamma$ events, (b) γ-background events, (c) background-background events and (d) total backgrounds (b+c). The R shows the ratio of the number of events in the shaded area to the number of the total events.

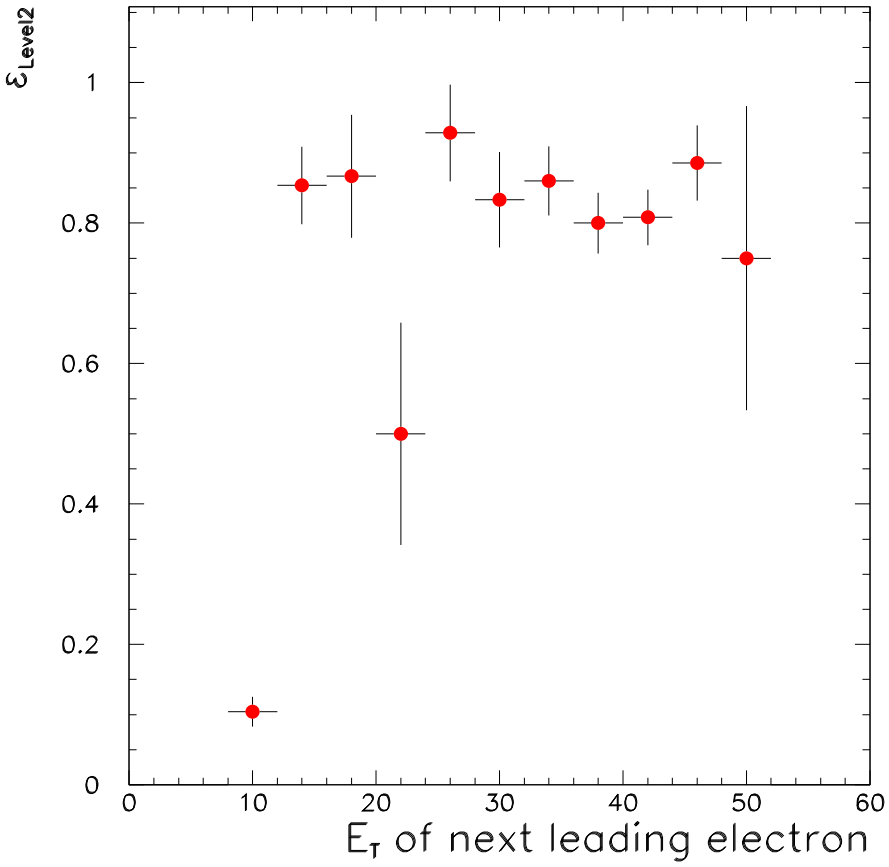

Figure 3.5: Level 2 trigger efficiency as a function of E_T for the next-leading electrons in the dielectron events.

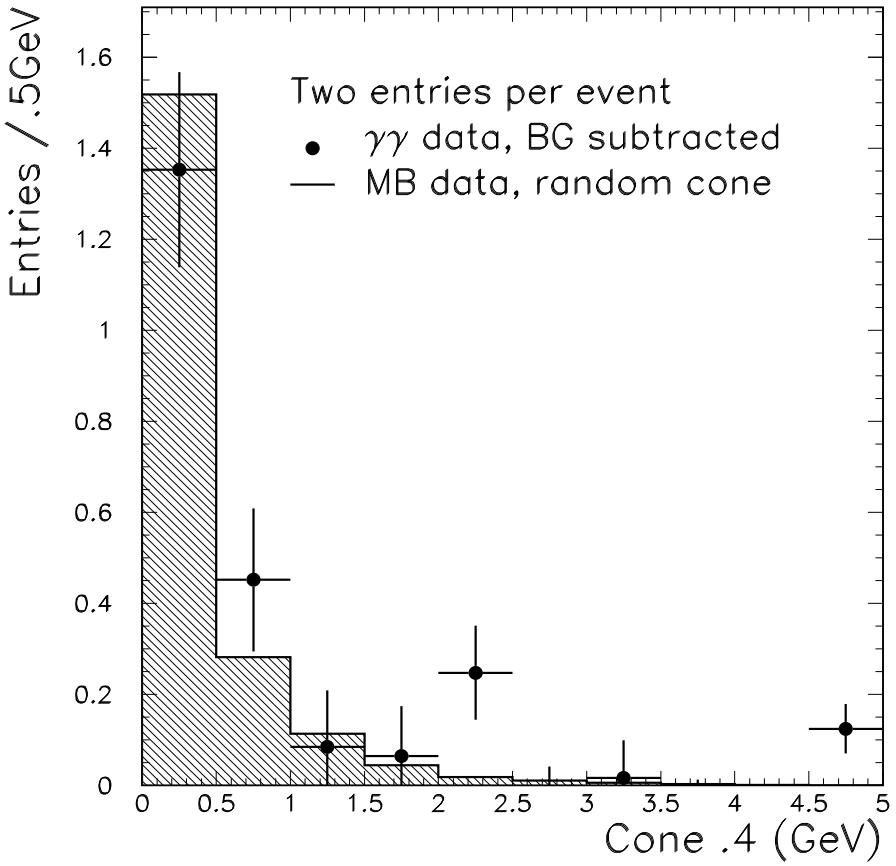

Figure 3.6: Comparison of the cone 0.4 isolation distributions between the diphoton events (points) and MB events (histogram). Two entries per event for both points and histogram.

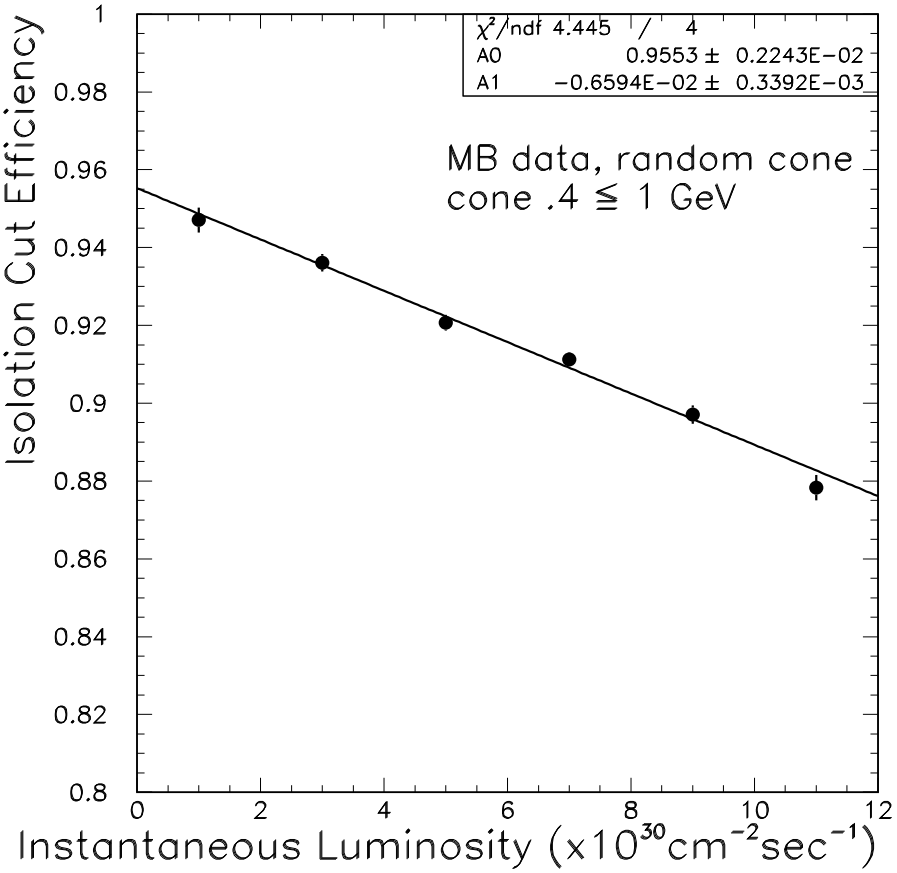

Figure 3.7: Efficiency of the isolation cut (extra transverse energy in the cone $0.4 \leq 1$ GeV) as a function of the instantaneous luminosity.

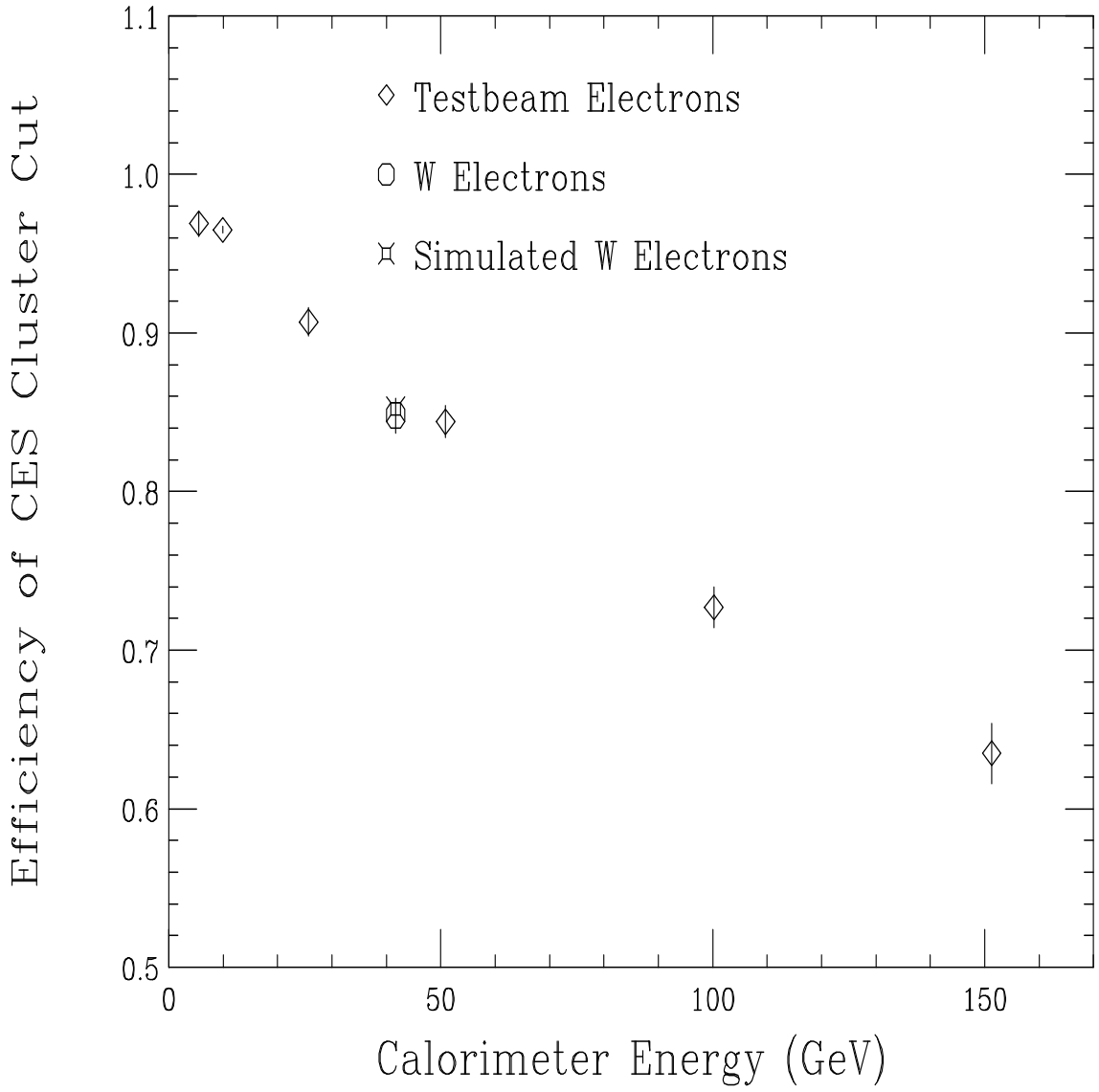

Figure 3.8: Efficiency of the CES extra cluster cut as a function of the calorimeter energy.

Chapter 4

Photon Identification

In this chapter we describe the photon identification procedure and the background subtraction in the diphoton sample selected in the previous chapter.

4.1 Background Sources

In the previous chapter we described the selection criteria for the diphoton candidates. After the selection cuts, we have the candidates for diphoton events, but we still have backgrounds in the candidates, which we are unable to reject by the selection cuts on event-by-event basis, because multiple photons from the neutral mesons cannot be identified on event-by-event basis by the CES nor by the CPR.

Table 4.1 shows a list of the neutral mesons which are considered as background sources in this analysis and their world average branching ratios of their decays to photons or π^0's [41].

4.2 Photon Identification Method

4.2.1 Profile and Conversion Methods

The CES provides us a statistical method to distinguish between a real photon and multiple photons from neutral mesons. The comparison of the lateral shower profile in the shower maximum region with that from the electron testbeam result gives us a statistical difference between a real photon and multiple photons from neutral mesons. We express the difference with a variable χ^2_{CES} defined by Eq. 3.12.

If the background particle has relatively low $P_T\,(\leq 40\,\mathrm{GeV})$, the shower shape is degraded by the multiple photons having the minimum distance calculated by Eq. 3.8, which makes the CES χ^2 higher. While at higher $P_T\,(\geq 40\,\mathrm{GeV})$, the distance between the photons becomes smaller enough to make the CES χ^2 lower. As a result, at high p_T it is more difficult with this method to distinguish background events from real photon events.

Another statistical information is the difference of the hit rates in the CPR between photons and background mesons. The CPR hit rates for them differ because the conversion probabilities in front of the calorimeter differ. At high p_T, multiple photons from the neutral meson decays are almost in the same direction, and they come into the same module of the CPR. The hit rate in the CPR is correlated with the number of photons coming into the module.

The difference of the conversion probabilities between photons and π^0's is demonstrated as follows. Consider the π^0 decay $\pi^0 \rightarrow \gamma\gamma$ as a background, for example. The

Decay modes	Branching ratio (%)
$\pi^0 \rightarrow \gamma\gamma$	98.798 ± 0.032
$\eta \rightarrow \gamma\gamma$	39.25 ± 0.31
$\eta \rightarrow \pi^0\pi^0\pi^0$	32.1 ± 0.4
$K^0_s \rightarrow \pi^0\pi^0$	31.39 ± 0.28

Table 4.1: List of the neutral background sources.

conversion probability for the π^0 (P_π) and that for single photon (P_γ) is related by:

$$\begin{aligned} P_\pi &\approx P_\gamma^2 + 2P_\gamma(1 - P_\gamma) \\ &= 1 - (1 - P_\gamma)^2 \end{aligned} \tag{4.1}$$

where we have assumed that the conversion probability is approximately independent of p_T. Using the difference of the conversion probability between single photons and π^0's, we extract the real diphoton events from the diphoton candidates statistically.

The CES Profile Method Efficiencies

The signal and background efficiencies for the CES profile method are defined by

$$\epsilon_\gamma = \frac{N_{\chi^2_{CES}<4,\gamma}}{N_{\chi^2_{CES}<20,\gamma}}, \tag{4.2}$$

$$\epsilon_b = \frac{N_{\chi^2_{CES}<4,b}}{N_{\chi^2_{CES}<20,b}}, \tag{4.3}$$

where $N_{\chi^2_{CES}<20,\gamma}$ ($N_{\chi^2_{CES}<20,b}$) is the number of photons (backgrounds) in a given photon (background) sample with $\chi^2_{CES} < 20$, $N_{\chi^2_{CES}<4,\gamma}$ ($N_{\chi^2_{CES}<4,b}$) is the number of photons (backgrounds) with $\chi^2_{CES} < 4$ in the sample.

The CPR Conversion Method Efficiencies

The signal and background efficiencies for the CPR conversion method are defined by

$$\epsilon_\gamma = \frac{N_{CPRhit,\gamma}}{N_\gamma}, \tag{4.4}$$

$$\epsilon_b = \frac{N_{CPRhit,b}}{N_b}, \tag{4.5}$$

where N_γ (N_b) is the number of photons (backgrounds) in a given photon (background) sample, $N_{CPRhit,\gamma}$ ($N_{CPRhit,b}$) is the number of photons (backgrounds) with a hit at the

corresponding CPR position in the sample. We define the CPR hit as the total charge of the CPR cluster greater than 500 fC.

4.2.2 Calculation of the Number of Real Diphoton Events in the Diphoton Candidates

Once we have the efficiencies, we can calculate the real number of photon events and background events. In the CES method, we test the events whether the events have the EM cluster which has $\chi^2_{CES} \leq 4$ or not. We use a word "pass" when the EM cluster has the $\chi^2_{CES} \leq 4$. Also in the CPR method, we test the events whether the events have the EM cluster which makes a hit in the CPR or not. We use a word "pass" when the EM cluster makes a hit in the CPR.

In the single photon case, the following vector equation can be used to obtain the numbers of true photons and backgrounds:

$$\begin{pmatrix} N_{false} \\ N_{pass} \end{pmatrix} = \begin{pmatrix} 1 - \epsilon_b & 1 - \epsilon_\gamma \\ \epsilon_b & \epsilon_\gamma \end{pmatrix} \begin{pmatrix} N_b \\ N_\gamma \end{pmatrix} \tag{4.6}$$

where N_{false} (N_{pass}) is the number of candidates that "fail" ("pass") the test described above, N_γ (N_b) is the number of true photons (backgrounds) in the photon candidates. In the diphoton case, there are 4 possible combinations in the CES/CPR test, which are false-false, false-pass, pass-false and pass-pass, and the number of possible cases for the combinations of signal and background become 4, which are $b-b$, $b-\gamma$, $\gamma-b$ and $\gamma-\gamma$. We have the following vector equation with 4×4 matrix, instead of 2×2 in the single photon case.

$$\begin{pmatrix} N_{ff} \\ N_{fp} \\ N_{pf} \\ N_{pp} \end{pmatrix} = \begin{pmatrix} (1-\epsilon_{b1})(1-\epsilon_{b2}) & (1-\epsilon_{b1})(1-\epsilon_{\gamma 2}) & (1-\epsilon_{\gamma 1})(1-\epsilon_{b2}) & (1-\epsilon_{\gamma 1})(1-\epsilon_{\gamma 2}) \\ (1-\epsilon_{b1})\,\epsilon_{b2} & (1-\epsilon_{b1})\,\epsilon_{\gamma 2} & (1-\epsilon_{\gamma 1})\,\epsilon_{b2} & (1-\epsilon_{\gamma 1})\,\epsilon_{\gamma 2} \\ \epsilon_{b1}\,(1-\epsilon_{b2}) & \epsilon_{b1}\,(1-\epsilon_{\gamma 2}) & \epsilon_{\gamma 1}\,(1-\epsilon_{b2}) & \epsilon_{\gamma 1}\,(1-\epsilon_{\gamma 2}) \\ \epsilon_{b1}\,\epsilon_{b2} & \epsilon_{b1}\,\epsilon_{\gamma 2} & \epsilon_{\gamma 1}\,\epsilon_{b2} & \epsilon_{\gamma 1}\,\epsilon_{\gamma 2} \end{pmatrix} \times \begin{pmatrix} N_{bb} \\ N_{b\gamma} \\ N_{\gamma b} \\ N_{\gamma\gamma} \end{pmatrix} \tag{4.7}$$

where N_{ff} is the number of diphoton candidates in which both the EM cluster fail the test, N_{fp} is the number of diphoton candidate in which the first EM cluster fails the test and the second EM cluster passes the test, ϵ_{b1} is the background efficiency for the first EM cluster, $\epsilon_{\gamma 1}$ is the photon efficiency for the first EM cluster, and so on.

By inverting this 4×4 matrix, the real number of signals $(N_{\gamma\gamma})$ and backgrounds ($N_{b\gamma}$, $N_{\gamma b}$ and N_{bb}) are evaluated.

Inverting the Matrix on Event-by-Event Basis

As is seen in the next section, the CES profile efficiencies have a large dependence on photon p_T. The CPR conversion efficiencies also have a dependence on the amount of materials in front of the CPR. Thus the profile and conversion efficiencies $(\epsilon_{\gamma 1}, \epsilon_{\gamma 2}, \epsilon_{b1}, \epsilon_{b2})$ vary event by event. It is then natural to invert the matrix on event-by-event basis, taking these dependences into account.

For example, consider that we have a diphoton candidate in which both of EM clusters pass the $\chi^2 < 4$ test. Then we have an input 4-dimensional vector (n_{ff} , n_{fp} , n_{pf} , n_{pp})= (0, 0, 0, 1) in Eq. (4.7). By inverting the 4×4 matrix given by the CES / CPR efficiencies, we will have an output 4-dimensional vector (w_{bb} , $w_{b\gamma}$, $w_{\gamma b}$, $w_{\gamma\gamma}$), the four elements of which represent weights for this particular event to be $b-b$,

$b-\gamma$, $\gamma-b$ and $\gamma-\gamma$.

The procedure is applied to all diphoton candidates. That is, we invert the 4×4 matrix on event-by-event basis to get the weights. The total number of the signal and the background events are calculated by taking the sum of these signal/background weights:

$$N_{\gamma\gamma} = \sum_{i=1}^{n} w_{\gamma\gamma}^{(i)}\,, \tag{4.8}$$

$$N_{\gamma b} = \sum_{i=1}^{n} w_{\gamma b}^{(i)}\,, \tag{4.9}$$

$$N_{b\gamma} = \sum_{i=1}^{n} w_{b\gamma}^{(i)}\,, \tag{4.10}$$

$$N_{bb} = \sum_{i=1}^{n} w_{bb}^{(i)}\,, \tag{4.11}$$

where n is the number of total diphoton candidates. The statistical errors for the $\gamma\gamma$, γb, $b\gamma$ and bb events are given by

$$\sigma_{\gamma\gamma} = \sqrt{\sum_{i=1}^{n} w_{\gamma\gamma}^{(i)\,2}}\,, \tag{4.12}$$

$$\sigma_{\gamma b} = \sqrt{\sum_{i=1}^{n} w_{\gamma b}^{(i)\,2}}\,, \tag{4.13}$$

$$\sigma_{b\gamma} = \sqrt{\sum_{i=1}^{n} w_{b\gamma}^{(i)\,2}}\,, \tag{4.14}$$

$$\sigma_{bb} = \sqrt{\sum_{i=1}^{n} w_{bb}^{(i)\,2}}\,. \tag{4.15}$$

4.3 Signal Efficiency for CES Profile Method

The CES signal efficiency ϵ_γ (Eq. 4.2) is evaluated by simulating photons by the PYTHIA event generator [42] and the QFL detector simulator [43]. The QFL simu-

Cuts
CEM cluster with $E_T \geq 25$GeV
Missing E_T $\leq$0.1
CEM fiducial volume
$\lvert Z_{vertex} \rvert \leq 60$ cm
Had/EM $\leq$0.1
E/p $\leq$1.5
L_{shr} $\leq$0.2
Position difference between the CTC track and the CEM cluster; $\lvert \Delta x \rvert \leq 1.5$ cm, $\lvert \Delta z \rvert \leq 3$ cm

Table 4.2: Selection criteria used to make the $W \rightarrow e\nu$ sample.

lation of the shower was based on the CDF testbeam results. The simulated CES χ^2 distribution was checked by the electrons from $W \rightarrow e\nu$ data. The simulated CES χ^2 distribution was also checked by photons from $\eta \rightarrow \gamma\gamma$ data.

4.3.1 Check on the Simulated χ^2_{CES} Distribution with Electrons from $W \rightarrow e\nu$

The $W \rightarrow e\nu$ sample was collected by the CDF 12 GeV electron trigger. Table 4.2 shows the selection criteria for the data.

We simulated $W \rightarrow e\nu$ electrons with the QFL simulation. In the QFL, the CES shower profile was based on the result of the CEM electron testbeam.

Figure 4.1 shows the comparison of the χ^2 distributions between the real W electrons and the simulated electrons in both the strip and the wire view. The simulation reproduced the data well.

4.3.2 Check on the CES signal efficiency with η Sample

η Sample

The simulated photon χ^2 distribution was checked by using the well separated real diphotons from η mesons decaying to diphotons (with the branching ratio of 39%) in the CDF data. In order to select the $\eta \rightarrow \gamma\gamma$ events with the CDF photon trigger, we searched for the events having an isolated EM cluster which contains two CES strip clusters located at two separate EM towers in the EM cluster. Each EM tower provides a corresponding single photon's energy, and the two CES clusters provide each photon's position. Then we are able to measure the η mass.

We selected the η sample with the selection criteria shown in Table 4.3. The events were taken by the 10 GeV trigger ("Trigger Cuts" in this table) . They were required to satisfy the "photon analysis cuts" described in this table. The missing E_T significance in the "photon analysis cuts" is defined by

$$S = \frac{E_T}{\sqrt{\sum E_T}} \tag{4.16}$$

where E_T is the transverse energy of the EM cluster, $\sum E_T$ is the sum of the E_T for all calorimeter clusters. The missing E_T significance cut rejects the backgrounds from cosmic ray muons emitting a bremsstrahlung photon. Finally the events were required to satisfy the "Two-Photon Cuts" in the table, where the EM clusters in the data were required to have two CES strip clusters located in two separate EM towers. The number of CES wire clusters in the EM cluster is required to be at least 1, because it was likely that the two strip clusters would overlap in the wire view.

Simulated η sample

Using the QFL, we generated η mesons decaying to diphotons with a p_T spectrum

$$\frac{dN}{dp_T} \sim \frac{1}{p_T^{5.5}}. \tag{4.17}$$

Trigger Cuts
$E_T \geq 10\,\mathrm{GeV}$
$Had/EM \leq 0.125$
ratio of extra energy in cone 0.7 and cluster energy ≤ 0.15
Photon Analysis Cuts
ratio of extra transverse energy in cone 0.7 and cluster $E_T \leq 0.15$
No 3D tracks pointing at the cluster
pseudorapidity $\lvert\eta\rvert \leq 0.9$
$\lvert Z_{vertex}\rvert \leq 50\,cm$
Missing E_T significance≤ 3 (see text)
Two-Photon Analysis Cuts
$9 \leq E_T \leq 15\,\mathrm{GeV}$
2 CES strip clusters in EM cluster
Each CES strip cluster in separate tower
1 or 2 CES wire clusters in EM cluster
$14 \leq \lvert Z_{CES}\rvert \leq 217\,\mathrm{cm}$ for both CES strip clusters
$\lvert X_{CES}\rvert \leq 20\,\mathrm{cm}$ for the CES wire cluster(s)
$\lvert X_{CES}\rvert \leq 17.5\,\mathrm{cm}$ for at least one of the CES wire cluster

Table 4.3: Selection criteria used to make the η sample.

Table 4.4 shows the conditions of the QFL for the η meson sample. The simulated events were required to satisfy the same selection criteria which were required to the data, as shown in Table 4.3.

Result

Figure 4.2 shows the invariant mass distribution of the diphotons in the η sample. The solid line is a fit to two Gaussians. The peak of π^0's is not clear in this plot because the 11 channel clustering in the CES is too wide to observe the π^0 peak.

We made the CES χ^2 distribution in the strip view for real photons from η decays by looking at the strip view χ^2 distribution of the events in the peak region defined as $0.45 < M < 0.625\,\mathrm{GeV/c^2}$ (signals plus backgrounds), and that of the events from two sidebands defined as $0.225 < M < 0.425\,\mathrm{GeV/c^2}$ and $0.650 < M < 0.850\,\mathrm{GeV/c^2}$ (backgrounds). By subtracting the strip view χ^2 distribution for the backgrounds in the two sidebands from that for the signals plus backgrounds in the peak region, we obtained the strip view χ^2 distribution for photons from η decays, as shown in Fig. 4.3. The strip view χ^2 distribution from photons from simulated η's is superimposed on it. The simulated distribution agreed with that from the data. The CES signal efficiency from the strip view χ^2 distribution from the simulation (data) was calculated to be $0.812 \pm 0.031 (0.810 \pm 0.006)$. The simulation reproduced the data well.

p_T range	$8\,\mathrm{GeV} \leq p_T \leq 17\,\mathrm{GeV}$
azimuthal angle distribution	flat
η distribution	flat
Z vertex distribution	gaussian, with $\sigma = 31$ cm

Table 4.4: Conditions of the QFL for making the η meson sample.

4.4 Background Efficiency for CES Profile Method

The CES efficiency for backgrounds ϵ_b (Eq. 4.3) was evaluated by generating π^0's, η's and K^0_S's with the PYTHIA event generator and simulating their showers with the QFL detector simulation. The relative number of π^0's, η's and K^0_S's produced in the $\bar{\mathrm{p}}\mathrm{p}$ collisions was determined using the CDF data. The simulated CES χ^2 distribution for π^0's was checked with the π^0's from $\rho^{\pm} \to \pi^0\pi^{\pm}$ decays.

4.4.1 Production Ratios η/π^0 and K^0_S/π^0

The measured numbers of π^0 and η mesons decaying to diphotons are written as

$$N^{detect}_{\pi^0} = N^{prod}_{\pi^0}\,\mathrm{BR}(\pi^0 \to \gamma\gamma)\,\epsilon(\pi^0 \to \gamma\gamma)\,, \tag{4.18}$$

$$N^{detect}_{\eta} = N^{prod}_{\eta}\,\mathrm{BR}(\eta \to \gamma\gamma)\,\epsilon(\eta \to \gamma\gamma)\,, \tag{4.19}$$

where $N^{detect}_{\pi^0}$ (N^{detect}_{η}) is the number of π^0 (η) $\to \gamma\gamma$ decays detected by the CDF detector, $N^{prod}_{\pi^0}$ (N^{prod}_{η}) is the number of π^0 (η) mesons produced in this collider run, $\mathrm{BR}(\pi^0 \to \gamma\gamma)$ ($\mathrm{BR}(\eta \to \gamma\gamma)$) is the branching ratio for the π^0 (η) to decay into diphotons, and $\epsilon(\pi^0 \to \gamma\gamma)$ ($\epsilon(\eta \to \gamma\gamma)$) is the detection efficiencies that the particles pass the photon selection criteria (see Table 3.2). The branching ratios are known from other experiments (see Table 4.1), the detection efficiencies for the backgrounds are obtained by the QFL simulation, so the only unknown parameters are $N^{prod}_{\pi^0}$ and N^{prod}_{η}.

Figure 4.4 shows the detection efficiency times the branching ratio for the $\pi^0 \to \gamma\gamma$, $\eta \to \gamma\gamma$, $\eta \to 3\pi^0$, and $K^0_S \to 2\pi^0$ decays. It shows that the π^0 is the dominant component in the neutral background.

η and π^0 Sample

In order to identify η and π^0 mesons in the CDF data, we used almost the same criteria as used in Section 4.3.2 (Table 4.3). We used 3 CES channels to make the CES

cluster instead of 11 channels, because, as shown in Fig. 4.2, the π^0 peak was not clear when we used 11 channel CES clustering. The number of the CES strip clusters in an EM cluster was required to be 2 or more, instead of exactly 2, and the two leading CES clusters were required to satisfy the rest of the CES criteria in Table 4.3.

Then we added more selection criteria. One was the energy isolation in the CES defined by

$$I_S = \frac{\sum_{i=3}^{n} E_{Si}}{E_{S1} + E_{S2}} \tag{4.20}$$

where n is the number of the CES strip clusters, E_{Si} is the strip energy of the ith strip cluster (energy ordered). Similarly we defined the CES wire cluster isolation, I_W. We required the events to satisfy these CES isolation variables to be less than 0.3.

Another criterion was the energy asymmetry defined by

$$Asymmetry = \frac{|E_1 - E_2|}{E_1 + E_2} \tag{4.21}$$

where E_1 and E_2 are the energy of the EM towers corresponding to each CES cluster. We required the events to have this asymmetry to be less than 0.8 to reduce the contamination of the single photons due to the shower fluctuation [44].

Calculation of η/π^0 Ratio

Figure 4.5 shows the invariant mass distribution of the diphotons with the 3 channel CES clustering. The solid line is a fit to two Gaussians plus polynomial, the dashed line is the background shape as a result of this fit, and the dotted line is the sum of the contamination of the single photons plus backgrounds. The contamination of the single photons due to the shower fluctuation was estimated with the simulated single photons with the same conditions used in Section 4.3.2 (Table 4.4).

The production ratio η/π^0 was calculated as follows. We define the peak region as $0.475 < M_{\gamma\gamma} < 0.625\,\mathrm{GeV}/c^2$ for the η, and $0.075 < M_{\gamma\gamma} < 0.225\,\mathrm{GeV}/c^2$ for the π^0.

The production ratio η/π^0 is obtained by

$$\eta/\pi^0 = \frac{(N_\eta - B_\eta)/A_\eta}{(N_{\pi^0} - B_{\pi^0})/(A_{\pi^0} + \frac{\gamma}{\pi^0}A_\gamma)} \tag{4.22}$$

where N_η (N_{π^0}) is the number of events in the η (π^0) peak region (signals plus backgrounds,), B_η (B_{π^0}) is the number of backgrounds in the η (π^0) peak region, A_η is the acceptance of the η's in the η mass region, A_{π^0} and A_γ are the acceptance of the π^0's and background single photons in the π^0 peak region, respectively, $\frac{\gamma}{\pi^0}$ is the ratio of misidentified single photons to π^0's in the π^0 peak region. N_η and N_{π^0} are obtained from the data points in Fig. 4.5, B_η and B_{π^0} were obtained from the result of the background fit, A_η, A_{π^0} and A_γ were calculated by QFL simulations [44]. The ratio $\frac{\gamma}{\pi^0}$ was calculated by both the data and the QFL [44].

Using Eq. 4.22, the production ratio of η's and π^0's was calculated to be

$$\eta/\pi^0 = 1.02 \pm 0.15(\text{stat.}) \pm 0.23(\text{syst.}). \tag{4.23}$$

Production Ratio K_s^0/π^0

The process $K_s^0 \to \pi^0\pi^0$ slightly contributes to the background χ^2 distributions. In evaluating the background efficiency determined by the QFL, we use the production ratio K_S^0/π^0 by the previous CDF experiment.

The production of K_S^0 has been measured by the CDF during the 1987 collider run, using charged decay modes [47]. A value of K_s^0/π^0 of 0.4 was used in the simulation, based on this measurement.

4.4.2 Check on the CES Background Efficiency with π^0's from $\rho^\pm \to \pi^\pm\pi^0$ Decay

The simulated CES background efficiencies was checked with the π^0's from $\rho^\pm \to \pi^0\pi^\pm$ decays in the CDF data.

$\rho^{\pm}$ sample

The $\rho^{\pm}$ mesons were identified starting from the π^0 sample described above. We required the following criteria for the tracks in the π^0 sample:

1. the charged track was required to have $p_T \geq 1.1\,\mathrm{GeV/c}$
2. $cos\,\theta^* \leq -0.88$, where $cos\,\theta^*$ is the angle between the $\pi^{\pm}$ direction in the $\pi^{\pm}\pi^0$ CMS frame and the $\pi^{\pm}\pi^0$ direction in the lab frame.

The $cos\,\theta^*$ cut was imposed to collect the asymmetric ρ decays with energetic π^0s.

We took all combinations of the π^0 and the charged tracks which passed the above criteria, and made the invariant mass distribution of π^0 plus a charged track, as shown in Fig. 4.6. The solid line is a fit to the Breit-Wigner form plus a linear function, the dashed line is the fitted linear function, showing the background shape. We evaluated the χ^2_{CES} distribution by looking at the χ^2_{CES} distribution with the events in the peak region (signals plus backgrounds) and that from the sidebands (background). The effect of the backgrounds in the peak region was then subtracted with the χ^2_{CES} distributions from sideband events. Figure 4.7 shows the χ^2_{CES} distribution of the π^0's from $\rho^{\pm}$ decay, together with the simulation. The simulation was in good agreement with the data.

4.4.3 Final CES Efficiencies

The final plot of CES $\chi^2_{CES} \leq 4$ cut efficiencies for both photons and backgrounds evaluated by the QFL simulation is shown in Fig. 4.8. The dotted lines show the bounds of the total systematic uncertainties described in the next section.

4.5 Sources of the Systematic Uncertainties for CES Efficiencies

The systematic uncertainties in the signal and the background CES efficiencies are highly correlated, because these efficiencies are both sensitive to the same instrumental

effects. A one standard deviation change in the photon efficiency due to a given source results in a corresponding 1σ change in the background efficiency.

The sources of the systematic uncertainties for the CES efficiencies are:

1. the difference of the shower fluctuation between electrons and photons,
2. the difference of the shower shape between electrons and photons,
3. the use of test beam showers taken under slightly different conditions than the collider running,
4. the background composition.

The uncertainty on the difference of the shower fluctuation between electrons and photons comes from the variation of the shower parametrization which are used in the detector simulation. This variation was used to estimate the systematic uncertainty on the shower fluctuation.

The shower shape of photons is slightly different from that of electrons because photon showers start later than electrons. In order to estimate the effect of the difference, we used the electron testbeam result with different material in front of the calorimeter to see the change of CES χ^2 as a function of the shower depth.

In the collider running, the high voltage to the chambers is slightly different from that in the testbeam. Thus the condition of the chamber, such as the saturation in the chamber, was taken into account to estimate the systematic uncertainty on the CES background subtraction.

We changed the background composition N_η/N_{π^0} from 0.75 to 1.3 to estimate the systematic uncertainty.

The effects on the systematic uncertainty from these sources are plotted in Fig. 4.9. It shows the systematic uncertainties on the cross section due to the background subtraction uncertainties as a function of photon p_T, where the total uncertainty and the uncertainties for each source are plotted. For simplicity, only the positive uncertainties are shown. The negative uncertainties are the same fashions.

4.5.1 Constraint on the CES Systematic Uncertainties with CPR

If one assumes that the CES and CPR background subtraction methods work completely well and the systematic uncertainties in the CPR method are completely known, the CES systematic uncertainties can be constrained by looking at a relative difference between the numbers of photons from CES and CPR:

$$\frac{N_\gamma^{CES} - N_\gamma^{CPR}}{N_\gamma^{CPR}} = \frac{N_\gamma^{CES}}{N_\gamma^{CPR}} - 1\,. \tag{4.24}$$

Figure 4.10 shows the ratio of the number of photon events obtained with the CES profile method to that with the CPR conversion method as a function of photon p_T. All points in this plot are in ± 0.1 band within error bars. Since the systematic uncertainty in the CPR method, as is seen in the next section, is reasonably smaller than that in the CES method, the systematic uncertainty in the CES method is constrained by the CPR method to be 10%.

4.6 CPR Conversion Method Efficiencies

The CPR conversion method is an independent scheme from the CES profile method to extract real photon events from the photon candidates. In this section we describe the calculation and calibration of these efficiencies.

4.6.1 CPR signal and background efficiencies

In order to evaluate the CPR efficiencies, we used the following equations of the photon conversion probability [41]

$$\epsilon_\gamma = 1 - \exp(-7/9 \times \mathrm{t}), \tag{4.25}$$

$$\epsilon_b \;=\; 1 \;-\; \exp\,(\,-7/9 \;\times\; \mathrm{t} \;\times\; N_\gamma\,(p_T)\,), \tag{4.26}$$

where t is the amount of materials in front of the CPR in units of radiation length. $N_\gamma\,(P_T)$ is the average number of photons coming from background mesons into the CPR cluster. This changes with the particle type and its p_T. The effect of the particle type is estimated with the simulated π^0, η and K_s^0 with a relative production ratio of $1 : 1.02 : 0.4$ (see section 4.4.1 and 4.4.1).

These efficiencies were corrected for the following effects. First the efficiencies are changed as a function of the polar angle θ of the particle, because the total material for the particle passing through is changed as the θ of the particle is changed. We correct for the effect on event-by-event basis. Next, the effect of the backscattered photons and electrons from an EM shower inside the calorimeter is estimated. These particles are produced during the electromagnetic shower after penetrating the CPR, their momenta are soft, then they are scattered inside the CEM with a large scattering angle, giving signals in the CPR. This correction is estimated with the electromagnetic shower simulation. The last correction, which is applied only to ϵ_γ, is for the effect of the soft photons in the underlying event. It is estimated with the minimum bias triggers.

4.6.2 Calibration for the CPR Efficiencies with the Reconstructed Neutral Mesons

The CPR hit rate measured by the fully reconstructed neutral mesons (π^0, η and ρ) can be used to check the CPR hit rate simulation. Since the CPR was installed to the CDF in 1992, the dataset which was used to calibrate the CPR is different from that used for CES calibration. The data used in this calibration was taken during the 1992-1993 collider run. Figure 4.11 shows the diphoton invariant mass distribution of the π^0 and η mesons, and diphoton plus charged track mass distribution of the ρ meson, with the transverse energy of the leading photons larger than 8 GeV. We calculated the CPR hit rate with these reconstructed neutral mesons by looking at the hit rate of the event

in the peak region (signal plus backgrounds) and that in the sidebands (backgrounds) . The expected CPR hit rate is also calculated with the simulation. These are described in detail in [45][46]. The measured (expected) conversion rate is .842 $\pm$ .008 (.847) for the π^0 , .831 $\pm$ .01 (.842) for the η, and .836 $\pm$ .010 (.834) for the π^0 from ρ meson decay. All measured results and predicted results taking the corresponding detector materials into account show good agreement with each other.

4.7 Sources of the Systematic Uncertainties for CPR Efficiencies

The uncertainties in the CPR efficiencies due to the material count for the solenoid magnet were estimated with the QFL simulation. The uncertainties were

$$\sigma_{\epsilon_{b,material}} = 0.006 \tag{4.27}$$

for the background efficiency and

$$\sigma_{\epsilon_{\gamma,material}} = 0.0078 \tag{4.28}$$

for the photon efficiency.

The uncertainties in the CPR efficiencies due to the backscattered showers inside the CEM were estimated with the EM shower simulation [13]. The uncertainties were

$$\sigma_{\epsilon_{\gamma,backscatter}} = (1 - \epsilon_\gamma) \times P_{bs} \tag{4.29}$$

for photon efficiency and

$$\sigma_{\epsilon_{b,backscatter}} = (1 - \epsilon_b) \times P_{bs} \tag{4.30}$$

for background efficiency. Here P_{bs} is the probability for the backscattered showers and

is parameterized with the shower simulation as,

$$P_{bs} = \frac{7.4 \times 10^{-4} \times p_T}{\sin\theta}. \tag{4.31}$$

where p_T is the momentum of the photons/backgrounds in GeV/c , and θ is a polar angle of the photons/backgrounds.

The uncertainty in the CPR background efficiency due to the background composition was estimated by a same method as in the estimation of the uncertainty in the CES background efficiencies. The uncertainty was

$$\sigma_{\epsilon_{b,bgcomposition}} = 0.008\,. \tag{4.32}$$

4.8 Photon Identification Using CES and CPR Efficiencies

The final plot of the CPR hit rate efficiencies for both photons and backgrounds is shown in Fig. 4.12. It shows the CPR efficiencies at $\sin\theta = 0.9$, where θ is the polar angle of photons and backgrounds. The dotted lines are the bounds of the total systematic uncertainties described above.

Figure 4.8 and Fig. 4.12 show that the CES profile method has a large power for separating signal events from background-contained candidates ($|\epsilon_\gamma - \epsilon_b|$ is large) , but it has a dependence on p_T and degrades the separation power at high p_T. Although the CPR conversion method has a relatively small separation power at low p_T compared with the profile method, it is almost independent of p_T at high p_T region. We use both methods in this measurement. We choose the p_T threshold to be 35 GeV/c, and we use the CES profile method when the EM cluster has $p_T \leq 35$ GeV and otherwise the CPR conversion method.

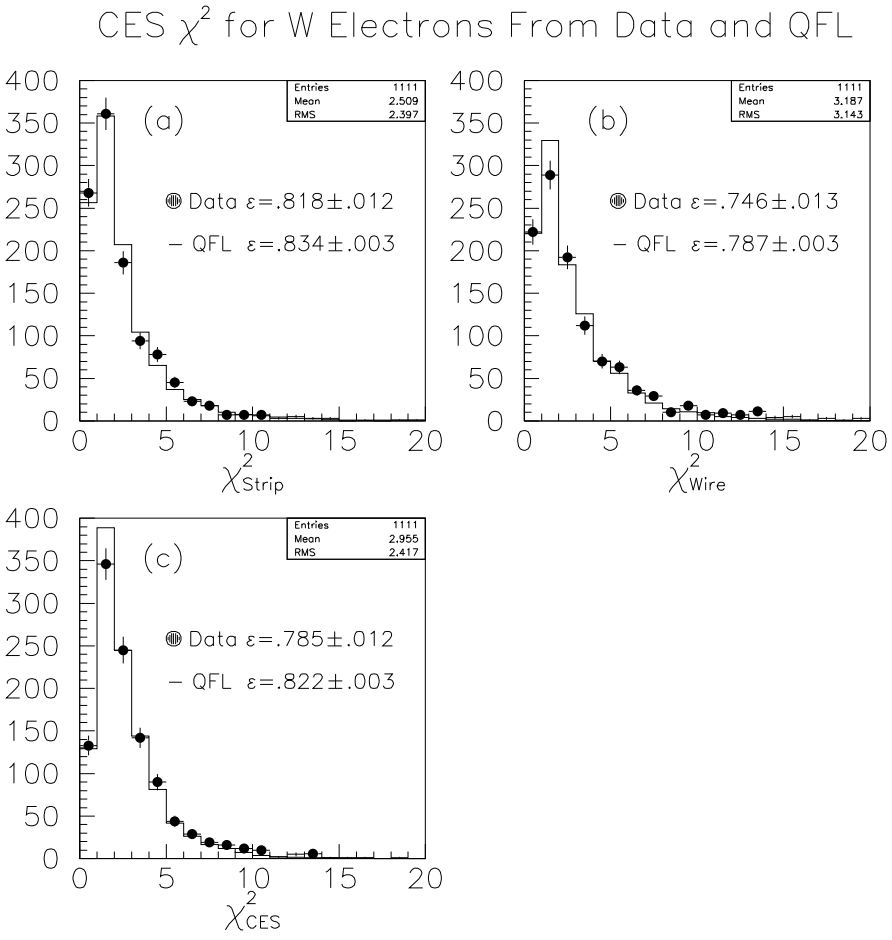

Figure 4.1: Comparison of the CES χ^2 distributions between the real W electrons and the simulated electrons, in (a) strip view, (b) wire view and (c) the average of both views.

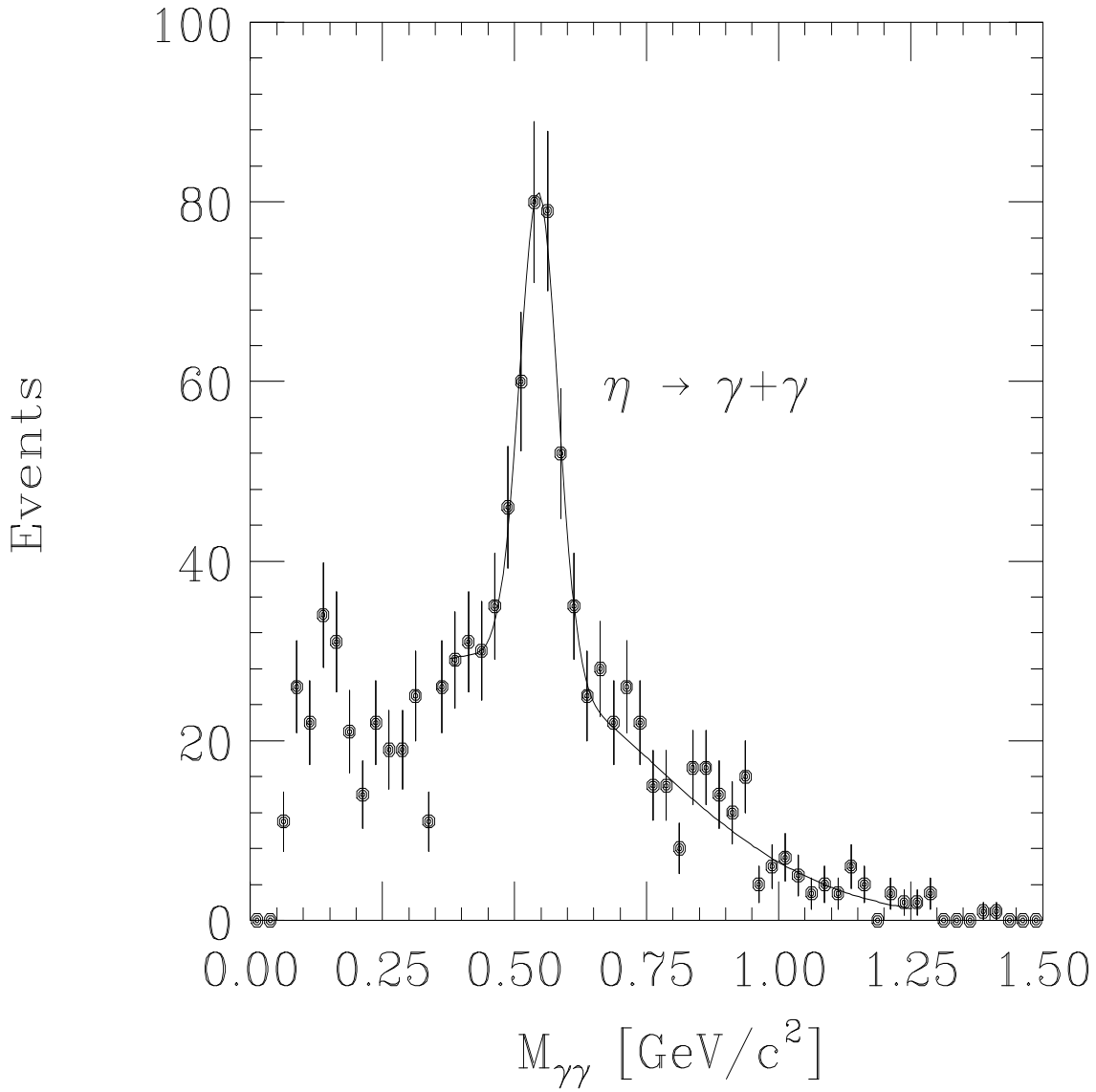

Figure 4.2: Invariant mass distribution of the diphotons in η mass region. The points are the data and the line is a fit to two Gaussians.

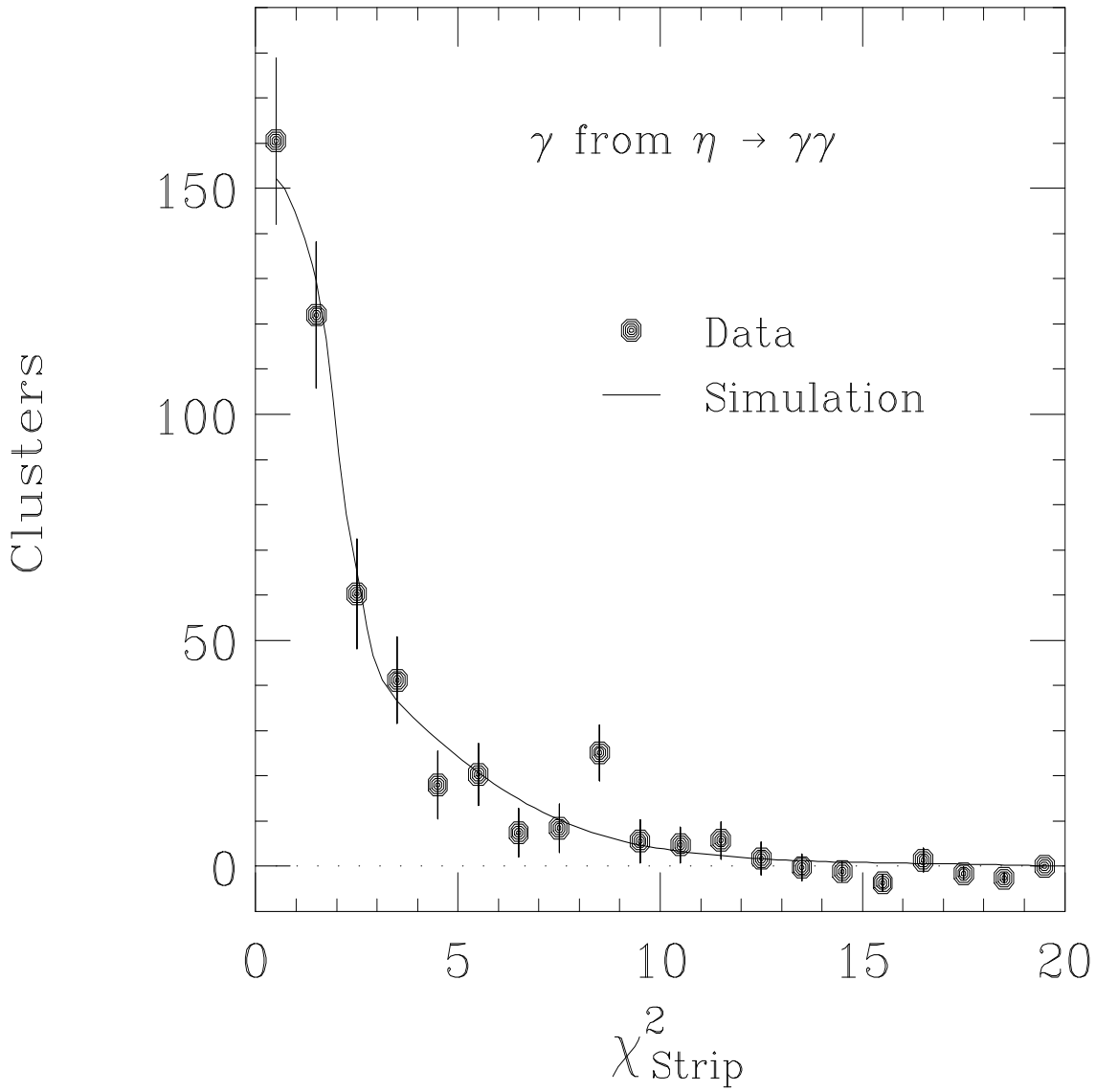

Figure 4.3: The CES χ^2 distributions of the photons from η meson decays in the strip view. The solid line shows the result from the QFL simulation.

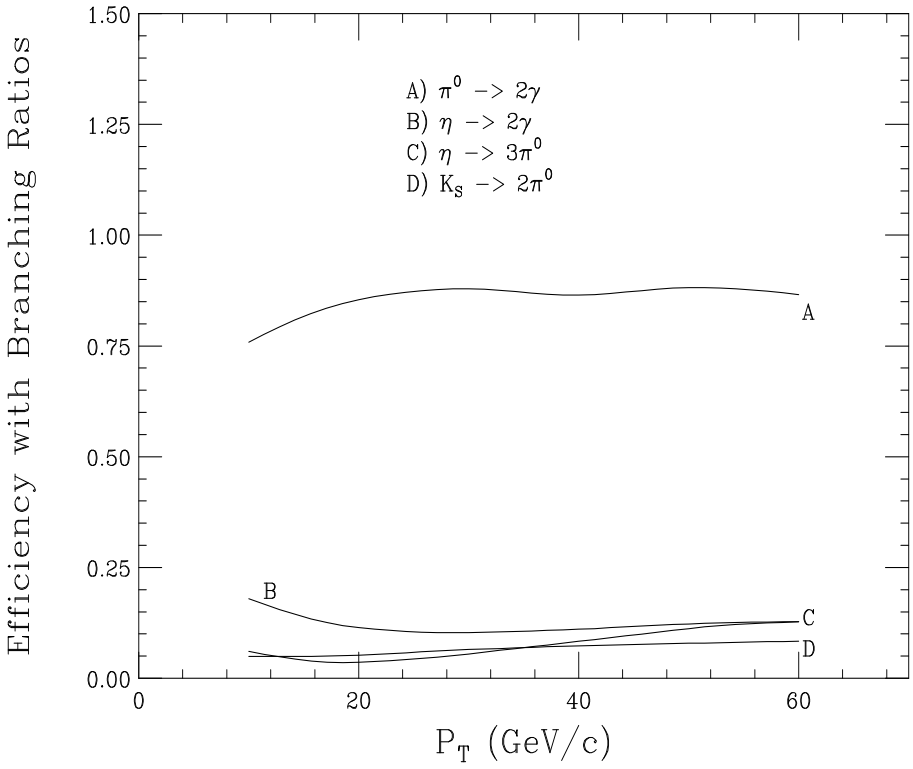

Figure 4.4: The detection efficiency times the branching ratio of each background mesons is shown as a function of the particle p_T.

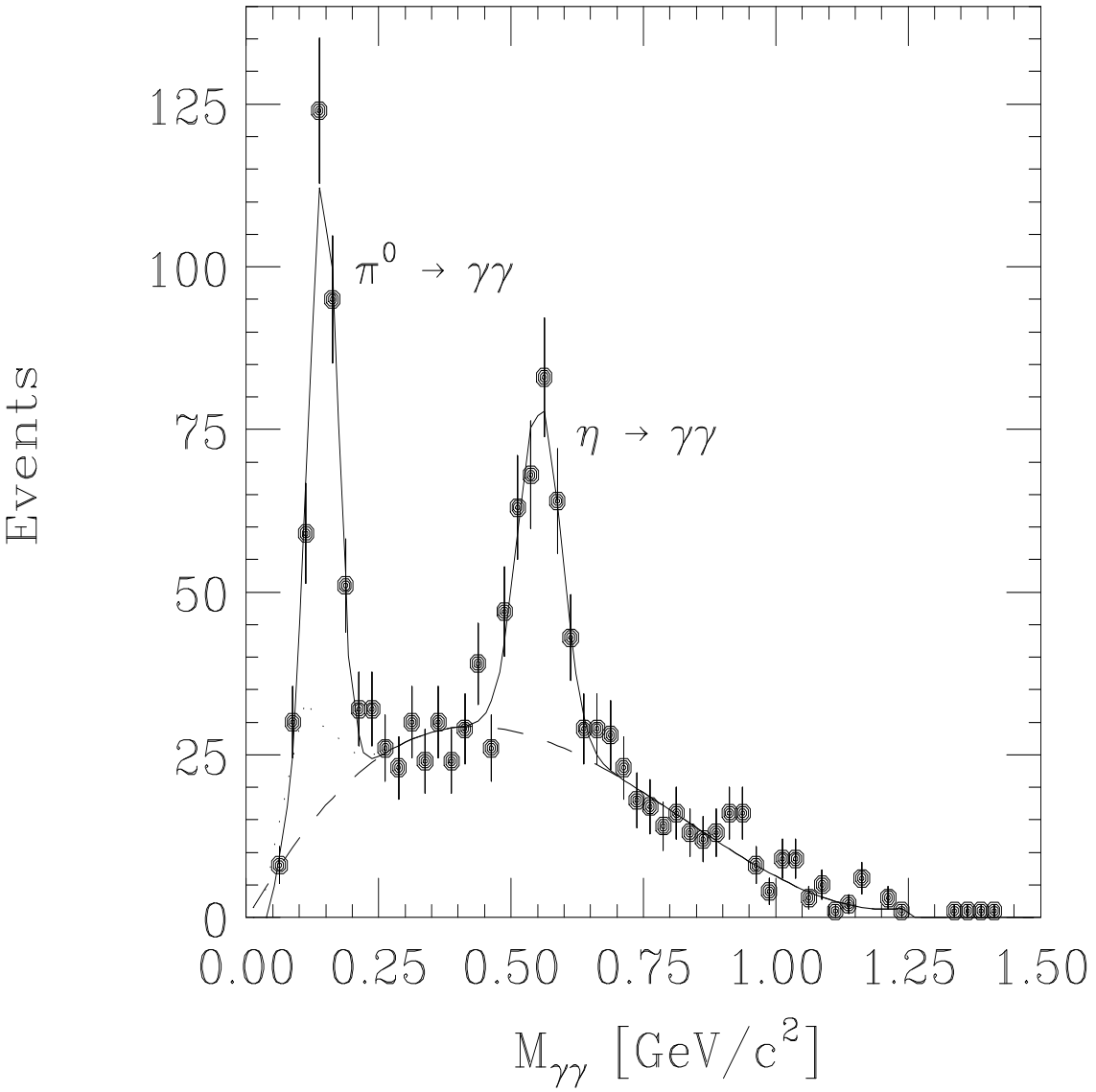

Figure 4.5: Invariant mass distribution of the diphotons in π^0 and η mass region. The solid line is the result of the 2 gaussians plus polynomial fit, the dashed line is the background shape as a result of this fit, and the dotted line is the sum of the contamination of the single photons plus backgrounds.

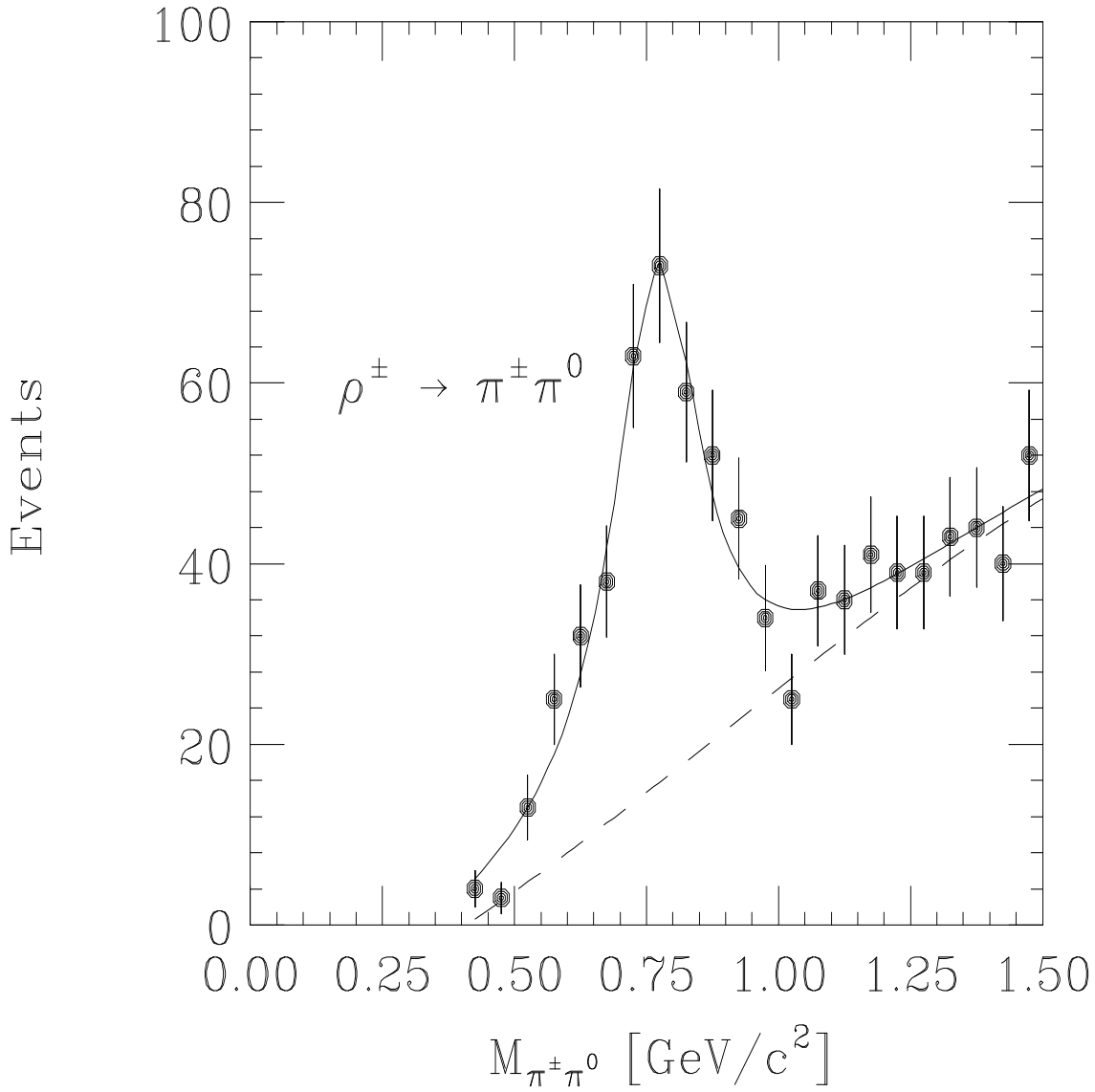

Figure 4.6: Invariant mass distribution of diphotons plus a charged track in ρ mass region. The dashed line is the result of the estimation of the combinatorial background (linear), the solid line is the fitted result of the signal (Breit-Wigner form) plus background shape.

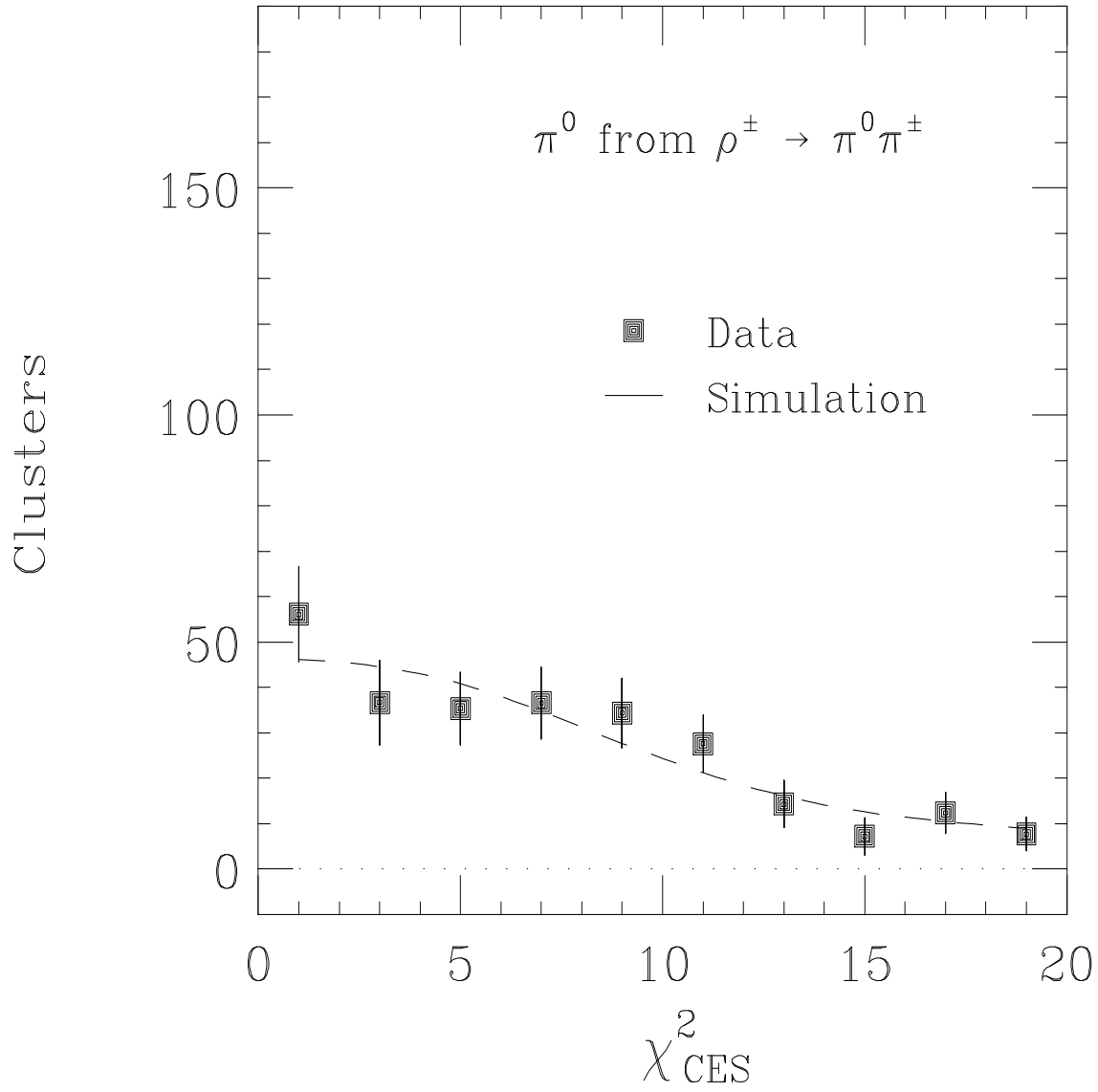

Figure 4.7: The χ^2_{CES} distribution for π^0's from ρ meson decay and that from the simulation.

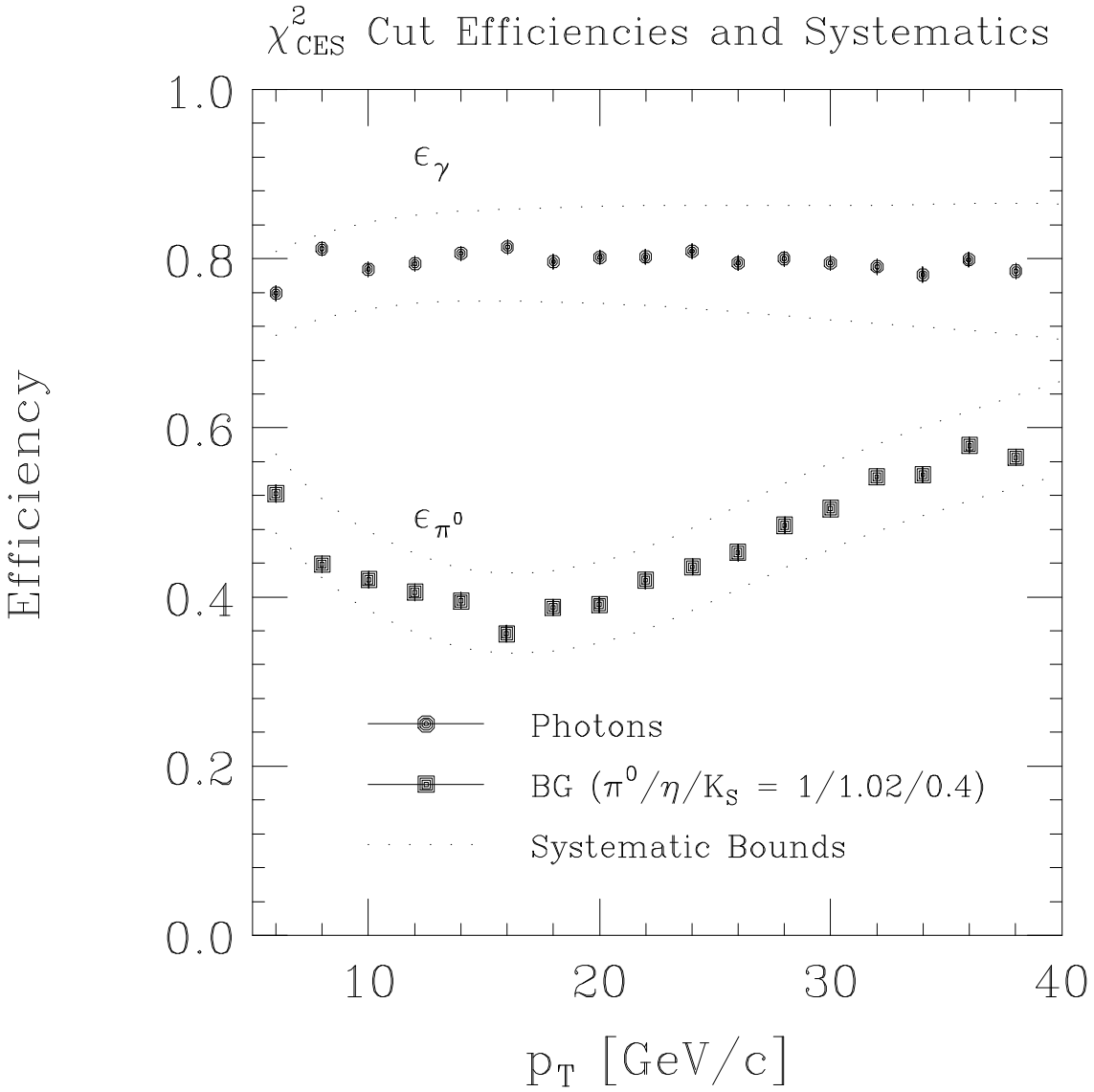

Figure 4.8: $\chi^2_{CES} \leq 4$ cut efficiencies for photons and backgrounds. The dotted lines are the systematic boundaries (see text) of the CES efficiencies.

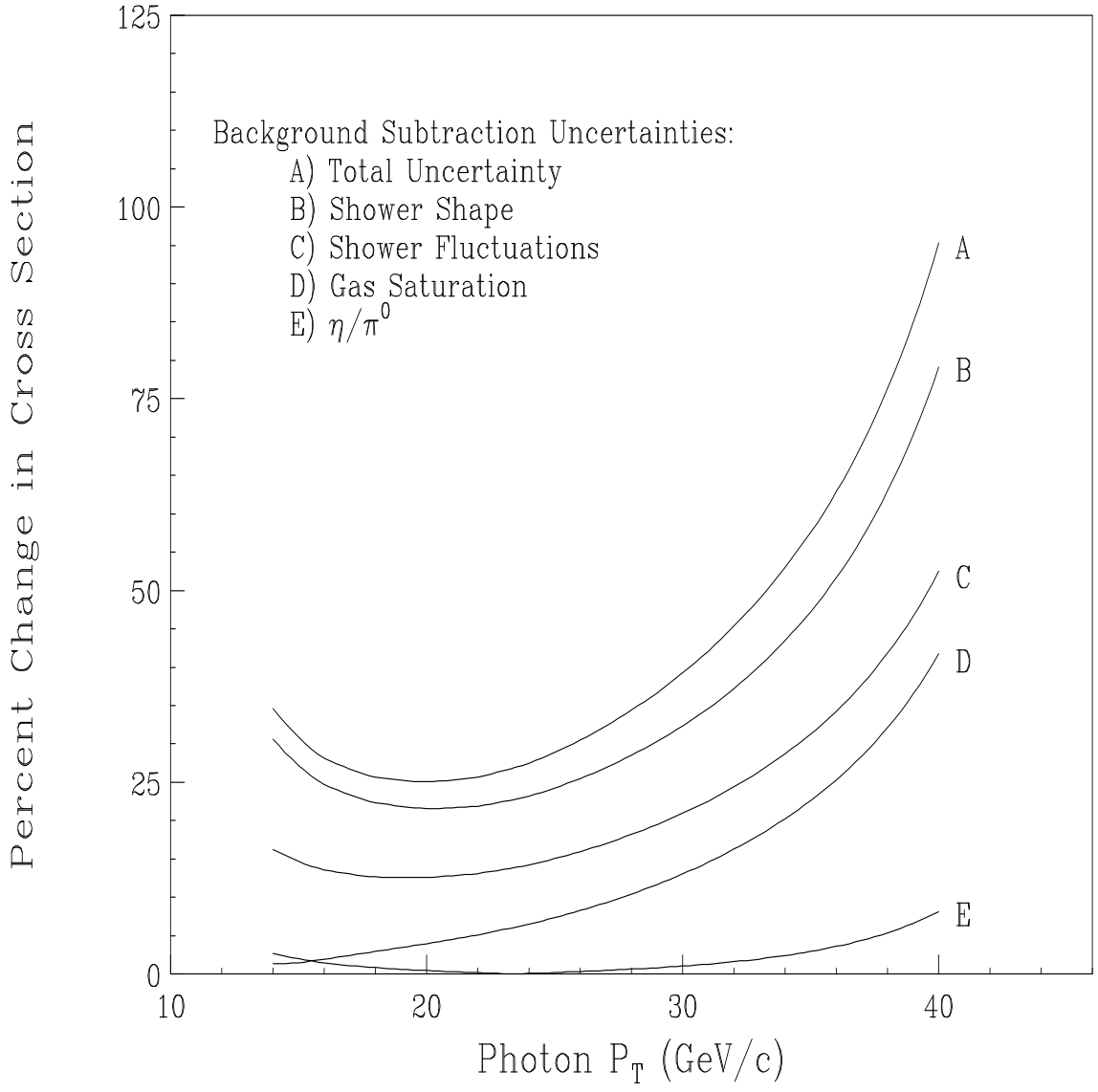

Figure 4.9: Effect of the systematic uncertainties in the χ^2 cut efficiencies on the cross section measurement. Curve A is the total uncertainty, and curves B - E are the uncertainties from each source.

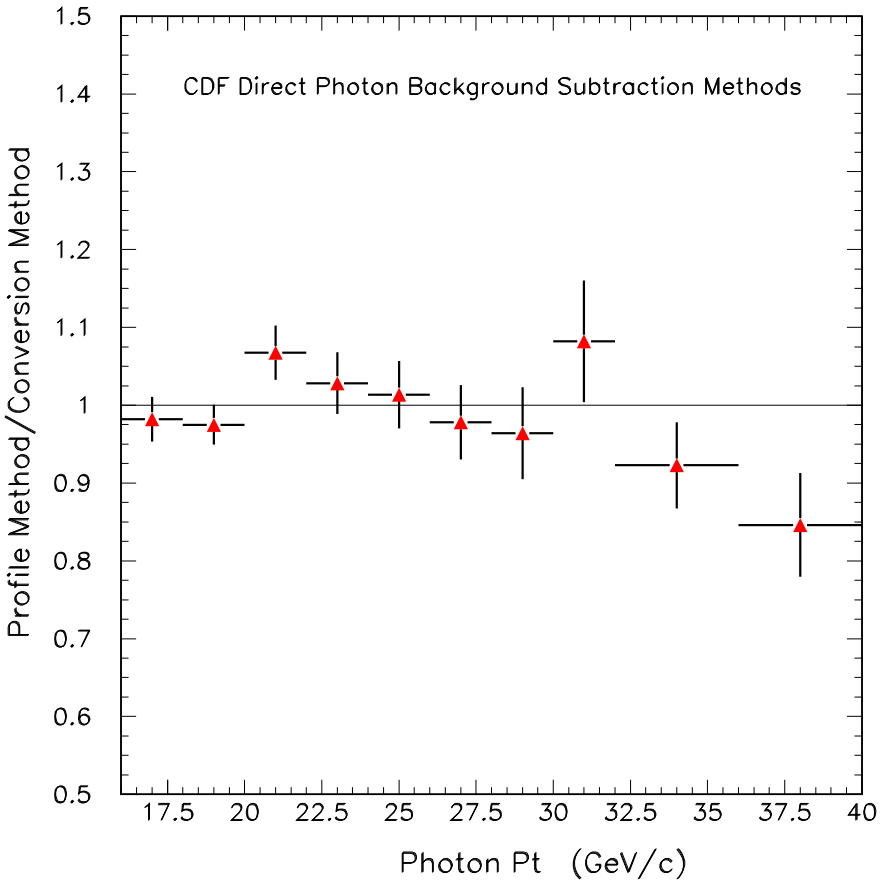

Figure 4.10: Ratio of the number of photons from the profile method and that from the conversion method. The error bars are statistical only.

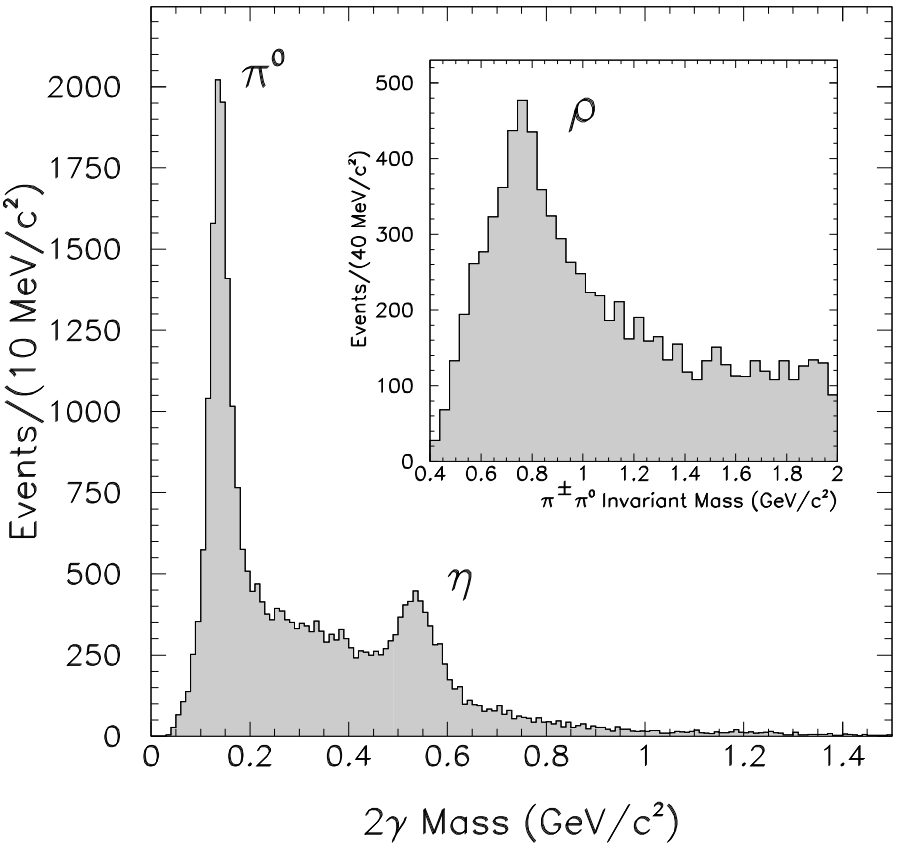

Figure 4.11: Invariant mass distribution of the diphotons in π^0 and η mass region. It was used for the calibration of the CPR conversion method.

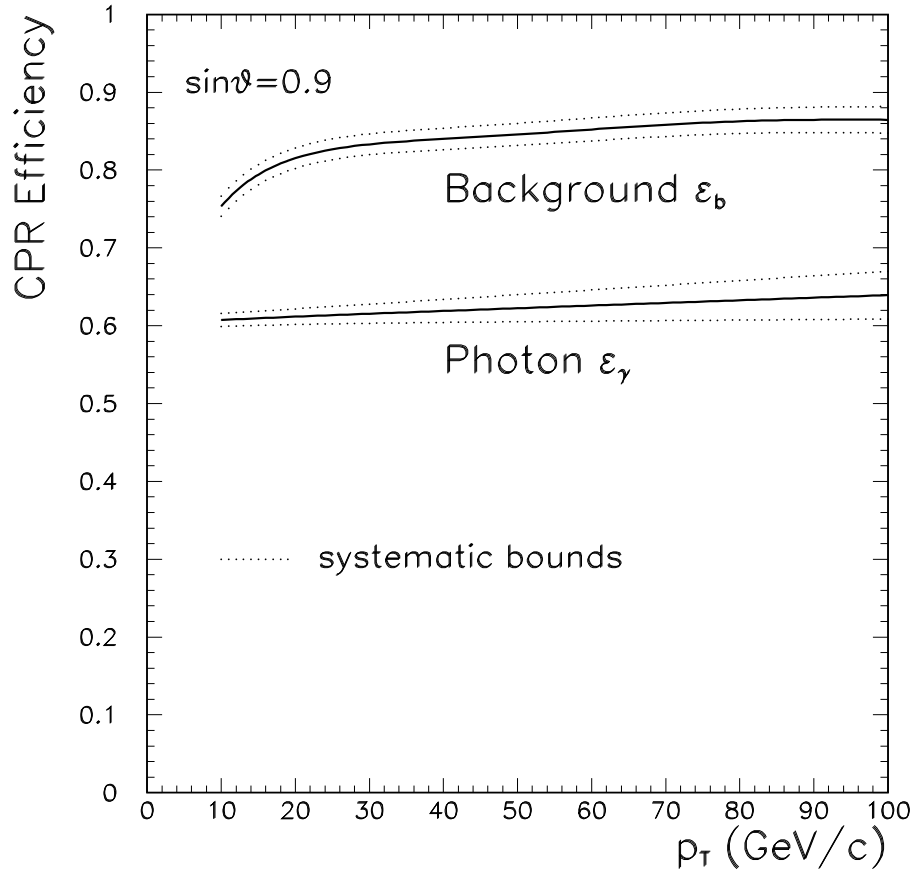

Figure 4.12: The CPR hit efficiencies for both photons and backgrounds at $\sin\theta = 0.9$, where θ is the polar angle of photons and backgrounds. The systematic bounds of the efficiencies are also shown.

Chapter 5

Measuring the Diphoton Cross Section

In this chapter we describe the photon fraction in the diphoton candidates and the diphoton cross section as a function of the photon p_T, the invariant mass of the diphoton system, the azimuthal angle difference between the two photons, the diphoton system p_T, and the p_T ratio of the two photons (Z).

5.1 Result of the Background Subtraction and Final Diphoton Events

The background subtraction described in the previous chapter is applied to the diphoton candidates which are selected in Chapter 3. The result is shown in Table 5.1. The number of total diphoton candidates (N_{TOT}), the estimated real diphoton events ($N_{\gamma\gamma}$) and the background events ($N_{\gamma b} + N_{b\gamma}$, N_{bb}) are shown in each photon p_T bin. Here we put two entries in one event. The number of diphoton events $N_{\gamma\gamma}$ will be used to calculate the photon fraction in the diphoton candidates, and the diphoton cross section.

p_T(GeV/c)	N_{TOT}	$N_{\gamma\gamma}$	$N_{\gamma b} + N_{b\gamma}$	N_{bb}
12-14	348	147.8±32.4	39.0±44.4	161.2±34.5
14-16	255	85.3±26.8	65.6±37.6	104.2±28.6
16-20	292	95.8±28.0	69.4±39.8	126.7±30.8
20-24	126	92.6±21.4	-14.9±27.7	48.4±21.5
24-30	61	26.1±17.4	9.0±24.4	25.9±18.4
30-48	50	50.8±34.6	-32.3±41.1	31.6±24.5

Table 5.1: The results of the background subtraction described in Chapter 4.

5.2 Photon Fraction in Diphoton Candidates

The photon fraction in our diphoton candidates is defined by

$$\text{Photon Fraction} \equiv \frac{N_{\gamma\gamma}}{N_{TOT}}, \tag{5.1}$$

where $N_{\gamma\gamma}$ is the number of real diphoton events and N_{TOT} is the number of total diphoton candidate events. The measured photon fraction is plotted as a function of p_T of the photons in Fig. 5.1. It shows that the photon fraction becomes higher when p_T becomes larger, although the statistics are low.

We have also measured the photon fraction in the inclusive photon sample, which is shown in Fig. 5.2. Here we can see more clearly that the photon selection criteria used in this analysis make the candidates pure at high p_T region.

5.3 The Diphoton Cross Section

In this section we show the procedure for evaluating the diphoton cross section. The results are compared with the NLO QCD calculation of $\bar{\text{p}}\text{p} \to \gamma\gamma X$ [11]. The systematic uncertainties from various sources are summarized.

5.3.1 Evaluation of the Diphoton Cross Section

The diphoton cross section is calculated by using the number of real diphoton events $N_{\gamma\gamma}$ and correcting for the efficiencies of each selection criterion and the level 2 trigger.

The diphoton cross section as a function of the photon p_T is calculated by

$$\frac{d\sigma_{\gamma\gamma}}{dp_T} = \frac{N_{\gamma\gamma}}{\epsilon_{\rm TOT} L \Delta p_T}, \tag{5.2}$$

where $N_{\gamma\gamma}$ is the number of diphotons listed in Table 5.1, Δp_T is the width of each p_T bin, L is the total integrated luminosity and $\epsilon_{\rm TOT}$ is the total efficiency. The total luminosity accumulated by the diphoton trigger system was 101.1 pb^{-1}. The total efficiency ϵ_{TOT} is given by the product of the efficiencies of each selection criterion,

$$\epsilon_{\rm TOT} = \epsilon_{\rm fid}{}^{(1)} \cdot \epsilon_{\rm fid}{}^{(2)} \cdot \epsilon_{\rm conv}{}^{(1)} \cdot \epsilon_{\rm conv}{}^{(2)} \cdot \epsilon_{\rm trk}{}^{(1)} \cdot \epsilon_{\rm trk}{}^{(2)} \cdot \epsilon_{\rm iso}{}^{(1)} \cdot \epsilon_{\rm iso}{}^{(2)} \cdot \epsilon_{\rm zvert} \cdot \epsilon_{\rm ext}{}^{(1)} \cdot \epsilon_{\rm ext}{}^{(2)} \cdot \epsilon_{\rm L2} \,. \tag{5.3}$$

where $\epsilon_{\rm fid}$, $\epsilon_{\rm conv}$ ... are given in Table 3.3 in Chapter 3.

Figure 5.3 shows the diphoton cross section as a function of the photon p_T, where each event is entered twice, once for each p_T of the two photons. The solid line shows the NLO QCD prediction with CTEQ2M [10] structure functions. The NLO QCD prediction includes the energy isolation cut (extra energy in cone $0.4 \leq 1\,\text{GeV}$) and rapidity cut ($|\eta_\gamma| \leq 0.9$). The statistical and systematic uncertainties in the diphoton cross section are shown in this plot. The result is in qualitative agreement with the NLO QCD prediction. The numerical values for the diphoton cross section are listed in Table 5.2.

We also measured the diphoton cross section as a function of the invariant mass of the diphotons M, the azimuthal angle between two photons $\Delta\phi$, the diphoton system

p_T(GeV/c)	$\langle p_T \rangle$	$d\sigma_{\gamma\gamma}/dp_T$(pb/GeV/c)	Stat. (%)	Sys. (%)
12-14	13.0	4.95	17	21
14-16	14.9	3.00	23	21
16-20	17.7	1.94	19	21
20-24	21.6	1.45	20	21
24-30	26.6	0.38	42	20
30-48	35.5	0.22	49	21

Table 5.2: The diphoton cross section as a function of the photon p_T. The statistical and systematic errors are also listed. We put two entries per event.

M(GeV/c^2)	$\langle M \rangle$	$d\sigma_{\gamma\gamma}/dM$(pb/GeV/c^2)	Stat. (%)	Sys. (%)
10-20	15.2	0.166	39	21
20-25	23.4	0.399	48	20
25-30	27.7	0.739	30	21
30-35	32.3	0.650	33	21
35-45	38.8	0.232	44	21
45-60	50.3	0.166	39	20
60-120	75.7	0.0179	125	21

Table 5.3: The diphoton cross section as a function of the invariant mass of the diphotons M. The statistical and systematic errors are also listed.

$\Delta\phi$(Rad)	$\langle \Delta\phi \rangle$	$d\sigma_{\gamma\gamma}/d\Delta\phi$(pb/Rad)	Stat. (%)	Sys. (%)
2.62-2.84	2.74	4.00	116	21
2.84-2.94	2.89	18.8	56	20
2.94-3.04	2.99	43.1	24	21
3.04-3.09	3.06	49.5	34	21
3.09-3.14	3.12	58.9	56	21

Table 5.4: The diphoton cross section as a function of the $\Delta\phi$ between the diphotons. The statistical and systematic errors are also listed.

p_T(GeV/c)	$\langle p_T \rangle$	$d\sigma_{\gamma\gamma}/dp_T$(pb/GeV/c)	Stat. (%)	Sys. (%)
0-1	0.66	1.33	46	21
1-3	2.11	1.46	34	21
3-5	3.98	1.27	40	20
5-8	6.58	1.02	52	21
8-13	10.1	0.53	36	21

Table 5.5: The diphoton cross section as a function of the p_T of the diphoton system. The statistical and systematic errors are also listed.

Z	$\langle Z \rangle$	$d\sigma_{\gamma\gamma}/dZ$(pb)	Stat. (%)	Sys. (%)
0.45-0.70	0.617	17.5	27	21
0.70-0.85	0.784	28.3	33	21
0.85-0.95	0.898	28.9	57	21
0.95-1.00	0.970	46.5	39	21

Table 5.6: The diphoton cross section as a function of the p_T ratio of the diphotons Z. The statistical and systematic errors are also listed.

p_T, and the p_T ratio of the photons Z. The Z is defined by

$$Z = \frac{p_T^{(2)}}{p_T^{(1)}}, \tag{5.4}$$

where $p_T^{(1)}$ and $p_T^{(2)}$ are the p_T's of the leading and next leading photons, respectively. The results are plotted in Figs. 5.4, 5.5, 5.6 and 5.7. The numerical values are listed in Tables 5.3, 5.4, 5.5 and 5.6.

The cross sections as a function of the invariant mass and $\Delta\phi$ are in qualitative agreement with the NLO prediction, while the cross sections as a function of the diphoton system p_T and the Z show slight differences compared with the theory.

5.3.2 Summary of the Systematic Uncertainties

In Table 5.7 we summarize the systematic uncertainties in the measured cross section.

ITEM	*VALUE*
Uncertainty in CES background subtraction	15 % ($12 \leq E_T \leq 30$ GeV)
Uncertainty in CPR background subtraction	10 % ($E_T \geq 30$ GeV)
Uncertainty in L2 Trigger Efficiency	2 %
Uncertainty in Isolation Cut	1 %
Uncertainty in no-tracks requirement	1 %
Uncertainty in Photon Energy Scale	4.5 %
Uncertainty in Luminosity	8 %

Table 5.7: Summary of the systematic uncertainties.

The uncertainties on the background subtraction with the CES and the CPR come from the uncertainties in the efficiencies for the CES profile method and the CPR conversion method, which are described in chapter 4. They make a contribution of 15 % cross section uncertainty in the CES method and 10 % in the CPR method.

The total systematic uncertainty is 21%. It is dominated by the uncertainty from the background subtraction.

5.4 Comparison with the Previous CDF Measurement

Here we present a list of improvements in the diphoton cross section measurement in this analysis, compared with the previous diphoton cross section measurement [19].

Integrated Luminosity

The integrated luminosity accumulated by the CDF diphoton trigger during the 1992-1995 collider run was 101.1pb^{-1}, which was about 24 times larger than the previous diphoton analysis (4.3pb^{-1} during the 1988-1989 collider run).

Diphoton Trigger

The level 2 diphoton trigger was changed. The isolation criterion using the neural network system. was added. We evaluated the trigger efficiency with the dielectron sample. The efficiency was measured to be 0.84 ± 0.02.

Isolation Criterion

At offline we used the extra transverse energy in the cone $0.4 \leq 1$ GeV as an isolation criterion, and the efficiency of the criterion to the signal was evaluated. It had a good efficiency for photons (90%) and rejected the backgrounds effectively.

CPR Conversion Method

In the previous diphoton measurement, only the CES was used to subtract the backgrounds. The diphoton cross section as a function of the photon p_T had been measured up to $p_T \leq 19$ GeV. The systematic uncertainty was about 40% (see Table 1.1 in Chapter 1). In this analysis, we used the CES and the CPR for the background subtraction. The CPR had a smaller systematic uncertainty at high p_T than the CES

(see Figs. 4.8 and 4.12 in Chapter 4). By using the CPR in addition to the CES, we were able to measure the diphoton cross section up to $p_T \leq 48\,\mathrm{GeV}$ or $M \leq 120\,\mathrm{GeV}/c^2$.

Photon Fraction in the Diphoton Candidates

We measured the photon fraction as a function of the photon p_T. We found that the selection criteria used in this analysis made the diphoton candidates more pure at high p_T.

Comparison of the Diphoton p_T Cross Section with the Previous Diphoton Result

In the previous diphoton cross section measurement, the cross section as a function of the photon p_T was about 3 times larger than the NLO prediction, although the statistics was limited (see Fig. 1.8 in Chapter 1).

We compare the present result of the diphoton cross section as a function of the photon p_T with the previous diphoton result at CDF in Fig. 5.8, where the circles show the present result and the triangles show the previous result with the total integrated luminosity of $4.3\,\mathrm{pb}^{-1}$. The result of this analysis is in agreement with the previous diphoton result within error bars. The difference between the data and the NLO prediction which was seen in the previous measurement is not seen in the present measurement with higher statistics.

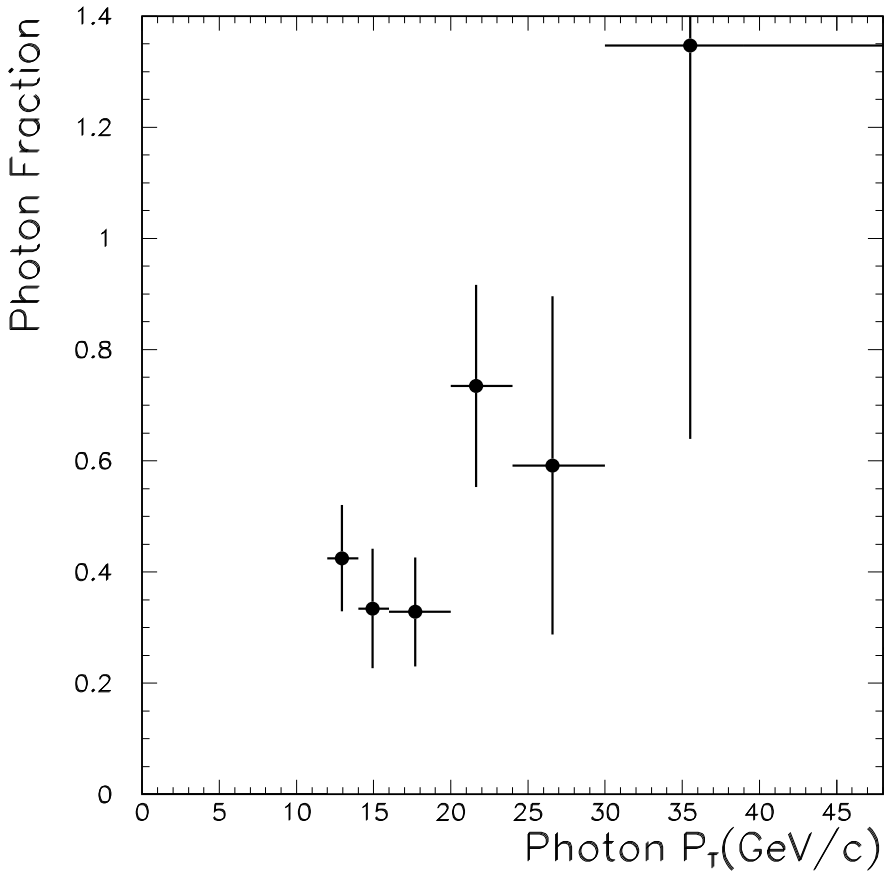

Figure 5.1: Photon fraction in the diphoton candidate events as a function of the photon p_T. In this plot we put two entries per event.

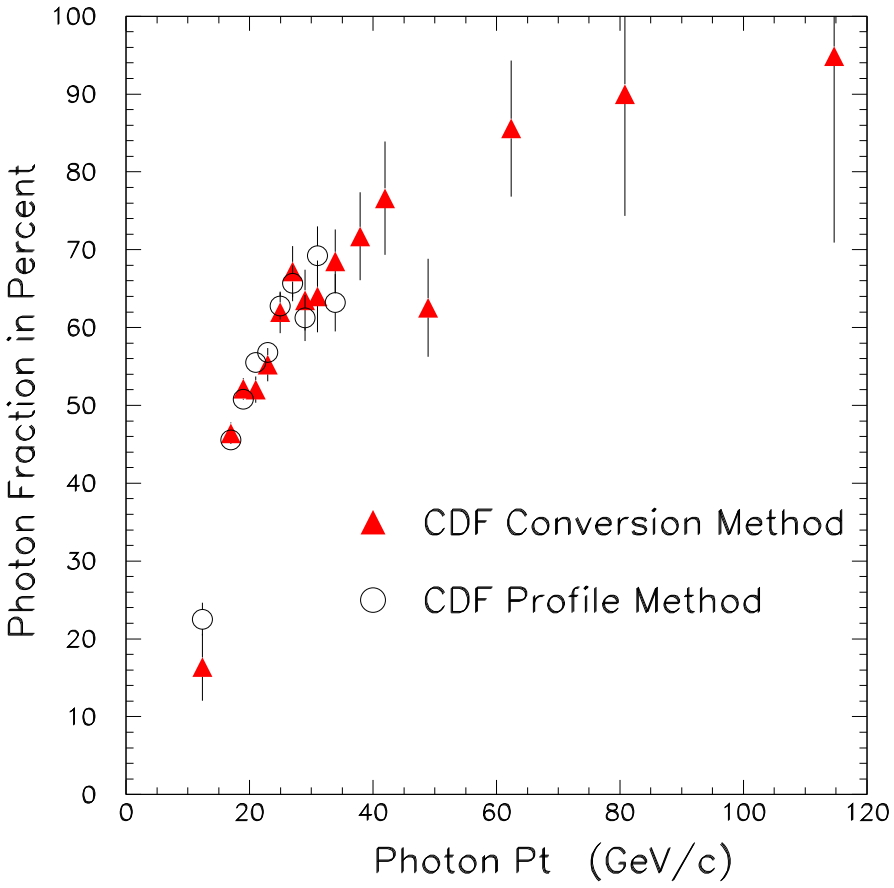

Figure 5.2: Photon fraction in the inclusive photon sample as a function of the photon p_T. The open circles show the photon fraction measured by the CES method, and the triangles show the photon fraction measured by the CPR method.

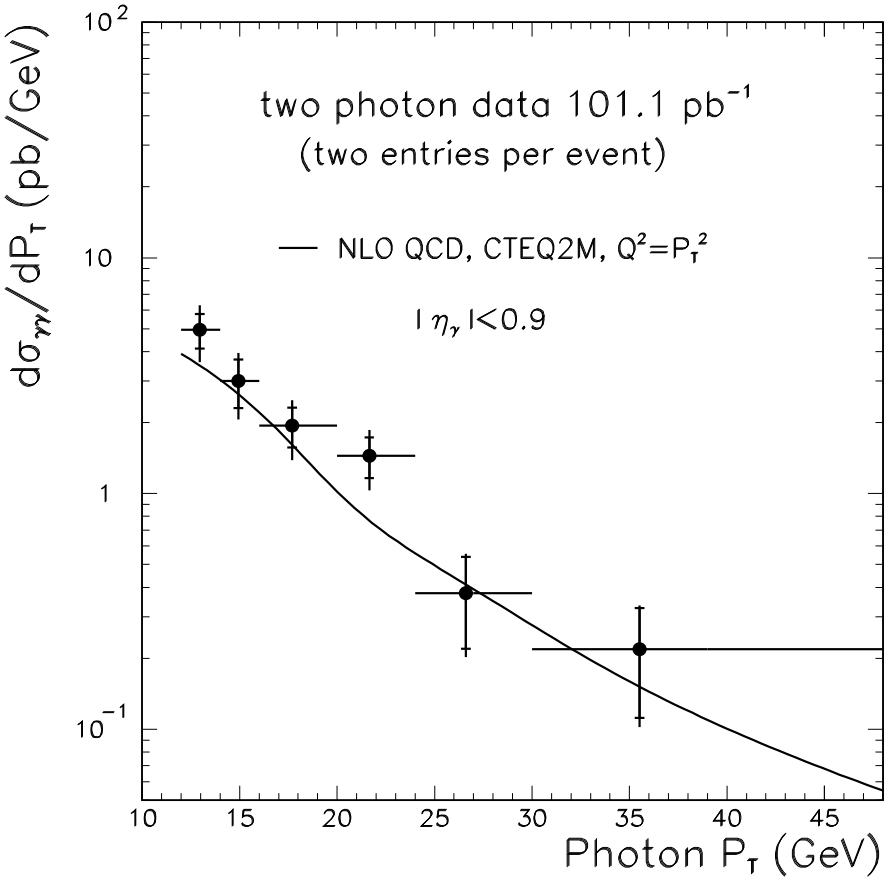

Figure 5.3: The cross section for diphoton production as a function of the photon p_T. The points show the measured cross section. The statistical errors and the quadratic sum of the statistical and systematic errors are shown. The solid line shows the NLO QCD prediction with the CTEQ2M parton distribution functions.

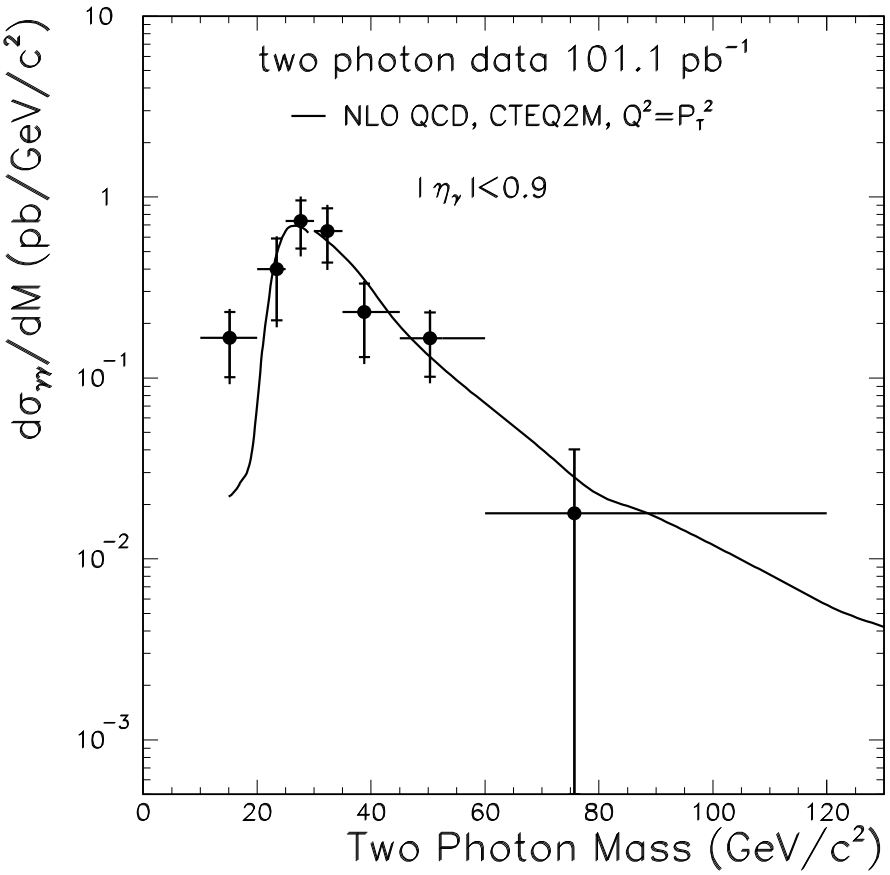

Figure 5.4: The cross section for diphoton production as a function of the invariant mass of the diphotons. The solid line shows the NLO QCD prediction.

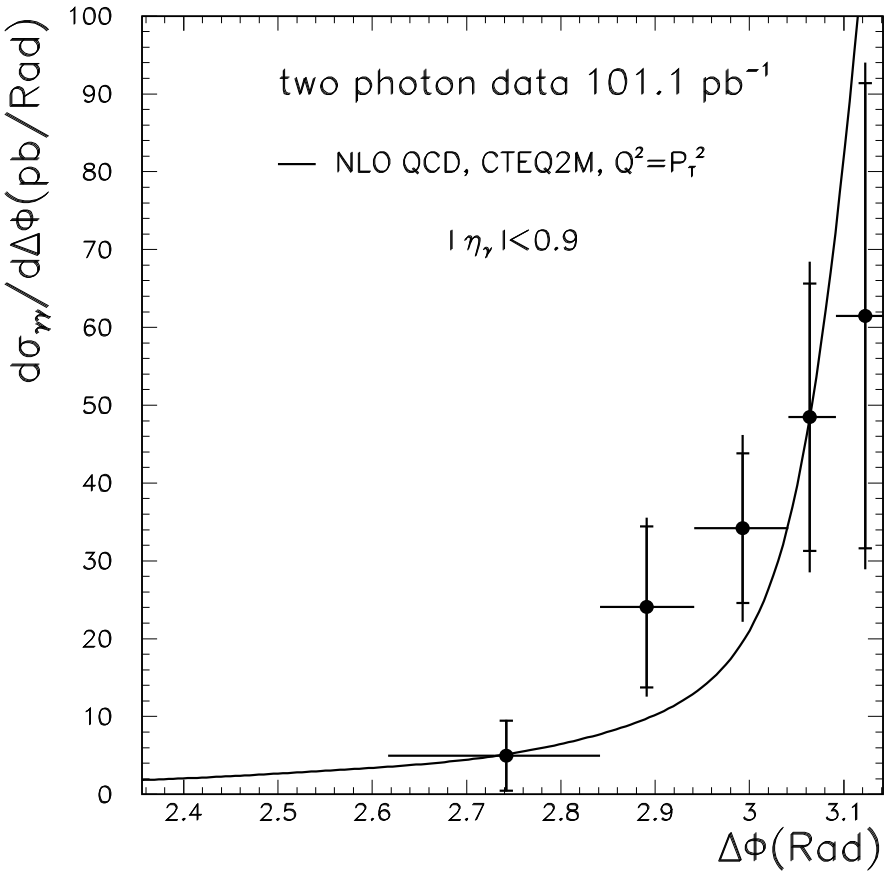

Figure 5.5: The cross section for diphoton production as a function of $\Delta\phi$ between the two photons. The solid line shows the NLO QCD prediction.

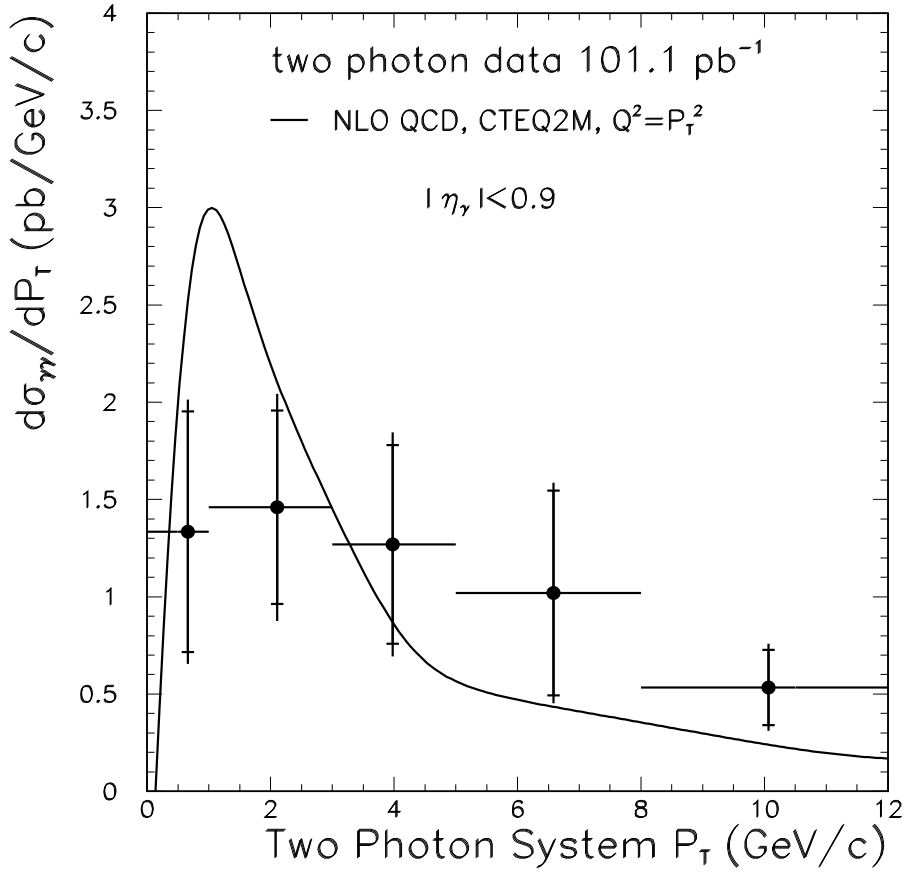

Figure 5.6: The cross section for diphoton production as a function of the system p_T of the diphotons. The solid line shows the NLO QCD prediction.

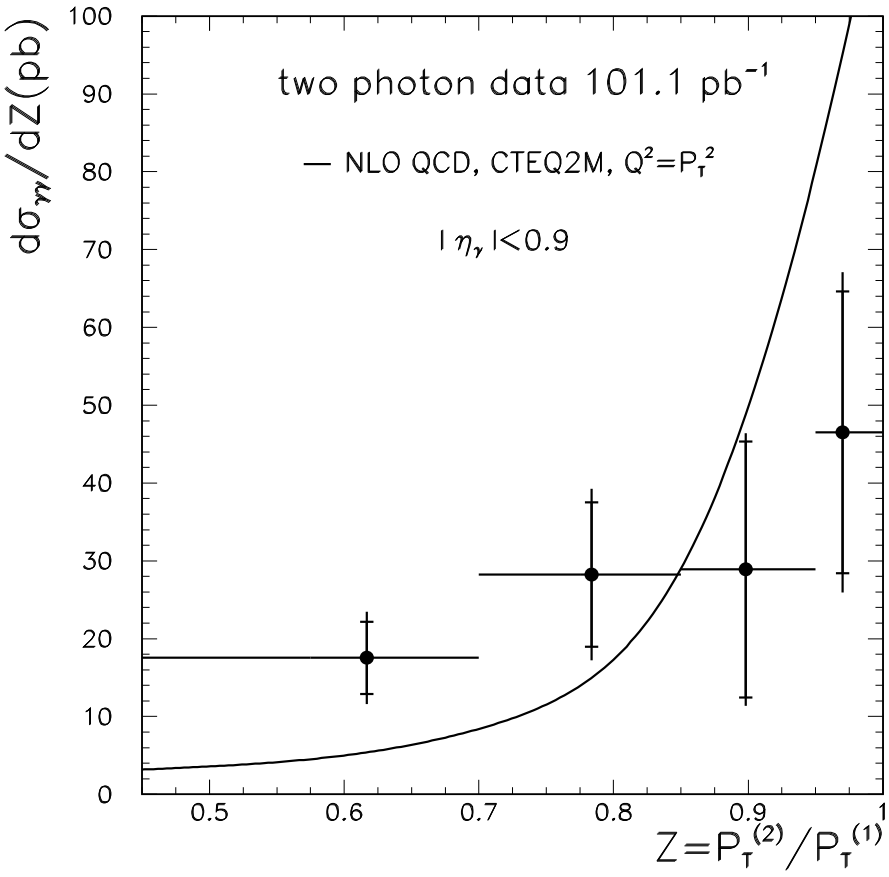

Figure 5.7: The cross section for diphoton production as a function of the p_T ratio of the diphotons. The solid line shows the NLO QCD prediction.

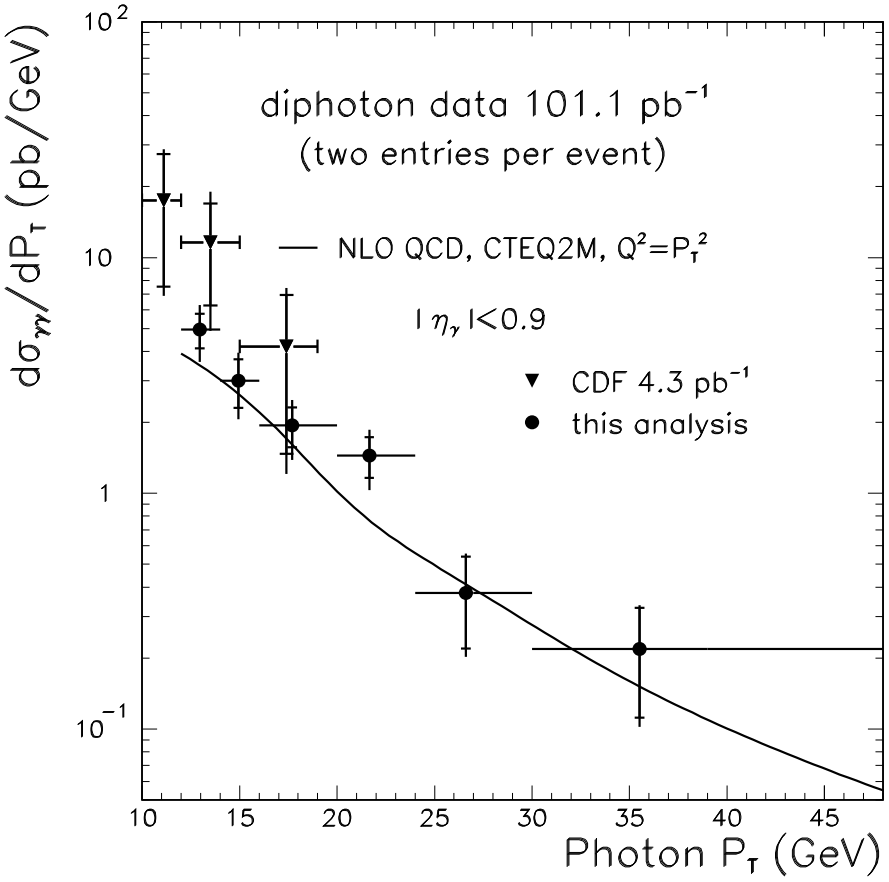

Figure 5.8: The present result of the diphoton cross section as a function of the photon p_T (circles) is compared with the previous diphoton result at CDF (triangles) .

Chapter 6

Conclusion

We have measured the prompt diphoton production cross section in $\bar{p}p$ collisions at a center-of-mass energy of $\sqrt{s} = 1.8\,\mathrm{TeV}$. The total integrated luminosity was about $110\mathrm{pb}^{-1}$, which was about 24 times larger than that in the previous CDF diphoton measurement.

The level 2 diphoton trigger included the isolation criterion, and the efficiency of the trigger was studied. The level 2 trigger efficiency was evaluated to be 0.84 ± 0.02.

In offline analysis, the isolation criteria of extra transverse energy in the cone $0.4 \leq 1\,\mathrm{GeV}$ was used, and its efficiency for the diphotons was studied. The isolation cut efficiency for the diphotons was estimated to be about 90%.

We used the CES profile method and the CPR conversion method to subtract the background events. We used the CPR conversion method at high p_T events. As a result, we were able to measure the diphoton cross section up to $p_T \leq 48\,\mathrm{GeV/c}$.

We measured the photon fraction as a function of the photon p_T. It showed that the selection criteria used in this analysis made the diphoton candidates more pure at high p_T.

The differential cross section was evaluated as a function of the photon p_T, the invariant mass of the diphotons M, the azimuthal angle between the two photons $\Delta\phi$, the p_T ratio of the two photons $Z = p_T^{(2)}/p_T^{(1)}$ and the transverse momentum of the diphoton

system. The total systematic uncertainty in the diphoton cross section measurement was estimated to be 21%.

We compared the result of the diphoton cross section with the NLO QCD predictions with CTEQ2M parton distribution functions. The diphoton cross section as a function of the photon p_T was in qualitative agreement with the theory. It was also consistent with the previous diphoton cross section measurement within error bars. The cross section as a function of the invariant mass and $\Delta\phi$ were in qualitative agreement with the theory. Slight differences between the data and the theory were seen in the diphoton cross section as a function of the diphoton system p_T and of the p_T ratio.

Appendix A

The Standard Selection Criteria for Electrons

In this appendix we describe the standard selection criteria for electrons used in CDF.

A.1 The Selection Criteria for Electrons

A.1.1 3D Track Cut

The CTC is operated in an axial magnetic field. Charged particles follow a helical trajectory. The helix is defined by the 5 parameters, curvature C (inverse diameter of the circle in $R-\phi$), impact parameter D_0 (distance of closest approach to $R=0$), ϕ_0 (azimuthal direction at the point of closest approach to $R=0$), z_0 (the z position at the point of closest approach to $R=0$), and $\cot\theta$, where θ is the polar angle.

The number of 3D tracks pointing at the EM cluster is defined by the number of 3D tracks whose extrapolated positions to the CEM are inside the EM cluster. In the

standard electron analysis in the CDF, the EM cluster is required to have

$$\text{Number of 3D tracks} \geq 1, \tag{A.1}$$

for high p_T electron analysis. In low p_T electron analysis, a tighter criterion of the 3D tracks

$$\text{Number of 3D tracks} = 1, \tag{A.2}$$

is required to the EM cluster in order to reduce the backgrounds in the electron candidates.

A.1.2 E/P

The variable we call E/P is defined by

$$E/P \equiv \frac{E_T}{p_T}, \tag{A.3}$$

where E_T is the transverse energy measured in CEM, p_T is the transverse momentum measured in CTC. Ideally the ratio of E_T and p_T for electrons should be 1. The shape of E/P distribution becomes broad due to finite resolutions in measuring E_T and p_T, and it has a longer tail at high E/P because of the bremsstrahlung.

In the CDF standard electron selection criteria, E/P is required to be

$$E\,/\,P \leq 1.8. \tag{A.4}$$

A.1.3 Had/EM

As the CEM is designed so that the electron deposits almost its energy to the CEM, the ratio of the transverse energy in the CHA and that in the CEM, called Had/EM, is a good parameter to discriminate the backgrounds from electrons. In the standard

electron analysis, the following criterion

$$Had/EM \leq 0.05\,, \tag{A.5}$$

is required to the electron dataset.

A.1.4 Lateral Shower Sharing: L_{shr}

The CEM tower is large enough to contain a full EM shower. If an electron hits a region in a CEM tower well away from its boundary, the electron deposits its energy on that tower, and nearly none on two adjacent towers in η direction. On the other hand, in the case of multiple particles from QCD events, energy deposition in the CEM tower adjacent to the seed tower (the tower in which the particles hit) will be different from that in the electron case.

In order to reject the multiple particle backgrounds, we define a variable "lateral shower sharing (L_{shr}) :

$$L_{shr} \equiv 0.14 \sum_i \frac{E_i^{meas} - E_i^{pred}}{\sqrt{(\Delta E)^2 + \left(\Delta E_i^{pred}\right)^2}}\,, \tag{A.6}$$

where E_i^{meas} is the energy deposition in the CEM tower i, E_i^{pred} is the expected energy deposition in the CEM tower i, ΔE is the uncertainty in the energy measurement with the CEM ($\Delta E = 0.14/\sqrt{E}$) and ΔE_i^{pred} is the error associated with E_i^{pred}. The sum runs over the two towers in η direction adjacent to the seed tower. E_i^{pred} is determined by the CDF testbeam data, as a function of the seed tower energy and the direction of the CES shower center relative to the event vertex. ΔE_i^{pred} is given by the propagation of the error of the shower center measurement in the CES to the predicted energy E_i^{pred}.

In the electron selection, it is required to be a small value:

$$L_{shr} \leq 0.2. \tag{A.7}$$

A.1.5 Lateral Shower Profile: CES χ^2

In electron analysis, the difference of the lateral shower profile at the shower maximum region between electrons and multiple particles from QCD events are used to reject the backgrounds. Using the definition of Eq. 3.11, we require the events to have

$$\chi^2_{strip} \leq 10. \tag{A.8}$$

A.1.6 Position Matching between the Track and CES Hit Position

In order to reject the multiple particle backgrounds, we require the matching of the 3D track and the CES hit position. Here the CES hit position is defined by the position of the seed CES cluster in the CEM cluster. In electron analysis we required the events to satisfy

$$|\Delta x| \leq 1.5\text{cm}, \tag{A.9}$$

$$|\Delta z| \leq 2.5\text{cm}, \tag{A.10}$$

where $|\Delta x|$ ($|\Delta z|$) is the position difference between the track and the hit position in X_{CES} (Z_{CES}) view in the CES coordinate.

Appendix B

Standard CES Profile

In this appendix we describe the standard CES profiles for electrons which were evaluated from the CDF central calorimeter testbeam done at 1985.

B.1 Standard CES Profile

The profiles are evaluated for both the CES analysis and the QFL simulations. We define $f(x)$ and $I(x)$, the instantaneous and the integrated fractional energies in 1 mm bins respectively:

$$f(x) = \int_{x-1}^{x} \rho(x')dx', \tag{B.1}$$

$$I(x) = \int_{-\infty}^{x} f(x')dx', \tag{B.2}$$

where the parent distribution $\rho(x)$ is normalized to unity:

$$\int_{-\infty}^{\infty} \rho(x')dx' = 1. \tag{B.3}$$

If $f(x)$ and $I(x)$ are obtained from the testbeam results, one can calculate $P(X)$, the fractional energy deposited in a channel at distance X from the shower center, and $dP(X)/dX$, the derivative of the fractional pulse height with respect to changes in

shower position:

$$P(X) = I(X) - I(X - \delta X) \tag{B.4}$$

$$dP(X)/dX = f(X) - f(X - \delta X) \tag{B.5}$$

$P(X)$ and $dP(X)/dX$ are used for fitting the CES cluster of real data.

B.2 Strip/Wire Profile Differences

The parent wire profile, $\rho(x)$, is independent of the X position of the shower center (X_0) and is symmetric about X_0, while the parent strip profile depends on the Z position of the shower center(Z_0) and not symmetric about Z_0. This asymmetry is caused by two reasons; one is simply the geometry of the CES and incident electrons, which is corrected by the following transformation:

$$Z' = Z \sin\theta, \tag{B.6}$$

where θ is the polar angle of the incident electron with respect to the detector z axis.

Another reason is the total amount of materials in front of the CES varies depending on the angle of the incident electrons, which is corrected by multiplying $cos\,\theta$ to the asymmetric parent function, $f_{s,anti}(z')$.

The strip profile is decomposed into a symmetric profile $f_{s,sym}$ and an antisymmetric profile $f_{s,anti}$, which are defined by:

$$f_{s,sym}(z) = \frac{1}{2}\left\{f_s(z) + f_s(-z)\right\}, \tag{B.7}$$

$$f_{s,anti}(z) = \frac{1}{2}\left\{f_s(z) - f_s(-z)\right\}. \tag{B.8}$$

So the complete strip profile is written by:

$$f_s(z') = f_{s,sym}(z') + f_{s,anti}(z')cos\,\theta, \tag{B.9}$$

Parameter	g	b_1	b_2	q_1	q_2
X(Wire) Value	0.311	0.472	2.065	-0.031	-0.044
Z(Strip) Value	0.269	0.583	2.182	-0.031	-0.044

Table B.1: parameters

Figure B.1 shows the standard electron profiles and the standard electron integral profile, both of which are from the electron testbeam results. Both plots are normalized to unity.

B.3 Parametrization of the CES Standard Profile

B.3.1 Parametrization of the Symmetric Profile

The transverse profile in a radial coordinate is parametrized as a double exponential form:

$$I(r) = \frac{0.5}{1+g}\left[\exp\left(-\frac{|r|}{b_1}\right) + g\exp\left(-\frac{|r|}{b_2}\right)\right] \tag{B.10}$$

Note that $I(r)$ is symmetric about $r = 0$ and $I(0) = 0.5$. I is then transformed from a radial coordinate to the x and z positions measured by the strip chambers:

$$I(X) = \frac{0.5}{1+g_x}\left[\exp\left(-\frac{|X|}{b_{1x}}\left(1+\frac{q_{1x}|X|}{b_{1x}}\right)\right) + g_x\exp\left(-\frac{|X|}{b_{2x}}\left(1+\frac{q_{2x}|X|}{b_{2x}}\right)\right)\right], \tag{B.11}$$

$$I(Z) = \frac{0.5}{1+g_z}\left[\exp\left(-\frac{|Z|}{b_{1z}}\left(1+\frac{q_{1z}|Z|}{b_{1z}}\right)\right) + g_z\exp\left(-\frac{|Z|}{b_{2z}}\left(1+\frac{q_{2z}|Z|}{b_{2z}}\right)\right)\right], \tag{B.12}$$

where X and Z are given in cm.

Table B.1 shows the parameters of the symmetric profile.

B.3.2 Parametrization of the Antisymmetric Profile

The integral from $-\infty$ to Z of the antisymmetric distribution can be parametrized as:

$$\delta I(Z) \;=\; (a + b|Z|)\,\exp\left(-\frac{|Z|}{b_3}\right)\,, \tag{B.13}$$

where Z is the shower coordinate relative to shower center. a, b and b_3 are therefore $a = -0.026, b = -0.022$ and $b_3 = 1.60$. Using these values, Eq. B.13 multiplied by a factor

$$f \;=\; 1 \;+\; 0.35\exp\left(-|Z|/5.\right) \tag{B.14}$$

fits the 1985 testbeam data within 5 cm of the shower center.

B.3.3 Energy Scaling of the Variance

The variance σ_i^2, the squared RMS fluctuation of the CES channel i measured profile depends on the number of secondary particles passing through the CES. Basically the number of secondaries is proportional to the primary electron's energy $(N \sim E)$, and assuming Poisson fluctuations in the fractional number of secondaries in each channel $(\sigma_i^2 = 1/N_i)$ gives a variance:

$$\sigma_i^2 \;\sim\; 1/E. \tag{B.15}$$

From 1985 testbeam, we estimated the energy dependence of the variance of the CES.

$$\sigma_i^2 \;=\; \sigma_{10,i}^2\,\left(\frac{10}{E}\right)^{0.747} \tag{B.16}$$

where

$$\sigma_{10,i}^2 \;=\; (0.026)^2 \;+\; y(x_i)\,(0.096)^2 \tag{B.17}$$

is the variance of channel i in the normalized profile determined from 1985 10 GeV testbeam electrons. Equation B.16 and the power 0.747 in that equation were determined from the measured CES response vs. energy in 1985 testbeam data.

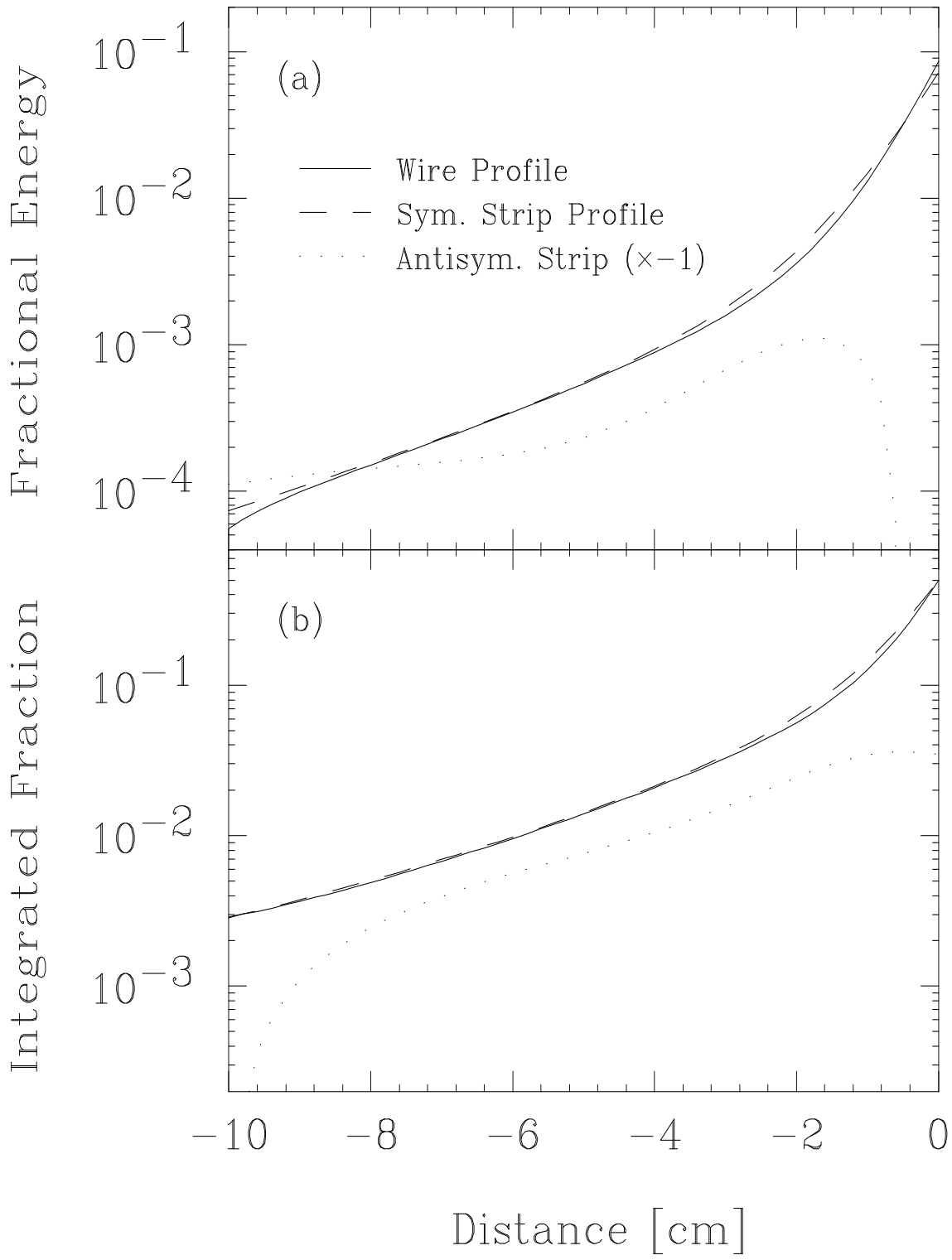

Figure B.1: (a) The standard electron profiles and (b) the standard electron integral profile. These are obtained from the electron testbeam. In both (a) and (b), the solid line is the wire profile, the dashed line is the symmetric strip profile and dotted line is the antisymmetric profile.

Bibliography

[1] H. Fritzsch, M. Gell-Mann and H. Leutwyler, Phys. Lett. B 47 (1973) 365.

[2] D. J. Gross, and F. Wilczek, Phys. Rev. Lett. 30 (1973) 1343,

[3] H. D. Politzer, Phys. Rev. Lett. 30 (1973) 1346,

[4] F. Abe *et al.*, Phys. Rev. D 49 (1994) 1.

[5] F. Abe *et al.*, Phys. Rev. Lett. 77 (1996) 448.

[6] F. Abe *et al.*, Phys. Rev. Lett. 77 (1996) 438.

[7] J. F. Owens, Rev. Mod. Phys. 59 (1987) 465.

[8] D. W. Duke and J. F. Owens, Phys. Rev. D 30 (1984) 49.

[9] G. Altarelli and G. Parisi, Nucl. Phys. B 126 (1977) 298.

[10] J. Botts *et al.* (CTEQ collaboration), Phys. Lett. B 304 (1993) 145.

[11] B. Bailey *et al.*, Phys. Rev. D 46 (1992) 2018.

[12] J. F. Gunion, G. L. Kane and J. Wudka, Nucl. Phys. B 299 (1988) 231.

[13] F. Abe *et al.* (CDF collaboration), Phys. Rev. Lett. 73 (1994) 2662.

[14] J. Huston *et al.*, "A Global QCD Study of Direct Photon Production", MSU=HEP-41027, Michigan State University, January 1995.

[15] J. Huston, private communication.

[16] T. Ferbel, W. R. Molzon, Rev. Mod. Phys., 56, (1984) 181.

[17] J. Alitti *et al.* (UA2 collaboration), Phys. Lett. B 288 (1992) 386.

[18] C. Albajar *et al.* (UA1 collaboration), Phys. Lett. B 209 (1988) 385.

[19] F. Abe *et al.* (CDF collaboration), Phys. Rev. Lett. 70 (1993) 2232.

[20] D. Toback, "The Diphoton Missing E_T Distribution at CDF", Proceedings of the 1996 DPF Meeting.

[21] F. Abe *et al.* (CDF collaboration), Nucl. Instr. and Meth. A271 (1988) 387.

[22] H. Minemura *et al.*, Nucl. Instr. and Meth. A238 (1985) 18.

[23] F. Snider *et al.*, Nucl. Instr. and Meth. A268 (1988) 75.

[24] F. Bedeschi *et al.*, Nucl. Instr. and Meth. A268 (1988) 50.

[25] L. Balka *et al.*, Nucl. Instr. and Meth. A267 (1988) 272.

[26] R. Blair *et al.*, "Proposal for a Preradiator Chamber for the CDF Central Detector", CDF internal note 760.

[27] K. Yasuoka *et al.*, Nucl. Instr. and Meth. A267 (1988) 315.

[28] R. G. Wagner *et al.*, Nucl. Instr. and Meth. A267 (1988) 330.

[29] S. Bertolucci *et al.*, Nucl. Instr. and Meth. A267 (1988) 301.

[30] G. W. Foster *et al.*, Nucl. Instr. and Meth. A269 (1988) 93.

[31] G. Ascoli *et al.*, Nucl. Instr. and Meth. A269 (1988) 63.

[32] B. Denby *et al.*, Nucl. Instr. and Meth. A356 (1995) 485.

[33] CERN-Pisa-Rome-Stony Brook Collaboration, Phys. Lett. B62 (1976) 460; M. Bozzo *et al.* (UA4 Collaboration), Phys. Lett. B147, (1984) 392.

[34] F. Abe *et al.* (CDF collaboration) , Phys. Rev. D50 (1994) 5518; phys. Rev. D50 (1994) 5550.

[35] C. Grosso-Pilcher *et al.* "Luminosity for the Top PRL", CDF internal note 3021.

[36] L. Nodulman, K. Byrum, "CEM Tower Calibration and Map Trim", CDF internal note 2487.

[37] L. Nodulman, "Preliminary CEM Calibration for 1B to the Feb. Shutdown", CDF internal note 3048.

[38] A. Maghakian *et al.*, "Inclusive Photon Cross Section 1992", CDF internal note 1963.

[39] R. M. Harris, "Definition of CES χ^2", CDF internal note 1329.

[40] W. Badgett, P. derwent, CDF internal note 2703.

[41] "Review of Particle Physics" , Phys. Rev. D 54 (1996).

[42] "PYTHIA 5.7 and JETSET 7.4", CERN-TH.7112/93. (1993).

[43] M. Shaprio *et al.*, "A User's Guide to QFL", CDF internal note 1810.

[44] R. M. Harris, "Measurement of η/pi^0 from Isolated Decays into Two Photons", CDF internal note 1472.

[45] R. M. Harris, R. Blair and S. Kuhlmann, "Calibration of CPR Conversion Probability from Fully Reconstructed η and π^0 Mesons", CDF internal note 2318.

[46] S. Kuhlmann and A. Maghakian, "Calibration of CPR Conversion Probability from $\rho^{\pm} \to \pi^{\pm}\pi^0$ Decay", CDF internal note 2478.

[47] F. Abe *et al.* (CDF collaboration), Phys. Rev. D 40 (1989) 3791.